AFRL-PR-WP-TR-2001-2110

HIGH-TEMPERATURE TRIBOLOGY OF SILICON NITRIDE LUBRICATED WITH CESIUM-BASED INORGANIC FILMS

LEWIS ROSADO, Ph.D.

MECHANICAL SYSTEMS BRANCH
TURBINE ENGINE DIVISION
PROPULSION DIRECTORATE
AFRL/PRTM
BUILDING 490, RM 217
WRIGHT-PATTERSON AFB, OH 45433-7251

DECEMBER 2001

FINAL REPORT FOR PERIOD OF 30 JANUARY 1997 – 30 SEPTEMBER 2001

Approved for public release; distribution unlimited

20020422 233

PROPULSION DIRECTORATE
AIR FORCE RESEARCH LABORATORY
AIR FORCE MATERIEL COMMAND
WRIGHT-PATTERSON AIR FORCE BASE, OH 45433-7251

NOTICE

USING GOVERNMENT DRAWINGS, SPECIFICATIONS, OR OTHER DATA INCLUDED IN THIS DOCUMENT FOR ANY PURPOSE OTHER THAN GOVERNMENT PROCUREMENT DOES NOT IN ANY WAY OBLIGATE THE US GOVERNMENT. THE FACT THAT THE GOVERNMENT FORMULATED OR SUPPLIED THE DRAWINGS, SPECIFICATIONS, OR OTHER DATA DOES NOT LICENSE THE HOLDER OR ANY OTHER PERSON OR CORPORATION; OR CONVEY ANY RIGHTS OR PERMISSION TO MANUFACTURE, USE, OR SELL ANY PATENTED INVENTION THAT MAY RELATE TO THEM.

THIS REPORT IS RELEASABLE TO THE NATIONAL TECHNICAL INFORMATION SERVICE (NTIS). AT NTIS, IT WILL BE AVAILABLE TO THE GENERAL PUBLIC, INCLUDING FOREIGN NATIONS.
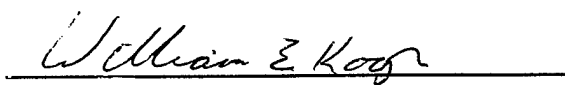
THIS TECHNICAL REPORT HAS BEEN REVIEWED AND IS APPROVED FOR PUBLICATION.

LEWIS ROSADO, Ph.D.
Project Engineer
Mechanical Systems Branch

ROBERT L. WRIGHT, Ph.D.
Chief, Mechanical Systems Branch

WILLIAM E. KOOP
Chief of Technology
Turbine Engine Division
Propulsion Directorate

Do not return copies of this report unless contractual obligations or notice on a specific document requires its return.

REPORT DOCUMENTATION PAGE

The public reporting burden for this collection of information is estimated to average 1 hour per response, including the time for reviewing instructions, searching existing data sources, searching existing data sources, gathering and maintaining the data needed, and completing and reviewing the collection of information. Send comments regarding this burden estimate or any other aspect of this collection of information, including suggestions for reducing this burden, to Department of Defense, Washington Headquarters Services, Directorate for Information Operations and Reports (0704-0188), 1215 Jefferson Davis Highway, Suite 1204, Arlington, VA 22202-4302. Respondents should be aware that notwithstanding any other provision of law, no person shall be subject to any penalty for failing to comply with a collection of information if it does not display a currently valid OMB control number. **PLEASE DO NOT RETURN YOUR FORM TO THE ABOVE ADDRESS.**

1. REPORT DATE *(DD-MM-YY)*	2. REPORT TYPE	3. DATES COVERED *(From - To)*
December 2001	Final	01/30/1997 – 09/30/2001

4. TITLE AND SUBTITLE

HIGH-TEMPERATURE TRIBOLOGY OF SILICON NITRIDE LUBRICATED WITH CESIUM-BASED INORGANIC FILMS

5a. CONTRACT NUMBER
N/A

5b. GRANT NUMBER

5c. PROGRAM ELEMENT NUMBER
62203F

6. AUTHOR(S)

LEWIS ROSADO, Ph.D.

5d. PROJECT NUMBER
3048

5e. TASK NUMBER
06

5f. WORK UNIT NUMBER
19

7. PERFORMING ORGANIZATION NAME(S) AND ADDRESS(ES)

MECHANICAL SYSTEMS BRANCH
TURBINE ENGINE DIVISION
PROPULSION DIRECTORATE
AFRL/PRTM
BUILDING 490, RM 217
WRIGHT-PATTERSON AFB, OH 45433-7251

8. PERFORMING ORGANIZATION REPORT NUMBER

9. SPONSORING/MONITORING AGENCY NAME(S) AND ADDRESS(ES)

PROPULSION DIRECTORATE
AIR FORCE RESEARCH LABORATORY
AIR FORCE MATERIEL COMMAND
WRIGHT-PATTERSON AIR FORCE BASE, OH 45433-7251

10. SPONSORING/MONITORING AGENCY ACRONYM(S)
AFRL/PRTM

11. SPONSORING/MONITORING AGENCY REPORT NUMBER(S)
AFRL-PR-WP-TR-2001-2110

12 DISTRIBUTION/AVAILABILITY STATEMENT
Approved for public release; distribution unlimited.

13. SUPPLEMENTARY NOTES

14 ABSTRACT *(Maximum 200 Words)*
The sliding friction and wear of silicon nitride was investigated in 600 °C air using a ball-on-disk configuration. Two cesium-based inorganic films were studied as potential high-temperature solid lubricants for limited-life turbine engine bearing applications: a sodium silicate bonded Cs_2WOS_3 coating and a cesium silicate chemical reaction film. Wear surfaces were characterized using various analytical techniques. The best tribological performance was obtained with thin chemical reaction films annealed in sulfur-rich air. Friction coefficients (f) and wear factors as low as 0.04 and 4×10^{-9} mm3/N·m respectively, were obtained at 600 °C with this system. These are comparable to boundary liquid lubricating films at much lower temperatures. The data provide conclusive evidence that neither tungsten nor molybdenum is necessary for low friction at 600 °C. The results also suggest that sulfur and cesium play important roles in the formation of a lubricious silicate film by chemically reacting with the silicon dioxide scale that naturally forms on silicon nitride surfaces. This occurs via a complex hot-corrosion mechanism involving the inward diffusion of oxygen from the surrounding air and cesium from the coatings and the outward diffusion of nitrogen and magnesium from the silicon nitride substrate. It is believed that sulfur provides a reaction path for the hot-corrosion mechanism.

15. SUBJECT TERMS

High-temperature lubrication, tribology, silicon nitride, surface chemistry

16. SECURITY CLASSIFICATION OF:			17. LIMITATION OF ABSTRACT:	18. NUMBER OF PAGES	19a. NAME OF RESPONSIBLE PERSON (Monitor)
a. REPORT Unclassified	**b. ABSTRACT** Unclassified	**c. THIS PAGE** Unclassified	SAR	178	LEWIS ROSADO, Ph.D. **19b. TELEPHONE NUMBER** *(Include Area Code)* (937) 255-6519

TABLE OF CONTENTS

TABLE OF CONTENTS (concluded)

LIST OF FIGURES

LIST OF FIGURES (continued)

LIST OF FIGURES (concluded)

LIST OF TABLES

PREFACE

1. INTRODUCTION

The endless pursuit for increased aircraft speed and range has led gas turbine engine designers to continuously explore new ways to improve engine performance while reducing size, weight, and cost. During the past decade a genuine attempt to double the thrust-to-weight ratio of future aircraft gas turbine engines was undertaken by the Department of Defense and the U.S. turbine engine industry under the Integrated High-Performance Turbine Engine Technology (IHPTET) program. The substantial increase in performance, which is derived primarily from boosts in the engine thermodynamic cycle, imposes unprecedented operating requirements on all turbine engine components, including the mainshaft support bearings and the lubricant used for lubrication and coolant.

Because of its simplicity and considerable performance, weight, and cost benefits, the ideal approach would be to completely eliminate the complex recirculating liquid lubrication system and provide rotor support with noncontacting type bearings (i.e., foil, hydrostatic air, magnetic bearings, etc.) or with a self-contained/self-lubricating rolling element bearing system. Because of their limited load capacity and poor damping properties, the noncontacting types appear more promising for lightly loaded applications, such as for small subsonic, long-range aircraft (i.e., subsonic expendable engines, uninhabited air vehicles, etc.). For highly loaded applications, such as large fighter class or small supersonic engines, the high-load capacity, stiffness, and robustness of rolling element-type bearings make these the preferred choice, at least for the foreseeable future. Yet, the ability to lubricate these at very high temperature remains a formidable challenge, particularly for systems requiring high-speed operation and long-life (100+ hours).

In limited-life systems, such as small supersonic expendable engines for cruise missiles, bearing life is of the order of several hours and a self-lubricating rolling element bearing concept becomes more viable. Nonetheless, the high Mach speed envisioned in some of these applications results in a high stagnation temperature at the compressor inlet, and consequently, the compressor discharge air, typically used to cool internal engine components, becomes extremely hot. Bearing sump air temperatures as high as 650°C are predicted for such an engine. The high rotational bearing speeds and loads, together with the absence of an adequate heat sink (i.e., cooling air, recirculating lubricant, etc.) further aggravate the situation. This temperature is well beyond the limit of current turbine engine liquid lubricants and bearing tool steels. It is also above the oxidative limit of most common solid lubricants, such as molybdenum disulfide (MoS_2) and graphite. Therefore, for such a system to work, significant advances in high-temperature lubrication and bearing materials will be needed.

1.1 Background

1.1.1 Historical Perspective

While the need for high-speed, high-temperature bearing technology has been made apparent recently under IHPTET, it has been the subject of numerous studies that date back half a century [1-16]. Most of the early work involved supplying solid lubricant powders (i.e., MoS_2/graphite) to bearing surfaces or relying on solid lubricant film transfer from composite sacrificial bearing cages to rolling element and bearing race surfaces. In most cases, bearing failure was attributed to cage unbalance at high speed caused by wear of the cage or to inadequate solid lubricant performance and endurance. Problems associated with bearing seizure, caused by thermal gradients across the bearing, were also common. An excellent review of early work is given by Bisson and Anderson [17].

The difficulty of operating bearings for extended periods of time at high temperature and high speed, simultaneously, is apparent from these studies. For example, Sliney and Johnson [13] demonstrated bearing lives of the order of hundreds of hours at 650°C on a cobalt alloy (Stellite) 204-size ball bearing using calcium fluoride/barium fluoride eutectic (CaF_2/BaF_2) as the solid lubricant, but maximum bearing speed in this case was only 0.10 MDN (MDN = shaft diameter (mm) times $rpm/10^6$). Similarly, 14.0 hours were accumulated on an M2 steel 204-size ball bearing operating at 0.8 MDN using a silver-mercury-Teflon-molybdenum diselenide (AgHg-WTFE-$MoSe_2$) composite self-lubricating cage, but temperatures never exceeded 200°C [14]. Achieving bearing operation above 500°C and 1.0 MDN simultaneously in an oxidizing environment was a barrier that was not overcome until the use of the complex metal chalcogenide solid lubricants and bearing grade silicon nitride (Si_3N_4) materials in the late 1980s [18]. The use of a superalloy, wear-resistant cage material, rather than relying on a sacrificial, self-lubricating one, was also critical in achieving high speed operation.

More recently, Forster [19] successfully demonstrated steady-state bearing operation at temperatures up to 475°C and speeds of 1.0 MDN on hybrid T-15 tool steel/Si_3N_4 206-size ball bearings. In this case, the bearings were fitted with a light-weight carbon-carbon (C-C) composite cage and were lubricated with vapor phase deposition (VPD) films formed in situ from an externally supplied phosphate ester mist. Bearing lives of up to 20 hours were demonstrated using this approach. He concluded that the VPD film appears to form only on ferrous type substrate materials through a complex mechanism involving the formation of graphitic carbon within a crosslinked polyphosphate structure and cation diffusion of carbon and iron. Though this lubrication method is evidently the most effective thus far developed for steel bearings operating in the 350 to 500°C range, it is unclear, and probably unlikely, that it can perform as well at temperatures above 600°C, particularly with ceramic substrate materials such as Si_3N_4. Since the need for higher temperature dictates the use of ceramic materials, a suitable solid lubrication approach for these materials is still desired.

1.1.2 Solid Lubrication with Complex Metal Chalcogenides

The synthesis of the complex metal chalcogenides was first reported by Müller et al. in 1968 [20-22]. The general chemical formula for these compounds can be represented as $M_x M'_y S_z$, where M and M' are different metals or the same metals in different oxidation states. S represents one or more of the chalcogenides (sulfur, selenium, and tellurium). Improvements in oxidation and thermal stability can be obtained by replacing some of the chalcogen atoms in the MM'S structure with oxygen. This results in a structure of the form $M_a M'_b O_c S_d$. King et al. [23-25] first applied these compounds to the field of tribology in the early 1980s as anti-wear and extreme pressure additives in lithium grease. They found that antimony thioantimonate and cerium and zinc thio- and oxythiomolybdates (i.e., M = Sb, Ce, Zn; M' = Sb, Mo; S = S) provided superior wear resistance to 52100 steel and 440C stainless steel when compared to a MoS_2 additive. They also found that the oxythiomolybdates, including cesium oxythiomolybdate (Cs_2MoOS_3), showed excellent thermal stability and speculated that these would perform well as high-temperature solid lubricants.

The initial investigation of these compounds as high-temperature solid lubricants was performed by Devine et al. [18, 26] as sodium silicate bonded coatings on subscale and full-scale Si_3N_4 bearings, confirming their excellent thermal stability and tribological properties. Devine showed that silicate bonded Cs_2MoOS_3 films could adequately lubricate all-ceramic Si_3N_4 bearings in air at temperatures up to 760°C, speeds up to 1.2 MDN, and thrust loads of 890 N for periods of 3 to 6 hours. However, they experienced high bearing failure rates and poor experimental reproducibility. Galbato [27] also demonstrated bearing lives of the same order at 620°C and 1.1 MDN using similar Si_3N_4 bearings lubricated with externally supplied Cs_2MoOS_3 powder, but also had a high failure-to-success rate. He attributed the inconsistent bearing life to difficulties in supplying the powdered lubricant and the inherent poor fracture toughness of the Si_3N_4 bearing raceway components. Nonetheless, he also obtained traction coefficients, viz. friction coefficient under combined rolling and sliding, on subscale ball-on-disk samples in the range of 0.009 to 0.12 at temperatures between 538 and 677°C on various silicon-based ceramic pairs. These remarkably low traction values are within the range obtained with conventional liquid lubricants at room temperature. The best traction and wear response was obtained on Si_3N_4/Si_3N_4 mating pairs.

In 1990 King and Forster [28] reported the development of three additional lubricants, referred to as the second-generation complex chalcogenides. In particular, two of the compounds, cesium oxythiotungstate (Cs_2WOS_3) and zinc oxythiomolybdate ($ZnMoOS_3$), showed very good thermal stability and good antiwear properties on Si_3N_4 sliding against itself at 650°C. Thermogravimetric analysis (TGA) also showed that Cs_2WOS_3 was more thermally stable in air than Cs_2MoOS_3. They obtained sliding friction coefficients between 0.16 and 0.23 at 650°C with these compounds as sodium silicate bonded films. The authors, however, noted a large variation in friction coefficient.

More recently, we have found that a wide range of coatings containing cesium, including sodium silicate bonded Cs_2MoOS_3, Cs_2WOS_3, Cs_2SO_4, CsOH, a cesium silicate chemical reaction film, and mixtures of these containing tungsten disulfide (WS_2) provide

excellent endurance to Si_3N_4 rolling contacts at a temperature of 650°C and at very high contact stresses (4.34 GPa) [29]. We also found that these do not perform well on metallic substrate materials suggesting a chemical interaction between the cesium-based coatings and the Si_3N_4 substrate. The results of this study are summarized in Figure 1. As shown, mean life obtained at 650°C on most of the cesium-based coatings on Si_3N_4 was about two orders of magnitude higher than that obtained on other known solid lubricant bonded coatings on steel and Si_3N_4 substrates. Large scatter in the data was observed though, even under seemingly well controlled laboratory conditions. It was hypothesized that a lubricious cesium silicate glass of the form $Cs_2O{\cdot}xSiO_2$ with low shear strength properties, and perhaps in the liquid state, was formed between the decomposition products of the cesium-based coatings and the silicon dioxide (SiO_2) scale that is naturally formed on Si_3N_4. We also discovered that Cs_2WOS_3 accelerates the formation of SiO_2 on Si_3N_4 at relatively low temperatures (700°C), lending support to this hypothesis. A mechanism based on the hot corrosion of Si_3N_4 with alkali metal salts was proposed to explain this phenomenon [30].

These results were recently confirmed by Strong [31] who obtained excellent sliding friction and wear performance on pulsed laser deposited Cs_2MoOS_3 thin films on silicon-based ceramic substrates. She obtained the best performance on Si_3N_4 mating pairs between 600 and 700°C with friction coefficients as low as 0.03 and attributed the low friction to the formation of a glassy cesium silicate film.

The excellent subscale rolling contact performance obtained with some of these new lubricious compounds was substantiated further by the author in 1997 on full-scale, all-ceramic Si_3N_4 bearings. Figure 2 shows performance data obtained on 206-size angular contact ball bearings lubricated with a Cs_2WOS_3 sodium silicate bonded coating and a cesium silicate reaction film supplemented with a Cs_2WOS_3 + WS_2 powder mixture. The bearings were also fitted with a C-C composite cage. As shown, bearing lives of the order of 1 to 3 hours were obtained at about 650°C, 1.2 MDN, and 445 N of thrust load in an oxidizing environment. But similar to the work previously done by Devine and Galbato with Cs_2MoOS_3, bearing life was inconsistent.

These studies clearly show that short-term bearing operation above 600°C and 1.0 MDN without an external lubricant supply is possible with these materials. However, the erratic bearing life behavior and poor experimental reproducibility has limited the development and practical use of this technology. It is believed that significant progress can be made if a basic understanding of underlying tribological mechanisms is developed for these materials.

The objective of the research described in this report was to further investigate the high-temperature tribological characteristics of cesium-containing films on silicon nitride in an oxidizing environment. Two coating systems were investigated, a sodium silicate ($Na_2O{\cdot}3SiO_2$) bonded Cs_2WOS_3 coating and a cesium silicate chemical reaction film. The selection of Cs_2WOS_3 was based on previous results that showed good antiwear properties and rolling contact endurance on Si_3N_4 and superior thermal stability in air when compared to other complex chalcogenides. Because of its chemical similarity to

4

Conventional solid lubricants = MoS_2, $EMoS_2$, WS_2, and EX1623B

High temp. solid lubricants = $ZnMoOS_3$, EX1623A, TiO_2, CaF_2/BaF_2, CuO/Re_2O_7, and CeF_3

Mean Life (hours)

High temp. lubricants on Si_3N_4

Cs-based coatings on BG42 and T15 steels

Cs-based coatings on Si_3N_4

Conventional solid lubricants on BG42, M62, M50 and T15 steels

From Rosado et al., *Trib. Trans.*, **43**(3), pp. 489-497, 2000.
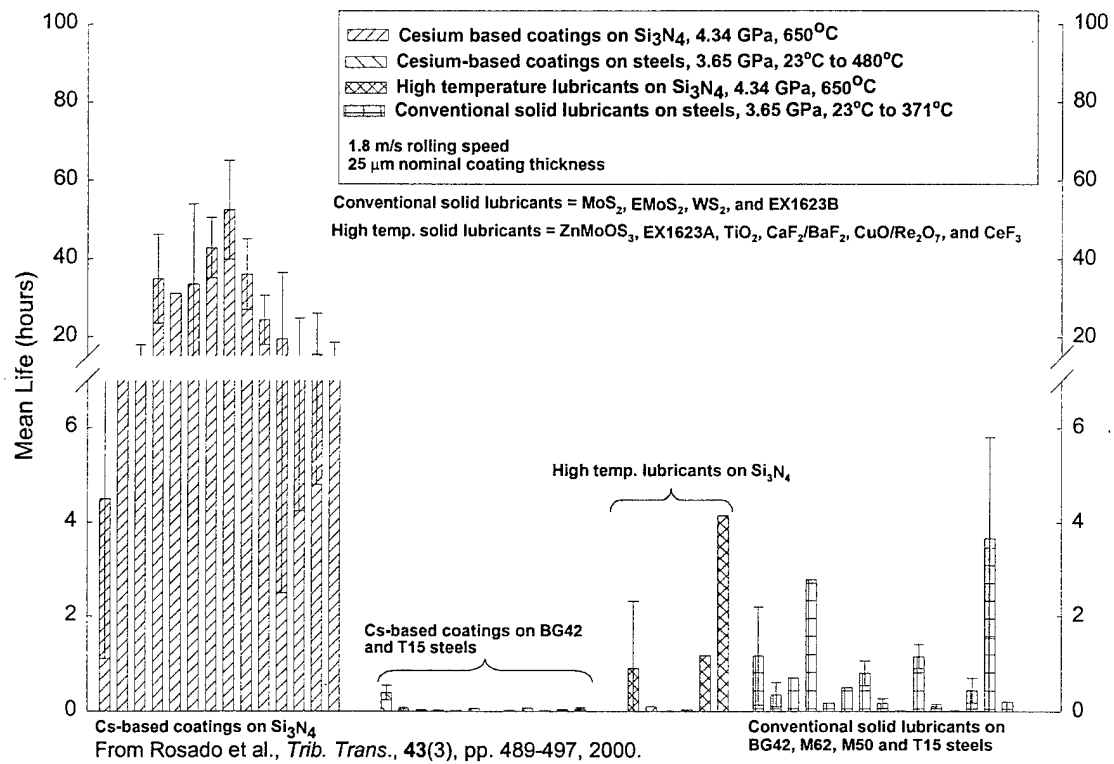
Figure 1. Comparison of Rolling Contact Endurance Between Cesium-Based Coatings on
Si_3N_4 and Conventional Solid Lubricants
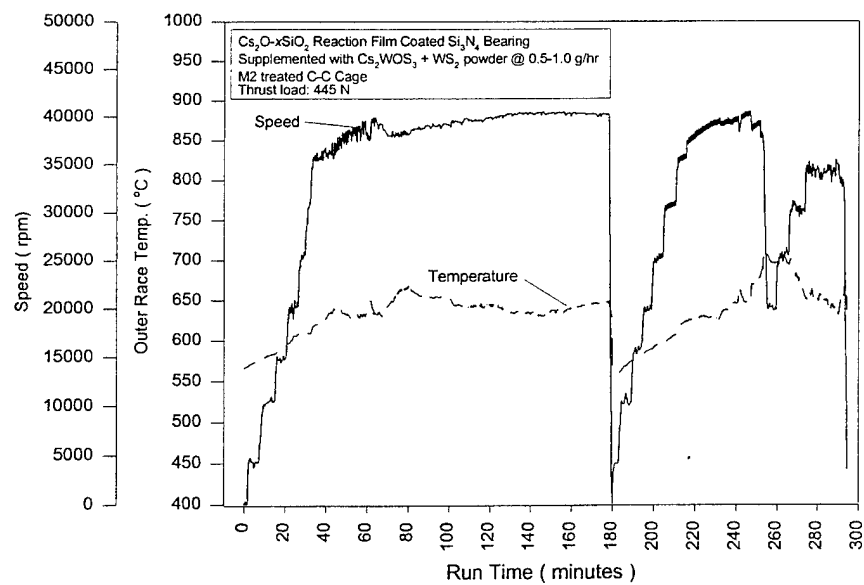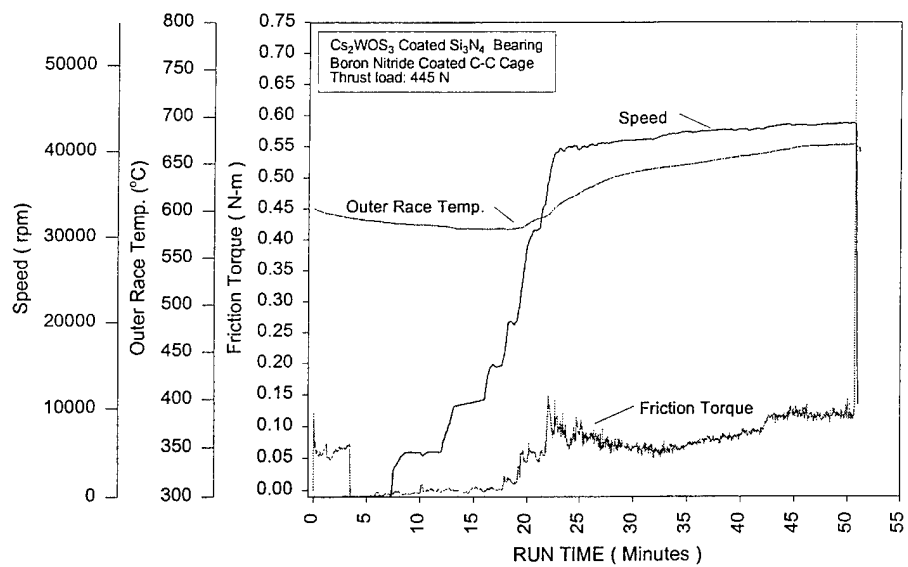
Figure 2. Performance Data Obtained on Full-Scale, All-Ceramic Si₃N₄ Angular Contact
Ball Bearings

Cs$_2$MoOS$_3$, results could also be generalized to sodium silicate bonded systems containing the molybdate. The selection of the cesium silicate film was primarily based on the presumption that this is the actual lubricating constituent that results from chemical reactions between cesium-based coating decomposition products and the oxide scale on Si$_3$N$_4$. The absence of tungsten, molybdenum, sulfur, and sodium in this system also allowed the author to study a simple system that could perhaps shed light on the role that these various elements play in the tribo-process.

Sliding friction and wear experiments were performed in air, mostly at 600°C, on uncoated and coated Si$_3$N$_4$ using a stationary ball on rotating disk configuration. Sliding wear factors were determined from experimental wear measurements. To elucidate tribo-mechanisms, surfaces were examined with optical and scanning electron microscopy (SEM) and the surface chemistry of postested samples was analyzed using various surface analytical techniques. This was supplemented with structural and surface chemical analysis of pyrolyzed Cs$_2$WOS$_3$ powders and static thermal analysis of powdered mixtures of Cs$_2$WOS$_3$ (with and without the sodium silicate binder) and Si$_3$N$_4$. The thermal analysis and thermochemistry results are included in the appendix.

2. EXPERIMENTAL

This section describes the starting Si_3N_4 and Cs_2WOS_3 materials, coating procedures, and experimental equipment used for friction and wear experimentation. The analytical techniques used to characterize surfaces of post tested samples are also described. The starting materials are described first.

2.1 Starting Materials

2.1.1 Silicon Nitride Substrate Material

Disk specimens, 2.54 cm in diameter by 0.635 cm thick, were fabricated from hot-isostatically pressed (HIP'ed) NBD-200 Si_3N_4 material made by Norton Advanced Ceramics (now St. Gobain), East Granby, Connecticut. The chemical composition and mechanical properties, as reported in [32], are given in Tables 1 and 2, respectively. NBD-200 Si_3N_4 contains about 1.0 wt% magnesium oxide (MgO) as the sintering aid, which is primarily concentrated at the grain boundaries as an amorphous glassy magnesium silicate phase. An etched cross section showing the microstructure of the material is depicted in Figure 3. The microstructure consists of elongated grains of up to about 5 μm in length and 0.5 μm in diameter. The observed microstructure is typical of that reported for other HIP'ed Si_3N_4 materials [32-34].

The disk specimens were lapped on one side to a mirror surface finish with a nominal roughness of 0.025 μm R_a by the manufacturer. The mean surface roughness value obtained on five as-received samples using a Sloan DEKTAK surface profilometer was 0.0279 μm R_a. Raman surface analysis confirmed the material to be predominantely β-Si_3N_4 with some free crystalline silicon, while AES analysis shows that the surface is covered with a thin layer containing silicon, nitrogen, oxygen and carbon. Fourier transform infrared (FTIR) spectroscopy, which in the arrangement used here is more surface sensitive than Raman, indicates the layer is mostly amorphous and appears to consist of amorphous silicon carbide (a-SiC), silicon oxynitride, and vitreous SiO_x. It is believed that the a-SiC was introduced during sample grinding and finishing. The surface analysis results are presented in Section 4. Grade 5 NBD-200 Si_3N_4 balls (0.635 mm in diameter), also purchased from Norton Advanced Ceramics, were used for all friction and wear experiments. The initial surface chemistry of balls was not characterized.

Prior to experimentation, the Si_3N_4 disks and balls were cleaned by scrubbing lightly in a solution consisting of distilled water (DH₂O) and 2 percent detergent cleaner, rinsing with DH₂O and pat drying with Kimwipe tissue. The samples were then rinsed in toluene and acetone, given a final wash in detergent solution, and then thoroughly rinsed with DH₂O. Samples were then dried in a flowing stream of dry nitrogen. Clean disks were wrapped in Kimwipe tissue and stored in clean tin containers. Balls were stored in clean glass vials.

Table 1. Nominal Chemical Composition of NBD-200 Si_3N_4						
% Weight						
Si_3N_4	Al	C	Ca	Fe	Mg	O
97.1-94.1	≤ 0.5	≤ 0.88	≤ 0.04	≤ 0.17	0.6 – 1.0	2.3 – 3.3

Table 2. Mechanical Properties of NBD-200 Si_3N_4	
Density	3.16 g/cm^3
Flexural strength	800 MPa
Tensile strength	400 MPa
Compressive strength	3.0 GPa
Hertz compressive strength	28 GPa
Fracture toughness	4.1 MPa m$^{1/2}$
Elastic modulus	320 GPa
Poisson's ratio	0.26
Indentation hardness (Vickers)	16.6 GPa
Rockwell C hardness	> 70
Thermal expansion coefficient	2.9 x 10^{-6}/°C

Figure 3. Etched Microstructure of NBD-200 Si_3N_4 Disk (5000X)

2.1.2 Cesium Oxythiotungstate Starting Powder

Background on the molecular and crystal structure, detailed synthesis, and characterization of the starting Cs_2WOS_3 powder used for the bonded coatings is given in the Appendix A. For the present study, Cs_2WOS_3 was synthesized by Desilube Technology, Inc., Lansdale, Pennsylvania, using a procedure slightly different from that originally described by Müller et al. [20-22]. The reaction is $Na_2WO_4 \cdot 2H_2O + 2CH_3CO_2Cs + 3H_2S \longrightarrow Cs_2WOS_3 + 5H_2O + 2CH_3CO_2Na$.

The resulting bright yellow material was ball milled for 24 hours into a fine powder, which was then used for the sodium silicate bonded coatings. The SEM photomicrographs shown in Figure 4 depict the Cs_2WOS_3 powder morphology prior to and after ball milling. Particles in the as-prepared material were mostly shaped as thin rectangular platelets less than 100 μm, though some prism-shaped crystals were also present as shown in Figure 4a. Ball milling significantly reduced the particle size as shown in Figure 4b. X-ray powder diffraction (XRPD), FTIR and Raman spectroscopy, described in detail in the Appendix A, all show a well-defined crystal structure consistent with that reported in the literature for this compound. However, XRPD did detect the presence of an unknown second phase and FTIR and ion chromatography detected trace amounts of cesium sulfate (Cs_2SO_4) while Raman detected elemental sulfur. Surface analysis by x-ray photoelectron spectroscopy (XPS) also found higher oxygen and lower sulfur and cesium surface levels suggesting that the surface of the Cs_2WOS_3 particles had partly oxidized, probably to Cs_2SO_4.

2.2 Bonded Coating Procedure

Bonded coatings were applied by Dr. James P. King of Desilube Technology, Inc. Coatings were only applied to disks (balls were uncoated). The thickness of clean Si_3N_4 disks were initially measured using a digital caliper prior to surface treatment. A typical procedure involved the following; 2.4 g of ball-milled Cs_2WOS_3 powder and 2.2 g DH_2O were mixed with a mortar and pestle. Sodium silicate binder (43.2% $Na_2O \cdot 2.88SiO_2$ solids, K-grade resin, PQ Corporation) was slowly added to the mixture and blended well. Although three different Cs_2WOS_3/sodium silicate weight ratio compositions were prepared (1:1, 1:1.6, and 1:2), most friction and wear experiments were performed on samples coated with the 1:1.6 composition. The amount of silicate binder was set in each case to give the required weight ratio. In each case, one drop of surfactant (Triton N-101) was added to the mixture. This resulted in a smooth yellow paste, which was subsequently transferred from the alumina mortar to a spray gun canister (Binks model 115).

Clean Si_3N_4 disks (typically four samples at a time) were affixed to a 45 by 30 cm board with masking tape and positioned vertically under a vent hood. The bonded coatings were applied to the polished surface of the samples by spraying with the gun at an air supply pressure of 0.38 MPa (55 psi). The gun nozzle was kept approximately 25 cm away from the sample surfaces during spraying. The samples were allowed to air dry for 1 hour and heated in an oven at 90, 110, and 120°C for 2 hours at each temperature.

20 µm

Prism-shaped
crystals

(a)

20 µm
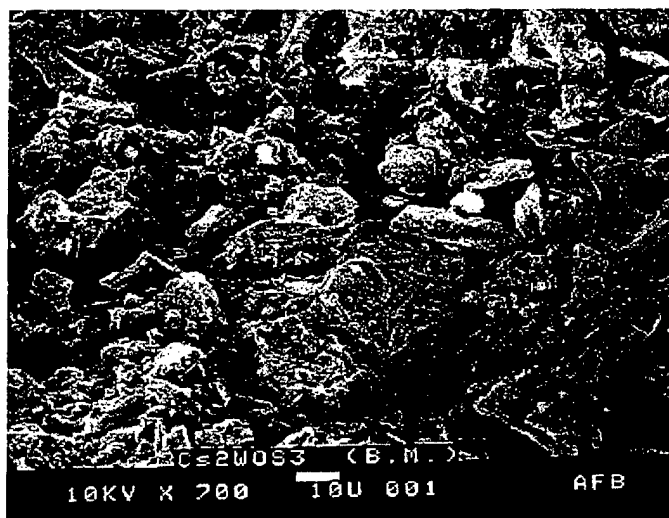
(b)

Figure 4. Cs$_2$WOS$_3$ Powder (a) As-Prepared and (b) After Ball Milling

12

Cured coated samples and one uncoated Si_3N_4 sample are shown in Figure 5. Upon cooling to room temperature, the thickness of each sample was measured from which the coating thickness was determined. The overall mean coating thickness was 41.8 ± 5.3 μm.

Although coating adhesion was not experimentally measured, it was clearly apparent that all bonded coatings adhered extremely well to the Si_3N_4 substrates with no evidence of coating delamination or flaking on any of the samples. Samples were wrapped in Kimwipe tissue and stored in labeled tin containers, which in turn were stored in an ambient laboratory environment.

2.3 Chemical Reaction Films

Previous research had indicated that the actual high temperature lubricating film was probably a glassy cesium silicate film of the form $Cs_2O \cdot xSiO_2$ formed by the reaction between the high-temperature decomposition products of cesium-based coatings and the SiO_2 scale on the Si_3N_4 substrates [29-31]. Therefore, attempts were made to form cesium silicate films in situ on Si_3N_4 substrates by immersing clean, pre-oxidized Si_3N_4 disks in a 50 wt.% cesium hydroxide (CsOH) solution. The original films were also applied by Dr. King. Si_3N_4 samples were initially measured and weighed in a microbalance prior to treatment. Pre-oxidation of the disks was conducted in air at 900°C for 3 hours using a ThermoLyne muffle furnace. The CsOH solution was prepared by slowly adding 100 g of CsOH monohydrate pure crystal (99% assay, Chemetall Gesellschaftt-Germany) to 100 g deionized water ($D.I.H_2O$). The resulting mixture was a clear solution.

The pre-oxidized Si_3N_4 disks were immersed in the CsOH solution and heated for 2 hours at 120°C. Samples were removed from the mixture and allowed to drain for 5 minutes on edge. Excess fluid was removed with Kimwipe tissue. The samples were air dried for 1 hour and dried in an oven for 2 hours at 100°C. Samples were given a final 1 hour anneal in air at 800°C. To prevent direct contact between the Si_3N_4 sample bottom and the alumina crucible during annealing, each sample rested on a platinum foil. Upon cooling to room temperature, samples were removed from the furnace, weighed and measured. Film thickness, determined by Auger electron depth profiling, was of the order of 0.17 μm. Samples were individually placed in clean tin containers and either stored in an ambient laboratory environment or in a vacuum dessicator. One of the most significant findings of the research resulted from a variation to the sample treatment and annealing process described above, which was developed by the author. This will be presented with the results
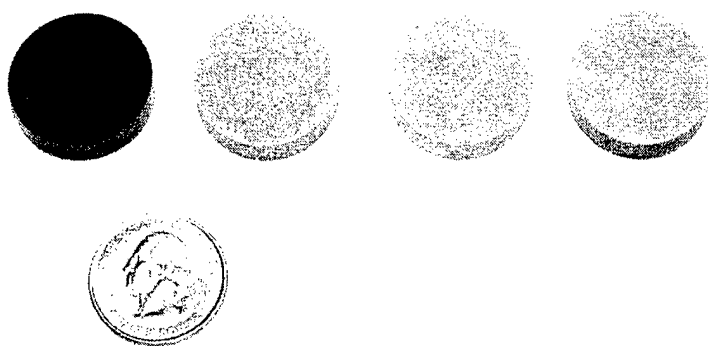
Figure 5. Uncoated Si$_3$N$_4$ and Sodium Silicate Cs$_2$WOS$_3$ Bonded Coated Samples

2.4 Friction and Wear Test Apparatus and Procedure

Friction and wear experiments were performed in laboratory air using a high-temperature ball-on-disk tribometer. A schematic of the tester and sample contact geometry are depicted in Figure 6. In this configuration, a stationary ball is loaded against a rotating disk by means of a hanging weight. For the present study, 0.635-cm diameter Si_3N_4 spheres were used. The sphere is held within a holder attached to a lever arm and the horizontal (tangential) force on the sphere is measured via a force gauge during disk rotation ($\pm$ 2.0 g accuracy). The force is calibrated to yield data on the friction force and friction coefficient. Wear occurs on the disk in the form of a groove or wear track and on the sphere whose area of contact is a worn circular flat or wear scar. The measured friction coefficient and disk rotation cycles are continuously recorded with a data acquisition system coupled to a computer using PC-Stripchart software. Data were acquired at a rate of one point per second, and friction coefficient calibration was performed periodically using a pulley-hang-down weight system.

For high temperature experiments, the samples were housed in a furnace with a split center or lid that permitted easy access to the samples. The air temperature surrounding the samples was monitored and controlled with a type K, chromel-alumel thermocouple positioned approximately 2.5 cm away from the sample contact point. This resulted in a slight temperature differential between the monitored and actual sample temperature, which was unknown during experimentation. Temperature calibration under static conditions indicated that a controller temperature set at 630°C yielded the desired sample temperature of 600°C. Samples were heated to 600°C at an approximate rate of 25°/min and were allowed to reach thermal equilibrium for 30 minutes prior to sample contact. The ball was brought into contact with the disk by lowering the lever arm support pillar 40 seconds prior to starting the drive motor.

New balls were used for each experiment while most disk samples tested at high temperature were used only once since exposing the sample to high temperature, particularly coated samples, was likely to affect subsequent friction and wear results. The number of replicate experiments varied and is reported with the results. The steady-state friction coefficient from each experiment was used to determine the average and standard deviation among each set. Unless otherwise stated, the nominal experimental test conditions were the following:

Applied load:	100 g (1.0 N normal force), 0.81 GPa initial Hertzian contact stress.
Linear sliding velocity:	0.080 m/s
Number cycles:	1300 to 20,000 .
Sliding distance:	40 to 615 m
Experiment duration:	30 to 45 minutes, typically
Sample temperature:	Uncoated samples; 23°C and 600°C
	Coated samples; 600°C
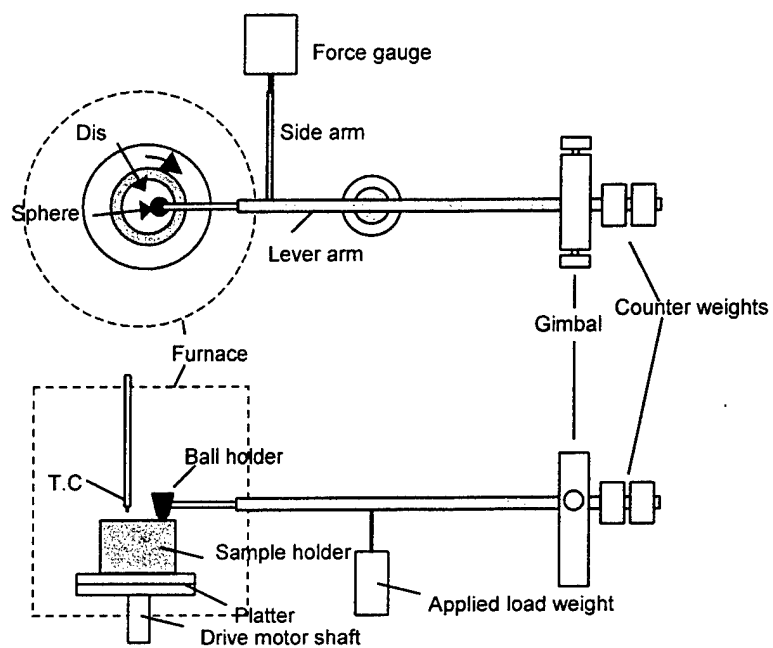
(a)
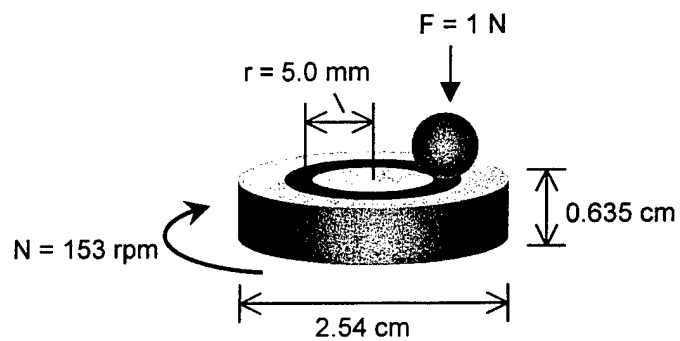
(b)

Figure 6 (a) Schematic: Ball-On-Disk Apparatus; (b) Sample Contact Geometry with Typical Operating Parameters

16

In experiments performed on coated samples, it was found that lower friction was obtained if the samples were given an initial 30-minute break-in at temperature. This involved running-in the samples for 900 cycles at low speed (0.014 m/s) and low load (10 g). This resulted in a very slight burnish on the coated disk and no measurable wear on the ball. Once completed, the ball and disk were brought out of contact, and the 10 g load was replaced with 100 g. The motor speed was then increased to the desired rpm and turned off prior to bringing the samples back into contact. Temperature was kept at 600°C during this process and the average time lapse between break-in completion and high-load, high-speed experiment startup was 4 minutes. Friction and wear results presented throughout this study are based on the high-load, high-speed portion of each experiment.

Relative humidity was not controlled but was closely monitored during each experiment. It averaged 18.6 ± 10.0 percent throughout the study. As will be shown later, a slight effect on friction and wear was observed on uncoated Si_3N_4 at room temperature, but no effect was noted at 600°C.

Most posttested samples were examined with a metallurgical optical microscope and a few selected ones were examined with an Amray model 1600 SEM. Wear surfaces of selected samples were also analyzed by Auger electron depth profiling, laser Raman spectroscopy, and FTIR spectroscopy. Because of the difficulty and uncertainty in measuring wear on the coated disks, wear is reported only for the balls and uncoated disks. Average wear on the balls was determined by taking three measurements of the wear scar diameter with an optical microscope fitted with a graduated reticle. The wear on the disks was measured using a Sloan DEKTAK surface profilometer and the arithmetic average of four measurements, taken 90° apart, was used. Measurements were converted to wear volume (mm^3) using simple geometric relationships and wear factors (mm^3/N m) were determined by dividing wear volume by the product of distance slid in meters and applied load in Newtons.

2.5 Analytical Techniques

The primary analytical techniques used to characterize surfaces of posttested samples included AES with depth profiling and laser Raman and FTIR spectroscopy. AES surface scans and depth profiles were obtained using a Varian model 981-2707 Auger electron spectrometer interfaced to a PC for data acquisition. Imaging of the sample was provided by a secondary electron detector. The average of three surface scans was typically used to determine the approximate atomic percent of elements outside and inside wear tracks. An argon ion gun was used to sputter etch the surface for elemental depth profiling. Unless otherwise noted, the argon ion beam energy was 2 keV and the sputter rate was approximately 80 Å/min. A 5-keV electron beam was used to excite the sample surface for Auger electron detection. The minimum electron beam spot diameter of the instrument was 10 μm; however, typical spot size was approximately 50 μm. AES is very surface sensitive and similar to other electron spectroscopies, it probes to a depth of about 10 to 30 Å. Si_3N_4 samples were masked with aluminum foil to prevent charging

during the analysis and to protect the surfaces from the ion-sputtering process. The AES data were acquired by Mr. Tom Wittberg of the University of Dayton Research Institute (UDRI).

Raman spectra were collected using a Renishaw 2000 confocal Raman microprobe. Samples were excited with a HeNe (632.8 nm) laser. This source was focused onto the sample using a 50X objective which produced an approximate beam diameter of 2 μm at the sample. Raman surface penetration depths range between 3 to 5 μm. Power at the sample did not exceed 6 milliwatts. The same objective was employed to collect the scattered radiation. Spectra were collected at 4 cm^{-1} resolution and represents the average of five individual scans. The integration time for each spectral element was 30 seconds.

Infrared spectra were collected with a Perkin-Elmer Autofocus infrared microscope interfaced to a Perkin-Elmer Spectrum 2000 FTIR spectrometer. The system employed a 250 by 250 mm, liquid nitrogen cooled, mercury cadmium telluride (HgCdTe) detector. Samples were analyzed using a 50 by 50 mm aperture. Each spectrum collected represents the average of 64 individual scans possessing a spectral resolution of 4 cm^{-1}. The Ge attenuated total reflection (ATR) accessory of the microscope was employed for sample analysis.

In those cases where a suitable sample thickness could not be obtained, the samples were analyzed with a Harrick Spilt-pea ATR microscope. This accessory employed a silicon internal reflection element (IRE) and the standard deuterium triglycine sulfate (DTGS) detector on the Spectrum 2000 macro bench. Spectra collected using this device represents the average of 32 individual scans possessing a spectral resolution of 4 cm^{-1}. The samples were brought into intimate contact with the IRE using a loading of 0.5 kg. Infrared surface penetration depths were less 1.0 μm in both cases. The Raman and FTIR data were acquired by Professor Andre Sommers of Miami University at Oxford.

3. FRICTION AND WEAR RESULTS

The high-temperature friction and wear results obtained on unlubricated (uncoated) Si_3N_4 sliding against itself and on two cesium-containing coatings applied to Si_3N_4 substrates are reported in this section. Experiments were performed in laboratory air, mostly at 600°C, using a ball-on-disk tribometer. Coatings studied included a sodium silicate ($Na_2O\,3SiO_2$) bonded Cs_2WOS_3 coating and a cesium silicate chemical reaction film. Wear factors were determined using optical microscopy and surface profilometry measurements and wear mechanisms were studied by optical microscopy and SEM. Results obtained on uncoated Si_3N_4 are presented first.

3.1 Unlubricated Silicon Nitride

The friction and wear of uncoated Si_3N_4 was studied in detail to establish a baseline for comparing the performance of coated samples. The results obtained at 23°C and 600°C are summarized in Table 3 and Figures 7 and 10. The steady-state mean friction coefficients (μ_m) obtained at 23°C and 600°C were 0.70 ± 0.09 and 0.80 ± 0.03, respectively. Although friction was slightly higher at 600°C, the mean value was not statistically different from that obtained at room temperature. Experimental variance was higher at room temperature, though. The variance may have been caused by the variation in laboratory relative humidity, as shown in Figure 8. It has been shown that the friction of unlubricated Si_3N_4 decreases slightly with increasing relative humidity [35-38]. Nevertheless, the mean friction coefficient values obtained here agree very well with those cited in the literature for unlubricated Si_3N_4 materials tested in low-humidity air environments [35-40]. Typical friction traces at both temperatures are shown in Figure 9.

Mean wear factors obtained on the balls and disks at 23°C and 600°C are also given in Table 3 and graphically represented in Figure 10. Typical surface profilometry traces obtained on disks wear tracks are shown in Figure 11. At 23°C, wear factors were of the order of 10^{-5} mm^3/N m, and balls wore at about the same rate as the disks. Wear of balls and disks was significantly higher at 600°C, and in this case, disks wore at a higher rate. Mean wear factors at 600°C were approximately 10^{-4} and 10^{-3} mm^3/N m for the balls and disks, respectively. Similar to friction, variance in the wear data was higher at 23°C. However, there was no apparent correlation between humidity and wear rate for the range of laboratory humidity conditions experienced in these experiments. This is shown in Figure 12. The wear factor values obtained, however, also compare favorably with those reported in the literature for unlubricated Si_3N_4 tested under similar conditions [38]. In general, the friction and wear values obtained here fall within the regime associated with the severe wear of Si_3N_4, where typical friction coefficients and wear factors range between 0.4 to 0.8 and 10^{-6} to 10^{-3} mm^3/N m, respectively.

Typical wear scars and corresponding wear tracks of sample sets tested at 23°C and 600°C are shown in the optical micrographs of Figure 13. SEM micrographs taken inside the wear track of a sample tested at 600°C are shown in Figure 14. Generally, there was hardly any visible wear debris at 23°C, and ball wear scars and disk wear tracks were, on occasion, partly covered with thin films that displayed interference colors when observed

Table 3. Friction and Wear Results of Unlubricated Si_3N_4 on Si_3N_4				
$V_s = 0.08$ m/s, F = 1.0 N load				
Temperature (°C)	Mean Friction Coefficient[*†]	Mean Wear Factor[†] (mm^3/N m)		Avg. R.H. (%)
		Ball	Disk	
23	0.70 ± 0.09 (avg. of 10 exp.)	1.2×10^{-5} ± 6.6×10^{-6}	7.9×10^{-6} ± 4.9×10^{-6}	27.3
600	0.80 ± 0.03 (avg. of 4 exp.)	9.3×10^{-5} ± 1.2×10^{-5}	1.7×10^{-3} ± 3.3×10^{-4}	12.9

* Mean steady-state friction value reported (typically achieved after 1000 cycles).
† Standard deviation given
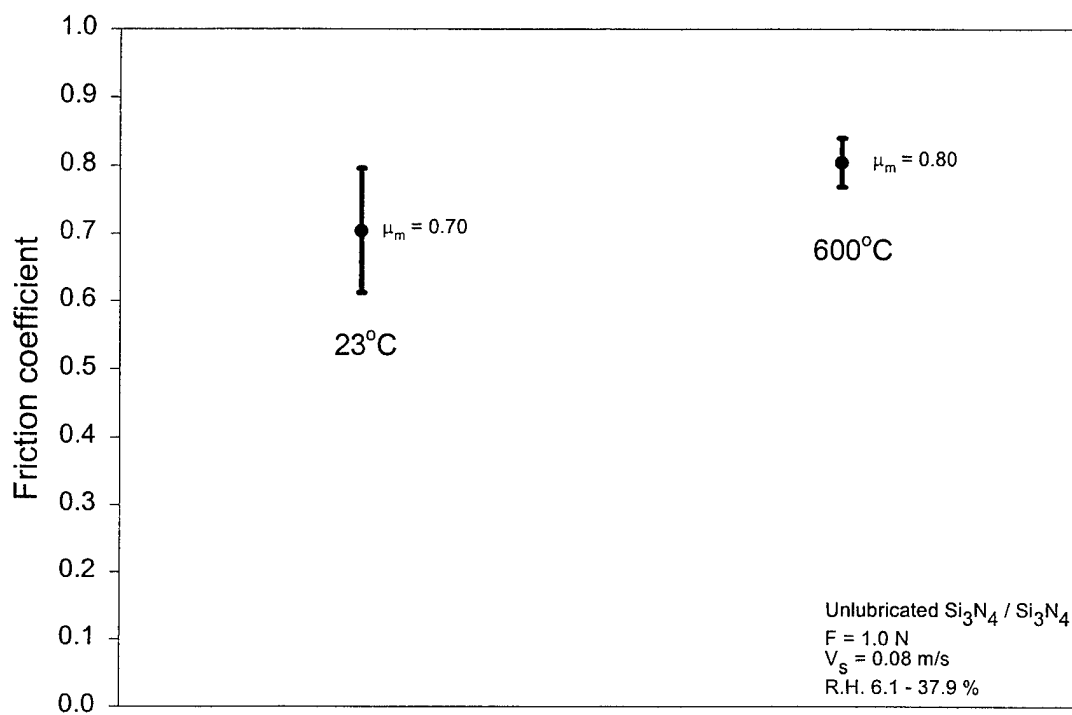
Figure 7. Mean Friction Coefficient and Standard Deviation of Unlubricated Si_3N_4 at 23°C and 600°C
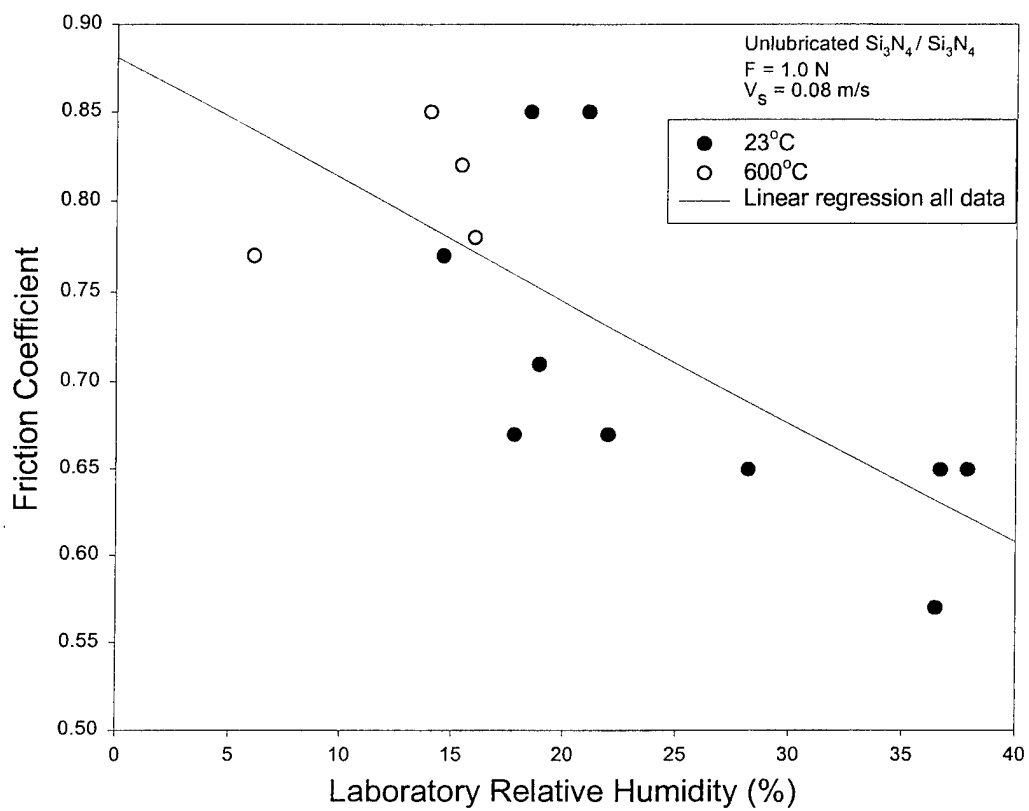
Figure 8. Effect of Laboratory Relative Humidity on Friction Coefficient of Unlubricated Si_3N_4
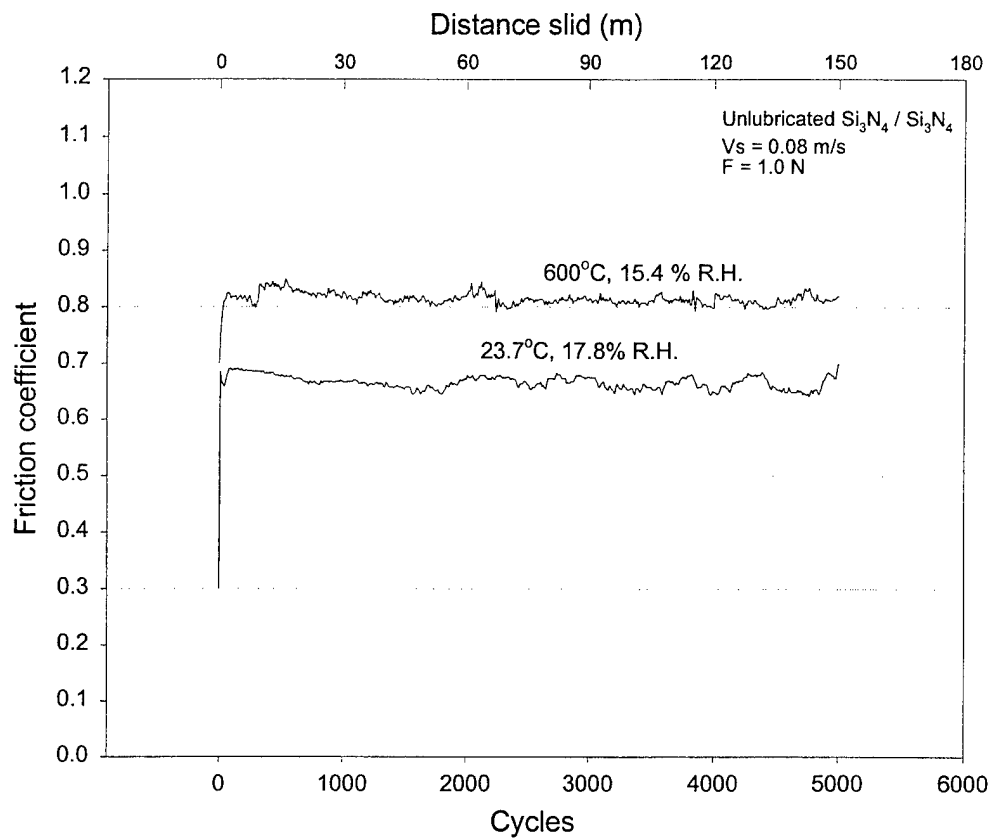
Figure 9. Friction Coefficient of Unlubricated Si_3N_4 at 23°C and 600°C as a Function of Cycles and Sliding Distance
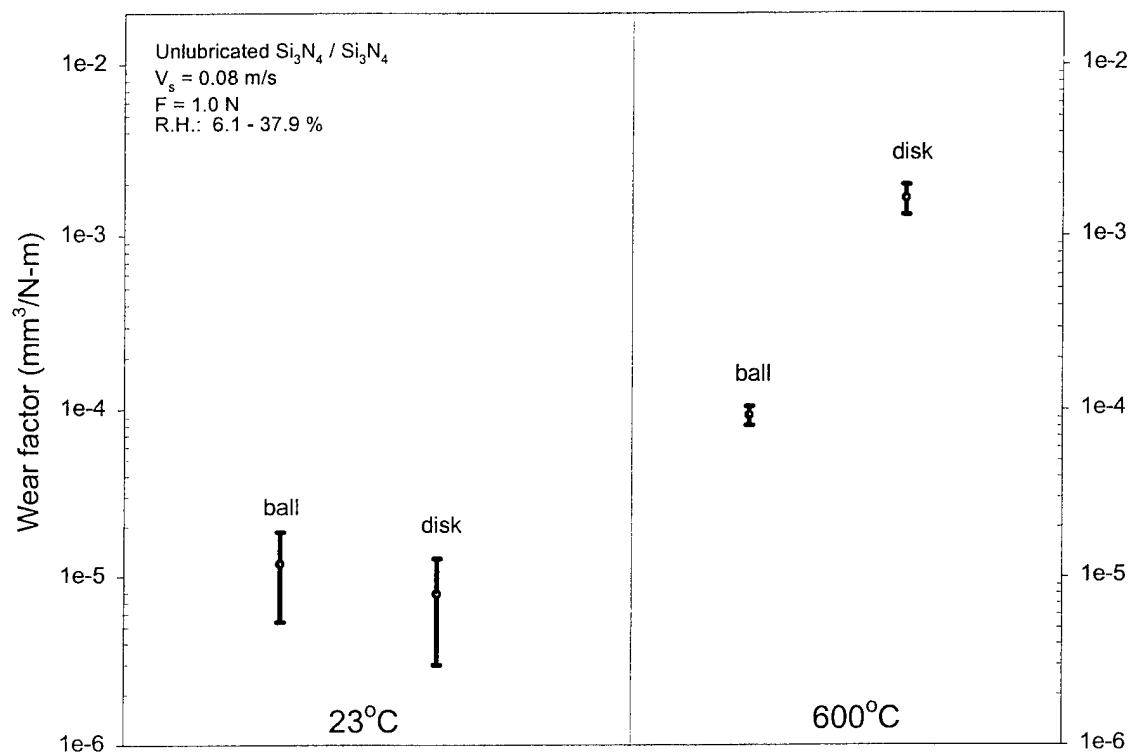
Figure 10. Mean Wear Factors and Standard Deviation of Unlubricated Si_3N_4 at 23°C and 600°C

ID:0078   SCAN: 2MM   VERT:-56 A
14:16 02-02-01 SPEED: MEDIUM   HORIZ: 1,175µM

(a)

ID:000201   SCAN: 2MM   VERT:-233 A
10:15 12-05-00 SPEED: MEDIUM   HORIZ:-1,992µM
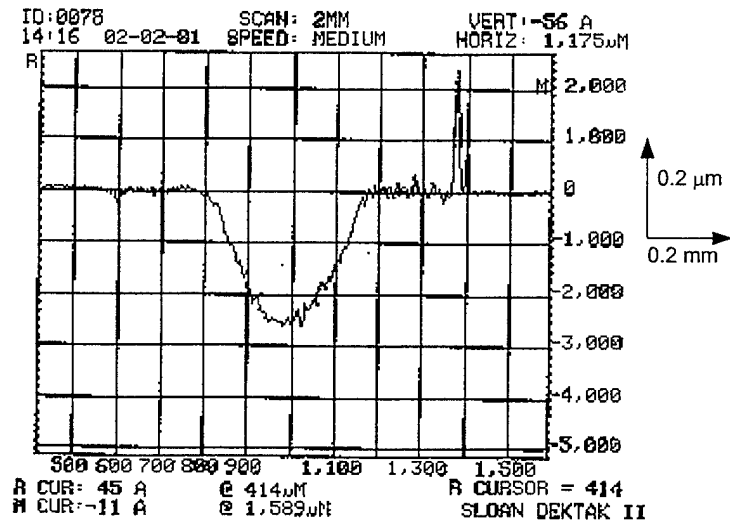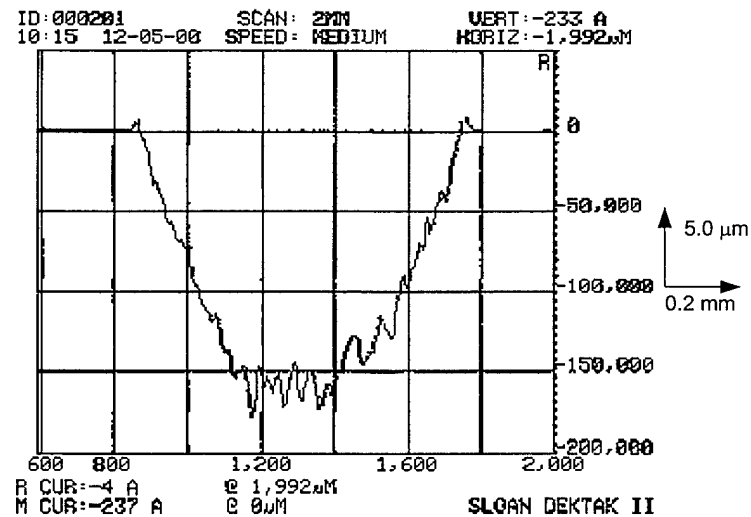
(b)

Figure 11. Surface Profilometry Traces of Disk Wear Tracks

Note: Unlubricated Si_3N_4 at (a) 23°C and (b) 600°C. V_s = 0.08 m/s, F = 1.0 N.

25
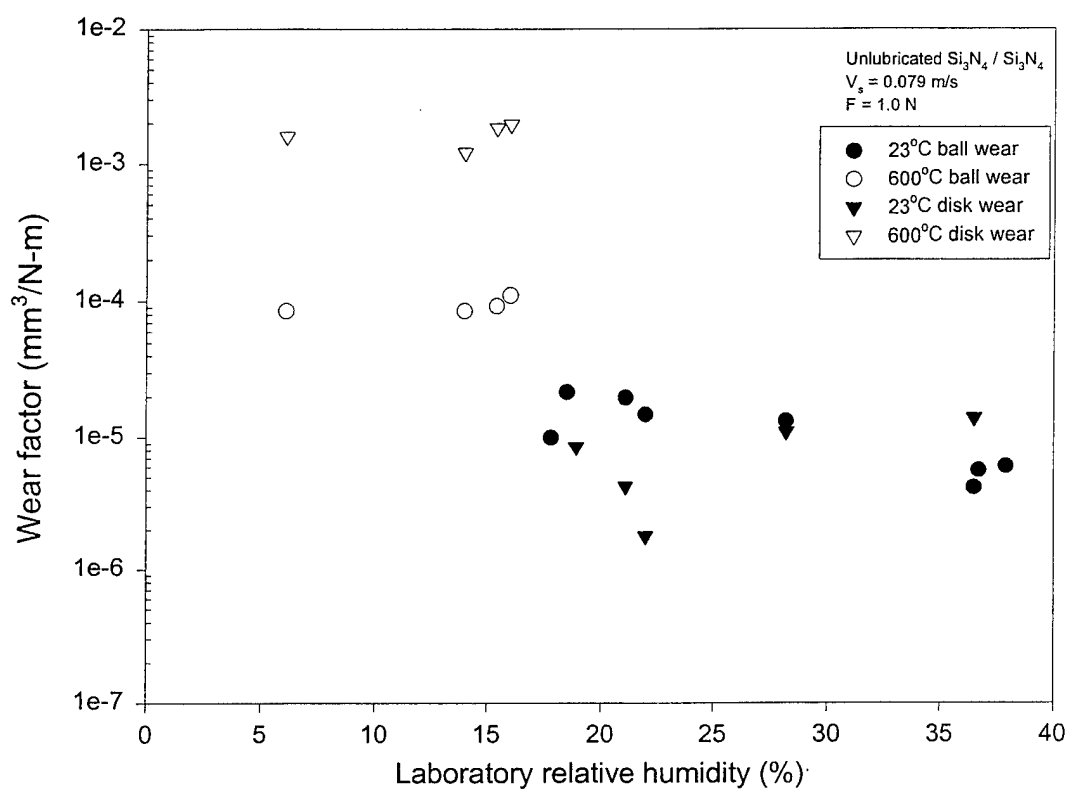
Figure 12. Effect of Laboratory Humidity on Wear of Unlubricated Si_3N_4 at 23°C and 600°C
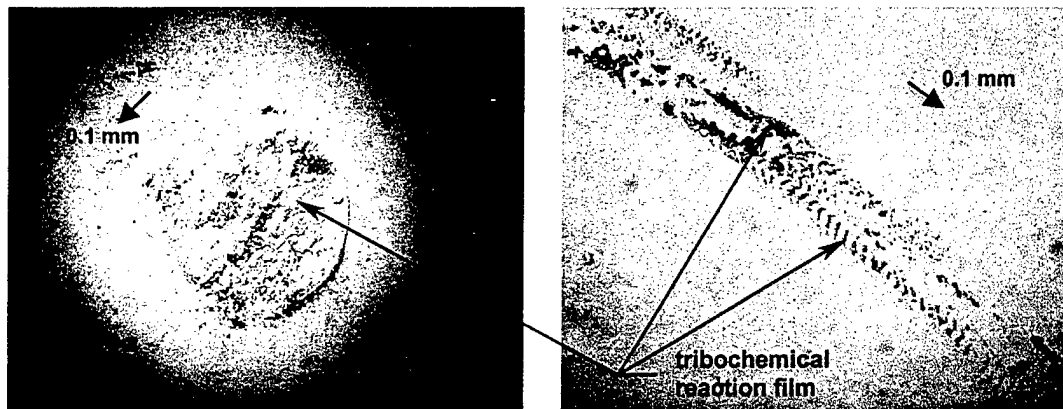
(a)
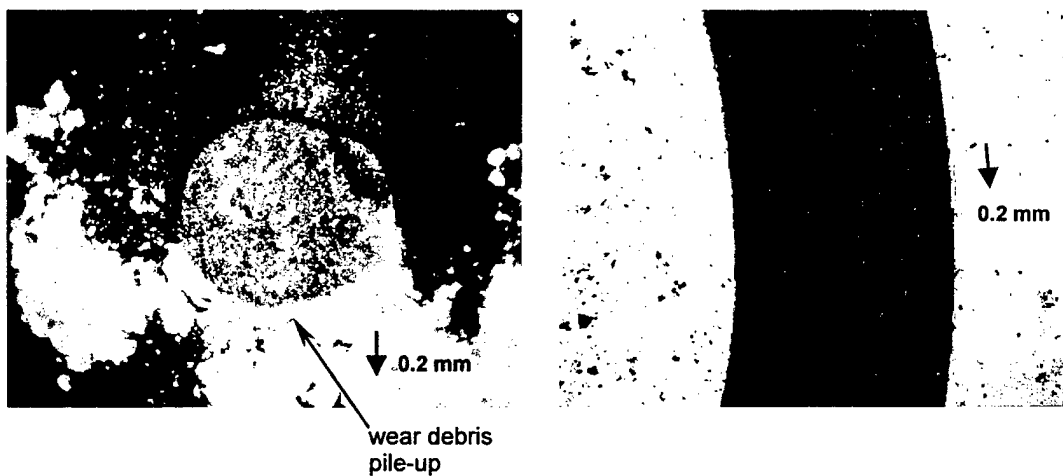
(b)

Figure 13. Optical Micrographs of Ball Wear Scars (Left) and Disk Wear Tracks (Right) of Unlubricated Si₃N₄, (a) 23°C and (b) 600°C

Note: Arrow indicates relative ball sliding direction and scale. V_s = 0.08 m/s, F=1.0 N.

20 μm

sliding
direction   5 μm
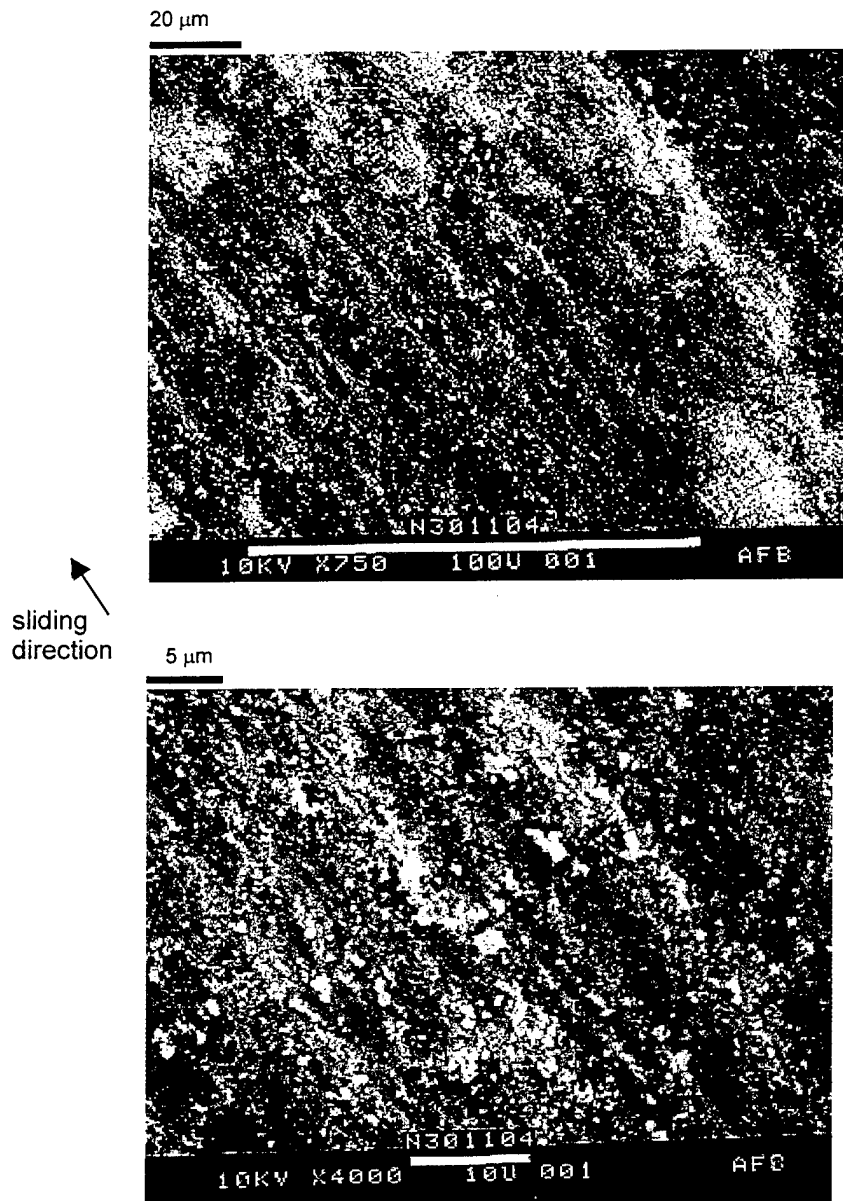
Figure 14. SEM of Inside Wear Track of Unlubricated Si_3N_4 Tested at 600°C Showing
Fine Wear Debris From Microfracture

Note: V_s = 0.08 M/S, F = 1.0 N.

under reflected white light. This is shown in Figure 13a for a sample that was tested at 23°C and 37 percent relative humidity. Fragmented transfer films that have been smeared along the wear track are clearly visible on the disk. Similar films have been noted by others and it is now well established that Si_3N_4 forms a soft protective layer, believed to be amorphous hydrated silica, during sliding in humid air [35-37, 42, 43]. These thin surface films are the product of tribochemical reactions between the Si_3N_4 substrate, oxidized and pulverized wear debris, and ambient water vapor. The soft layers reduce and redistribute the local contact stresses and protect the surfaces from gross wear by accommodating surface shear stresses [36, 43]. FTIR analysis performed on the surface film shown in Figure 13a (right) shows an increase in Si-O and Si-OH species suggesting the formation of hydrated SiO_2.

The amount of visible wear debris was considerably higher at 600°C, in agreement with the measured wear data. The increased wear is clearly evident from the surface prolilometry traces shown in Figure 11 and photomicrographs of Figures 13 and 14. As shown in Figure 13b, wear debris consisted of very fine white dust-like particles which could easily be removed when rubbed. Unlike at 23°C, no surface films were visible on samples tested at 600°C and wear surfaces were dull grey and rough with patches of white wear debris. The rough surfaces obtained at 600°C and the presence of very fine wear debris indicate that wear occurred predominately by microfracture as described by Fisher and Tomizawa [35, 36]. The SEM micrographs shown in Figure 14 support this observation.

In all cases, particularly at 600°C, the wear debris traveled with the ball and formed a small pile that accumulated ahead of the sliding direction (i.e., at the inlet rim region of the contact zone). This is shown in Figure 13b. This has been observed before on Si_3N_4 sliding in dry environments and according to Fisher et al. [36], the wear debris causes the disk to wear by third body abrasion. This results in higher wear rates on the disk. This would explain the higher wear rates observed on disks tested at 600°C, where very low humidity conditions were favored.

3.2 Solid Lubricated Silicon Nitride

3.2.1 Cesium Oxythiotungstate Bonded Coatings

The friction and wear results obtained at 600°C on Cs_2WOS_3 bonded coated samples are summarized in Table 4 and Figures 15 to 18. Results for uncoated Si_3N_4 are also presented for comparison. Experiments were performed in two time series, 7 months apart. During the early part of the research, it was found that low friction coefficients were only obtained when coatings were given an initial 30-minute running-in at a low load (0.01 N), low speed (0.015 m/s), and at temperature (600°C). The procedure is described in detail in the experimental section. The mean friction results reported and discussed throughout this study were obtained from the steady-state values of the high load (1.0 N), high speed (0.08 m/s) segment of each experiment.

A μ_m of 0.49 ± 0.30 was obtained on silicate bonded Cs_2WOS_3 coatings without running-in (group A), while those from the first experimental series with running-in (Group B), conducted during the March to April 2000 timeframe, gave a μ_m of 0.17 ± 0.07. A reduction in the mean friction value and in the data scatter is clearly evident for samples that were given the running-in. Interestingly, samples from the same coating batch tested seven months later (Group C) performed poorly in terms of friction despite the initial running-in. Friction coefficients were abnormally high for this group (higher than uncoated Si_3N_4) with $\mu_m = 1.08 ± 0.23$. These results imply that the coating changed during the time period between Group B and C experiments. Unfortunately, surface analysis was only performed on an aged sample and not on a fresh, as-coated one. The analysis of the aged sample revealed that a layer containing sodium carbonate had formed on its surface. Posttest inspection under the optical microscope also revealed that remnants of coating material were still present inside the wear track of four out of five of the Group C samples, unlike all previous samples where the coating was completely worn through. Optical micrographs showing this will be presented later. Also, there was no visible wear scar on two of the five balls.

All of the bonded coatings exposed to high temperature underwent a color change from yellow-green to a dull grey color, indicating that a thermally induced reaction (i.e., oxidation, phase change, or decomposition) had taken place. TGA and differential thermal analysis (DTA) of Cs_2WOS_3 powder indicate that this material undergoes a series of complex oxidation reactions between 315 and 600°C. Raman and FTIR spectroscopy show that destruction of the $[WOS_3]^{2-}$ anion is complete by 600°C. The decomposition products that are formed melt at about 770°C. Thermal decomposition mass spectroscopy (TDMS) also shows that sulfur is evolved from Cs_2WOS_3 at about 80°C and between 300 and 600°C with S_2, S_4, and S_6 type species being detected. The addition of the sodium silicate binder significantly affects its thermal behavior and seems to protect it from oxidation, perhaps by serving as a glass encapsulate. These results are described in full in the Appendix B.

Figure 16 shows typical friction traces obtained on all three of the Cs_2WOS_3 bonded coated groups. The shape of individual friction curves was very consistent within Groups B and C and were generally similar to those shown in Figure 16. Friction curves from Group A, however, varied in shape. Two representative types are shown in Figure 16. For Group B, friction would generally start at a moderate to low value (0.2 to 0.3), remain steady or decrease somewhat during the first several hundred cycles, increase to a maximum, and finally decrease to a very low steady value. The maximum μ in Group B friction curves was usually between 0.3 and 0.4. The shape of Group B friction curves are typical of those characterized by a break-in period as defined by Blau [44]. In this case, it appears that the break-in resulted in the formation of a lubricious film with a friction coefficient of about 0.10. For Group C, friction would normally start at a moderate to high value (0.4 to 0.6) and increase to a steady value of about 1.2.

Because the bonded Cs_2WOS_3 coatings were relatively thick, it was very difficult to establish the exact location of the substrate reference surface for profilometry wear measurements. Hence, only wear of the balls is reported for these samples. Mean wear

Table 4. Friction and Wear Results of Sodium Silicate Bonded Cs₂WOS₃ Coated Samples Si_3N_4 coated disk sliding against uncoated Si_3N_4 ball T=600°C, V_s = 0.08 m/s, F = 1.0 N load			
Coating System	Mean Friction Coefficient[b,c]	Mean Wear Factor of Ball[c,d] (mm³/N m)	Avg. R.H. (%)
Uncoated Si_3N_4 substrate	0.80 ± 0.03 (avg. of 4 exp.)	9.3×10^{-5} ± 1.2×10^{-5}	12.9
Cs₂WOS₃ coating with no running-in (Group A)	0.49 ± 0.30 (avg. of 4 exp.)	1.9×10^{-6} ± 1.1×10^{-6}	14.5
Cs₂WOS₃ coating with running-in (Group B)[a]	0.17 ± 0.07 (avg. of 12 exp.)	1.0×10^{-6} ± 4.2×10^{-7}	19.1
Cs₂WOS₃ coating with running-in (Group C)[a]	1.08 ± 0.23 (avg. of 5 exp.)	1.6×10^{-6} ± 6.6×10^{-7} (avg. of 3 exp.)	26.7

[a]Time lapse between Group B and C experiments was 7 months.
[b]Mean steady-state (s.s.) friction value reported. Number of cycles to s.s. varied in each case.
[c]Standard deviation given.
[d]Wear on bonded coated disks is not reported due to high uncertainty in profile measurements.
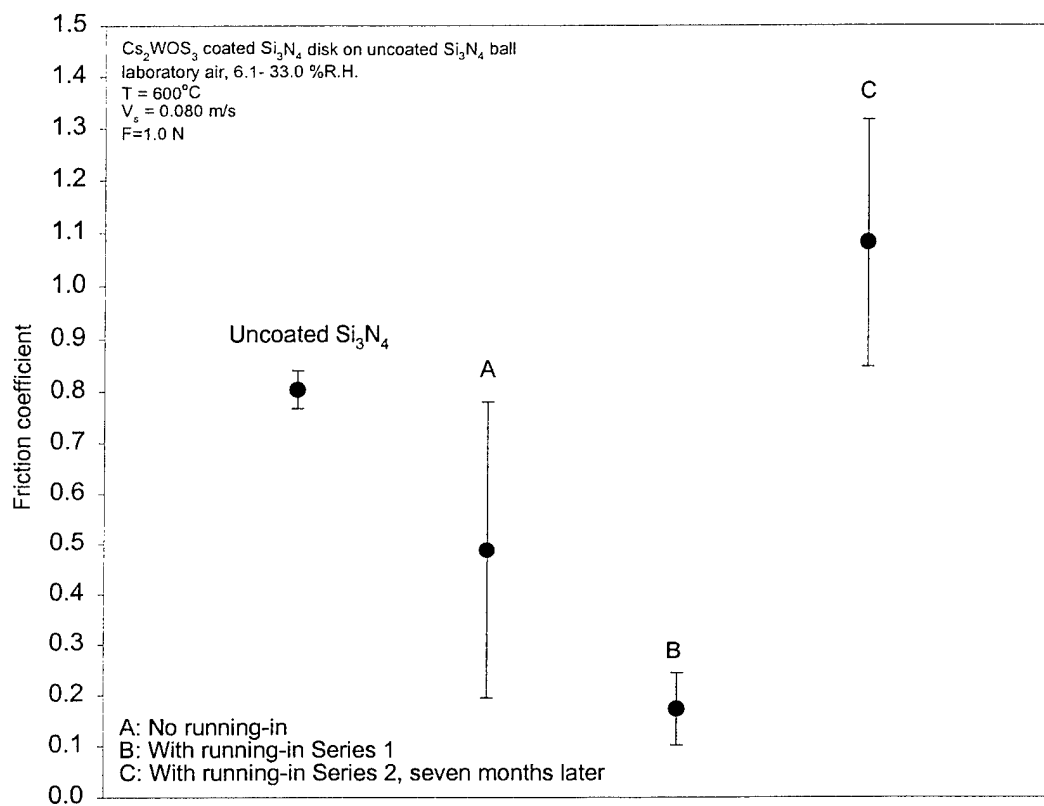
Figure 15. Mean Friction Coefficients and Standard Deviation of Cs_2WOS_3 Bonded Coatings at 600°C
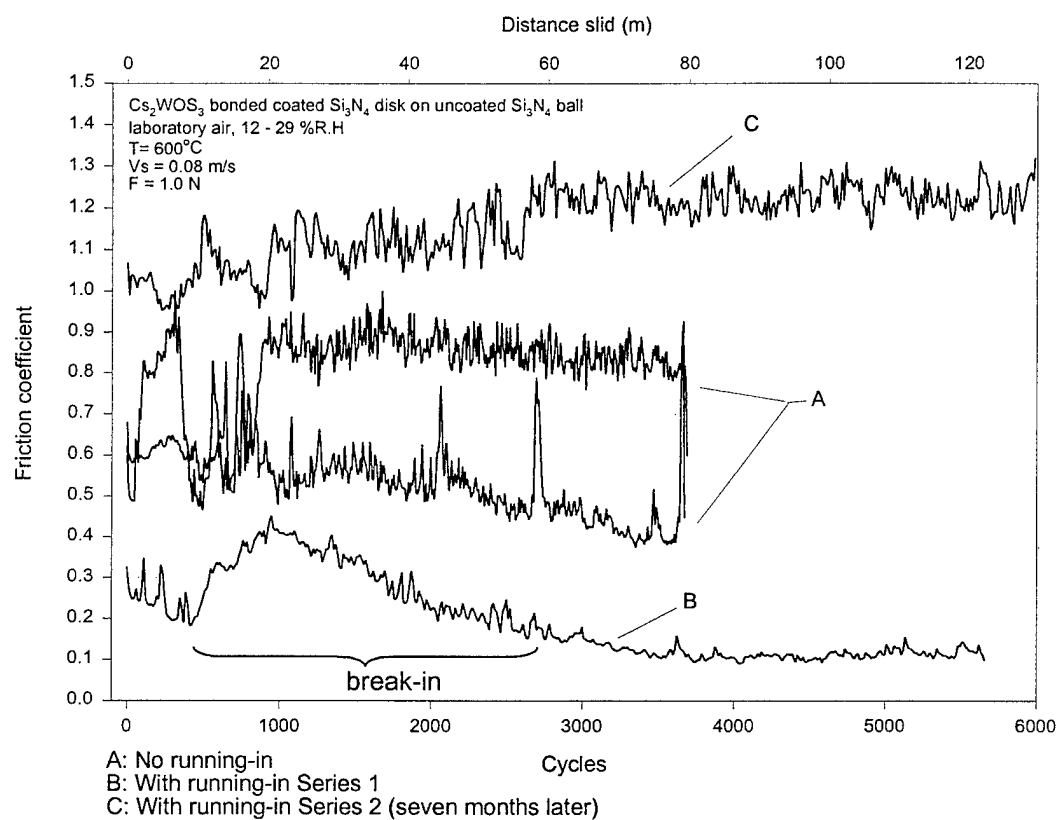
Figure 16. Friction Coefficient of Bonded Cs_2WOS_3 Coatings on Si_3N_4 as a Function of Cycles and Sliding Distance

factors are given in Table 4 and shown in Figure 17. For the Group C samples, the mean wear factor is based on the three balls that exhibited wear scars.

Two experiments were intentionally suspended after completing the 30-minute running-in to visually inspect the extent of wear on balls and disks. There was a light halo on the balls but very little coating debris and no visible wear scar. Coated disks exhibited a very slight burnish that was barely noticeable. As a result, the running-in portion of each experiment was not considered in the wear rate calculations.

As shown in Figure 17, a significant reduction in ball wear rate is apparent for all of the bonded coated groups when compared to uncoated Si_3N_4 at 600°C (about two orders of magnitude lower). The wear rate of balls that were slid against coated samples was approximately 10^{-6} mm^3/N m and was about the same for all three bonded coated groups, including Group C, which gave very high friction. This suggests that the running-in process used here had little effect on the wear rate and that the wear response is decoupled from the frictional response. In other words, the wear mode of balls appears to be insensitive to the parameters or factors influencing the frictional response.

Optical micrographs of typical wear scars and corresponding wear tracks of samples from Groups A and B are shown in Figure 18. Also shown in this figure is a sample from Group C in which the coating was completely worn through. As previously noted, four of the Group C samples had segments of coating residue still attached to the substrate inside the wear track. This is shown in Figure 19 for one sample. All of the other bonded coatings (Groups A and B) were worn through, and contact between ball and disk substrate surfaces was apparent. Considerable coating film transfer to the balls was evident in all cases and ball wear scars usually exhibited debris pileup at the leading edge of the contact (ahead of the sliding direction) and toward the sides. Figure 20 clearly exemplifies this phenomenon. The compacted debris appeared brittle and glassy-like and often displayed cracks running across it. There was usually less of this debris on the trailing edge side.

As shown in Figure 21, wear surfaces generally displayed three major zones associated with the wear process. A highly polished load bearing zone in the center or primary wear track, a film transfer zone at the immediate edges of the primary wear track, and outer wear debris transfer zones. Areas surrounding the wear scars on balls also displayed features that dimensionally correlated well with these three areas as depicted in these figures. It is clear from these observations that contact between balls and disks was not confined to a small area (i.e., primary load bearing zone and wear scar), but rather to a relatively large one that involved extensive interaction between compacted coating debris attached to the balls and the aforementioned areas on the coated disks. This is to be expected for a system involving a hard slider rubbing against a relatively thick and soft coating on a hard substrate.

Group B primary wear tracks were often more well defined and narrower than others. However, all surfaces showed the presence of optically active surface films, which when observed under reflected white light, displayed interference colors. Blue and
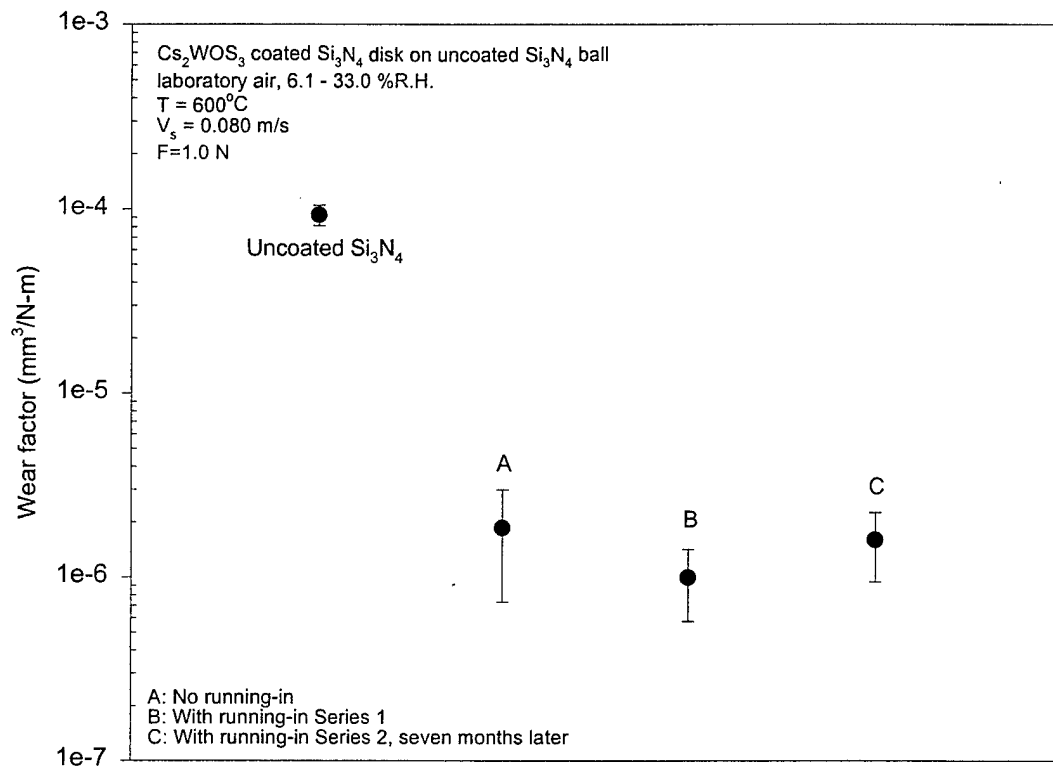
Figure 17. Mean Wear Factors and Standard Deviation of Balls Slid Against Cs_2WOS_3 Bonded Coated Disks at 600°C
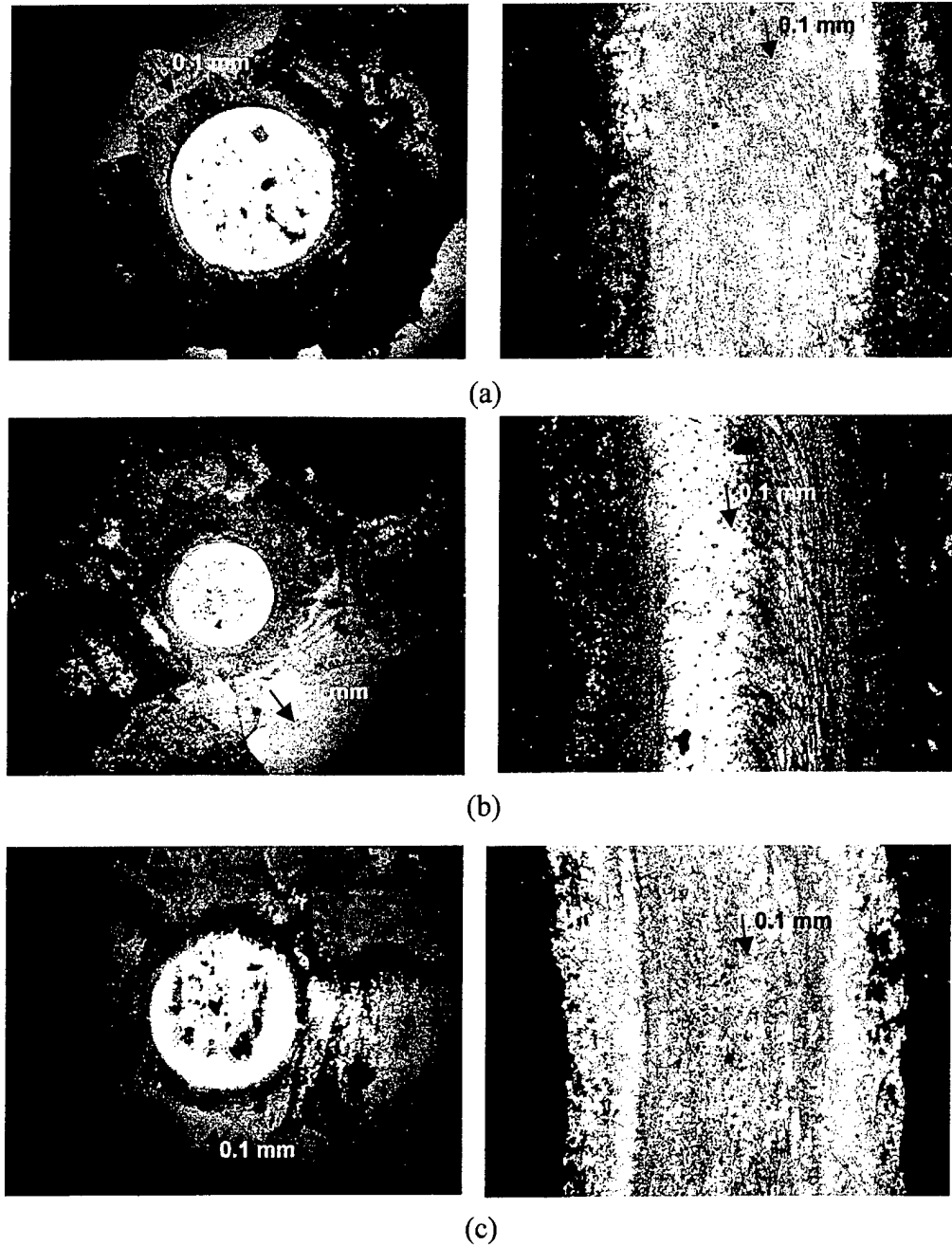
Figure 18. Optical Micrographs of Typical Ball Wear Scars (Left) and Wear Tracks (Right) of Cs_2WOS_3 Bonded Coated Samples

Note: (a) Group A - no running-in, (b) Group B - with running-in time Series 1, and (c) Group C – with running-in time Series 2. Arrow indicates relative ball siding direction and scale. F = 1.0 N, V_s = 0.08 m/s, and T = 600°C.
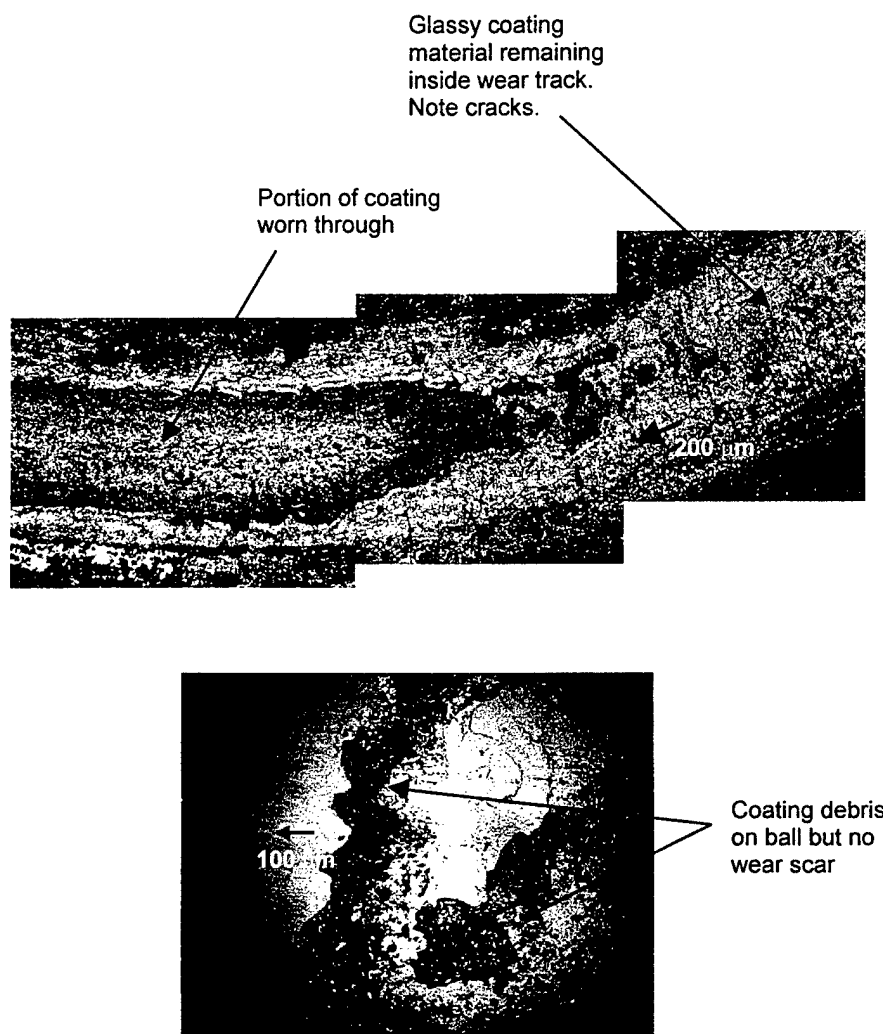
Figure 19. Optical Micrograph of Wear Track (Top) and Ball (Bottom) of Cs_2WOS_3 Bonded Coated Sample Set from Group C

Note: Coating remained within portions of the wear track after sliding. $\mu_{s.s.} = 0.98$ at F = 1.0 N, $V_s = 0.08$ m/s, and T = 600°C. Small arrow indicates relative ball sliding direction and scale.
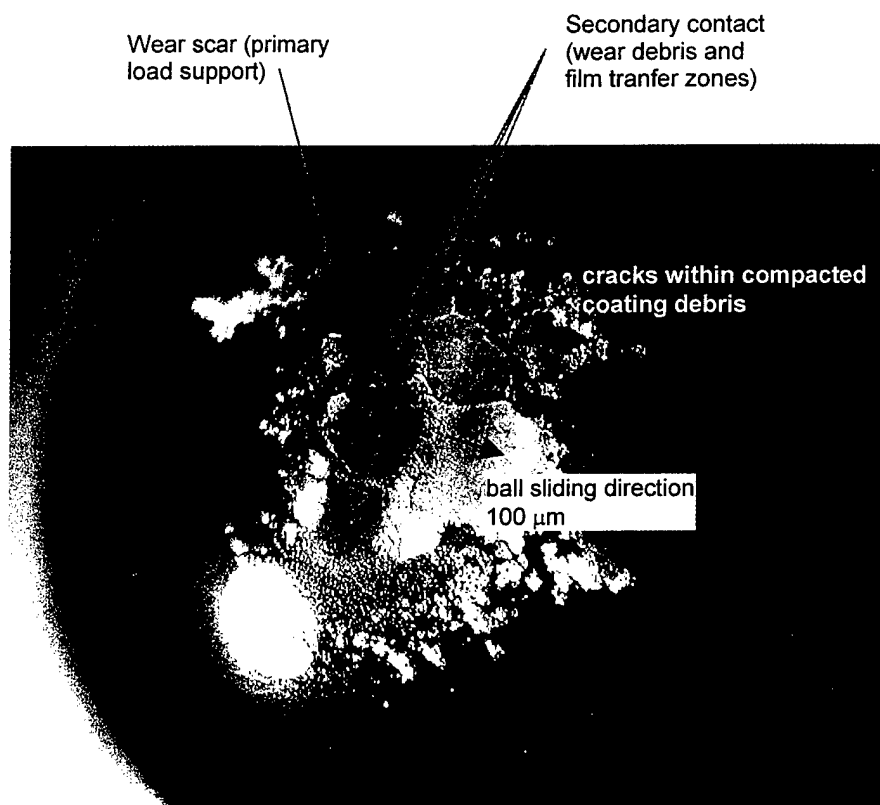
Figure 20. Typical Ball Showing Coating Debris Surrounding Wear Scar after Sliding Against Cs_2WOS_3 Bonded Coated Disk
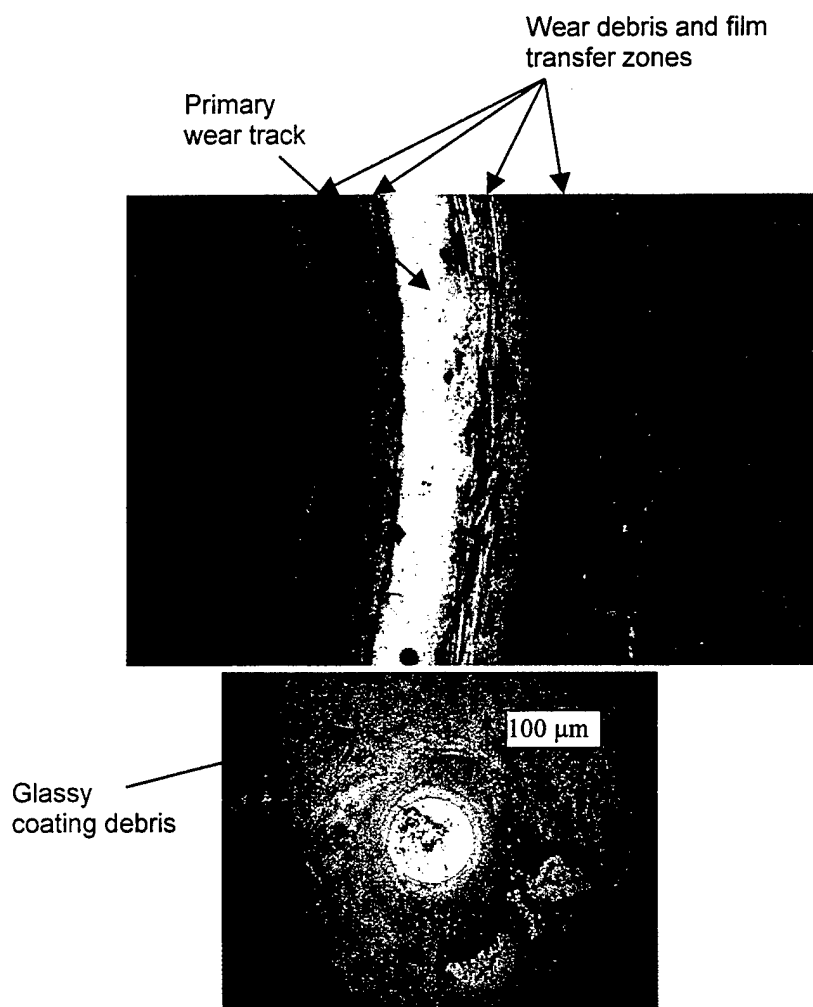
Figure 21. Wear Track (Top) and Ball Wear Scar (Bottom) of Cs_2WOS_3 Bonded Coated Sample Set from Group B Showing Distinctive Wear Zones

Note: $\mu_{s.s.} = 0.087 \pm 0.02$ at $F = 1.0$ N, $V_s = 0.08$ m/s, and 600°C. Small arrow indicates relative ball sliding direction and scale.

brown films were prominent at the edges of the primary wear track and thicker films (higher order coloring) were present within the outer wear debris zones. This is shown in Figure 21 for a sample from Group B that gave low friction ($\mu = 0.09$). Sliding marks across the blue and brown films are clearly visible throughout the edges of the primary wear track. These are believed to be caused by coating debris trapped ahead of the ball which is subsequently dragged and pushed aside during sliding.

Primary wear tracks and ball wear scars were usually highly polished. A profilometry trace obtained inside the ball scar of one sample set gave an R_a value of 2.4 nm. Also, primary wear tracks and wear scars often exhibited peculiar patterns and dendritic-like features which displayed considerable interference coloring. This is shown in Figure 22 for the same sample previously shown in Figure 21, but in a different area. Some of these features seemed to have been in the liquid state. The random and irregular shape and the absence of smearing marks along the sliding direction suggests that these were formed after sliding, probably during cooling.

3.2.2 Chemical Reaction Films

The primary objective of this part of the research was to investigate the high-temperature sliding friction and wear characteristics of cesium silicate films. If good lubricating behavior was observed, then this would lend support to our hypothesis that reactions between cesium-based coatings and the silicon dioxide scale on Si_3N_4 produces a lubricious cesium silicate glassy film. Because of the significant findings encountered during this part of the research, it is appropriate to briefly review the process in which the silicate films were produced.

The original films were applied by Desilube Technology, Inc. and were formed by immersing pre-oxidized Si_3N_4 samples in a 50 percent CsOH solution and annealing in air at 800°C for 1 hour. The annealing was done in open alumina crucibles in a muffle furnace. Initial friction coefficient on all of these samples was very high ($\mu > 0.6$), with the exception of one sample. This is shown in Figure 23. A steady-state friction coefficient of about 0.10 was obtained on this particular sample. Surprisingly, Auger electron surface analysis revealed the presence of sulfur and high surface carbon levels inside the wear track of this sample. These results are presented in the next section. It is believed that the source of the sulfur contaminant was from residual material that remained within the tribometer from a previous high-temperature (600°C) experiment conducted on a sample burnished with WS_2. This is also supported by the shape of the friction trace, which implies that the lubricating film was formed during sliding (i.e., initial moderate friction followed by a sudden drop in friction). Polishing of the ball and wear track surfaces could also cause a decrease in friction, and in fact, posttested surfaces appeared polished. The source of the carbon could be attributed to surface contamination or to the thin SiC layer found on the substrate. These results suggest that sulfur plays a role in the formation of a lubricious film.
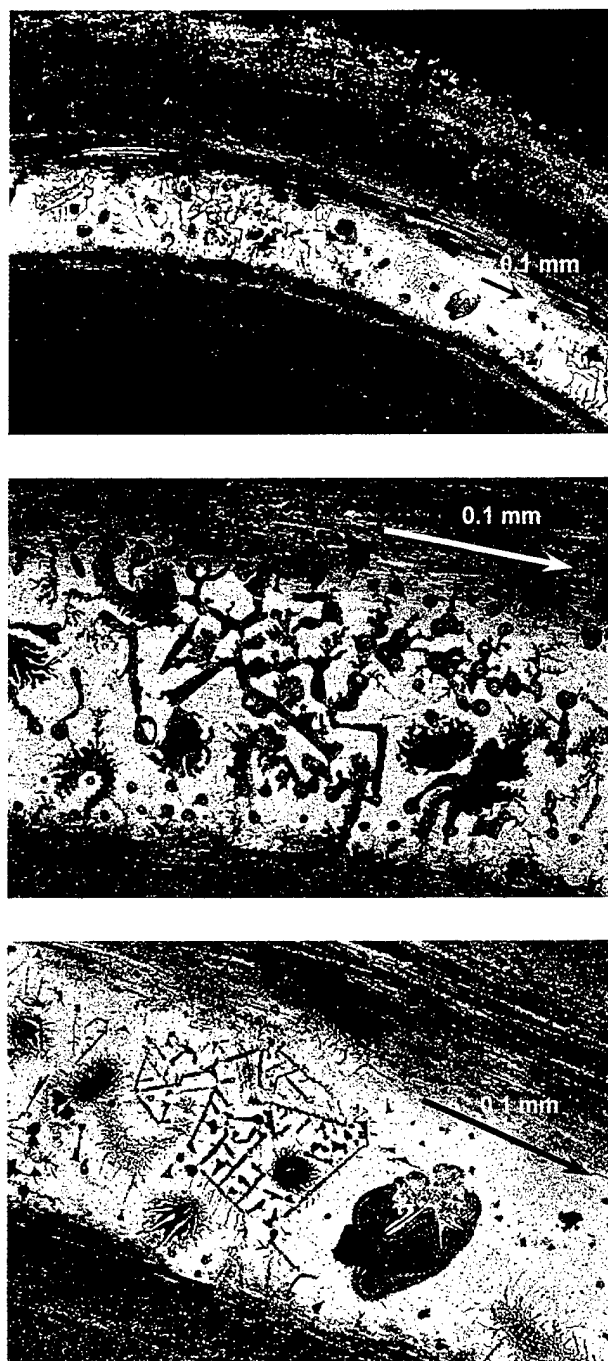
Figure 22. Dentritic and Starlike Patterns Exhibiting Interference Colors Inside Wear Track of Cs_2WOS_3 Coated Sample that Exhibited Low Friction

Note: $\mu_{S.S.}$ = 0.09 at F = 1.0 N, V_s = 0.08 m/s. Arrow indicates relative ball sliding direction and scale.

41
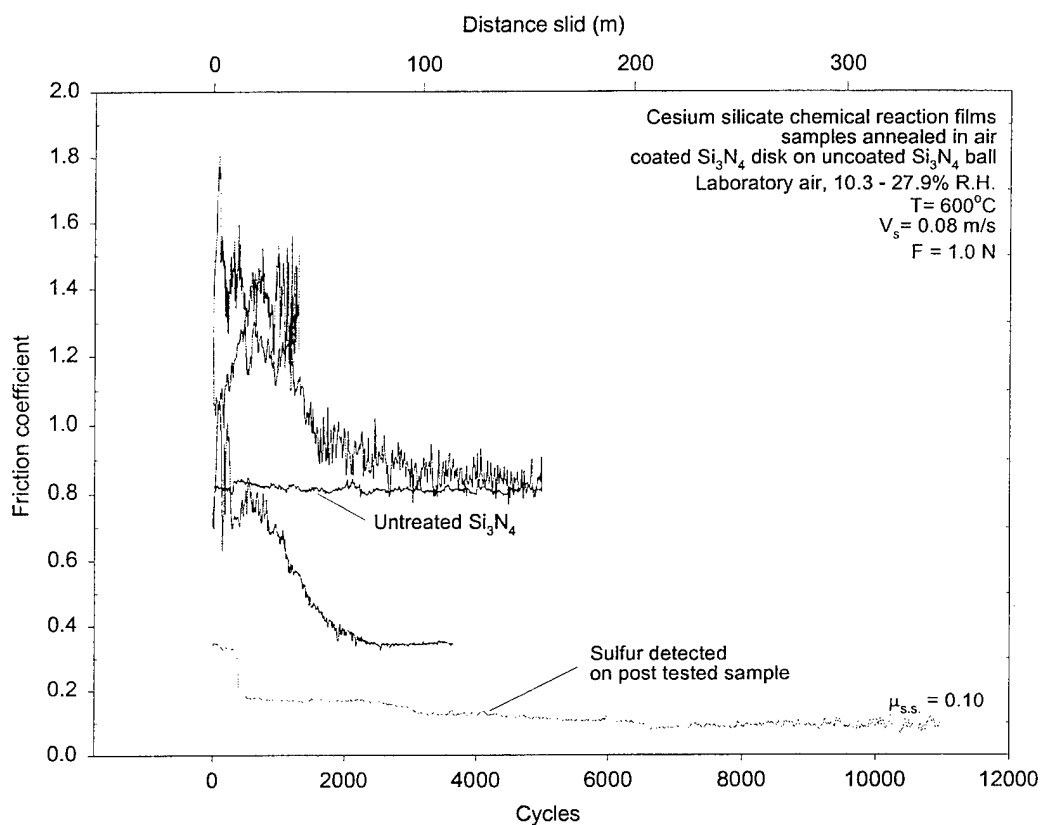
Figure 23. Friction Traces of CsOH Treated Samples Annealed in Air. Sample Contaminated with Sulfur Showed Dramatic Drop in Friction

To further investigate this, a 600°C experiment was performed on a CsOH treated sample which was purposely doped with elemental sulfur powder to see if this provided low friction. Friction obtained on this sample, however, was also relatively high ($\mu >$ 0.3). This implied that perhaps a gas phase reaction involving SO_2 or SO_3 was needed at the sample surface instead. Thus, the 800°C annealing process was modified by placing a small amount of elemental sulfur powder (2.4 mg) in a platinum cup and sealing the alumina crucible containing the powder and CsOH treated sample. A schematic showing the physical arrangement is illustrated in Figure 24. The idea was to convert the S_8 to SO_2 and SO_3 during the annealing step, promoting a gas phase oxidation-type reaction at the sample surface. Although a better approach would have been to anneal the sample in a well defined SO_3/O_2 gaseous environment at a well controlled SO_3 partial pressure, the setup would have been complex and time consuming. However, an approximate calculation of SO_3 partial pressure was made based on the volume of the crucible, assuming zero leakage, and the amount of sulfur used. It is estimated that p_{SO3} at 800°C was about 0.05 bar.

Upon cooling, it was apparent that all of the sulfur had volatilized as expected and the sample surface exhibited, what appeared to be a reaction front or halo that extended from the sample edge closest to the Pt cup toward the center. Under the optical microscope, this film appeared to consists of irregular shaped metallic gray globules, some of which exhibited interference colors. The friction coefficient obtained at 600°C on this sample was exceptionally encouraging ($\mu_{s.s.} = 0.10 \pm 0.008$) as shown in Figure 25. Moreover, low friction was obtained immediately upon starting the experiment, unlike all previous samples, including the bonded Cs_2WOS_3 coatings, which typically started at a higher initial friction. This implies that the lubricious film was already present on the surface prior to experiment startup. These results were confirmed with a longer duration replicate experiment run for 10,200 cycles, also shown in Figure 25, that gave a steady-state friction coefficient of 0.09. A third experiment conducted on a sample that was CsOH-treated at the author's laboratory exhibited even better performance yet. The initial friction of this sample was similar to that of the previous two ($\mu_i = 0.10$); however, a sudden drop in friction was noted after about 700 cycles of sliding, resulting in a steady- state value of 0.04 ± 0.004. This very low friction value is within the range obtained with ceramic-steel sliding couples lubricated with refined mineral oil at low temperatures [45]. Interestingly, the value is very close to the 0.03 value reported by Strong [31] on pulsed laser deposited Cs_2MoOS_3 thin films at 600°C.

These results indicate that sulfur plays an essential role in the formation of a lubricious film. The results also provide conclusive evidence that neither tungsten nor molybdenum are necessary for low friction at 600°C. In addition, the lower friction obtained on the third sample implies that a different lubricious film, perhaps of differing compositional makeup, was formed on this sample during sliding. This is supported by the surface analysis results presented in the next section.

43
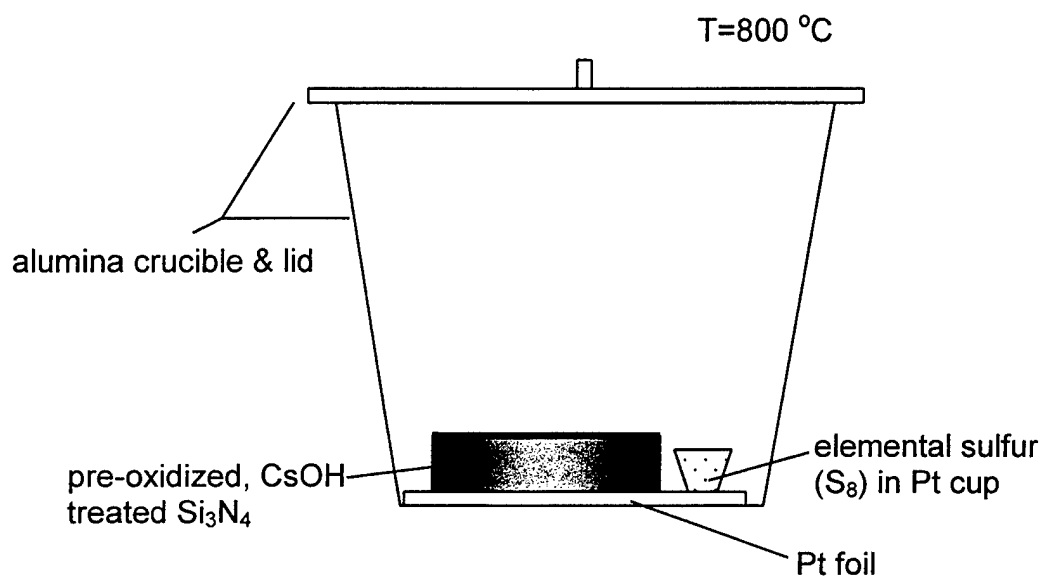
Figure 24. Schematic Showing Physical Arrangement of Modified Cesium Silicate
Chemical Reaction Film Annealing Procedure

Distance slid (m)

Cesium silicate chemical reaction films
coated Si_3N_4 disk on uncoated Si_3N_4 ball
laboratory air, 8.4 - 36.9 % R.H.
T= 600°C
V_S= 0.08 m/s
F = 1.0 N

Untreated Si_3N_4

Pre-oxidized Si_3N_4 (no CsOH)
anneal in air / SO_3 gaseous mixture

CsOH treated
anneal in air / SO_3 gaseous mixture

$\mu_{s.s.}$ = 0.09

$\mu_{s.s.}$ = 0.04 $\mu_{s.s.}$ = 0.10

Friction coefficient

Cycles
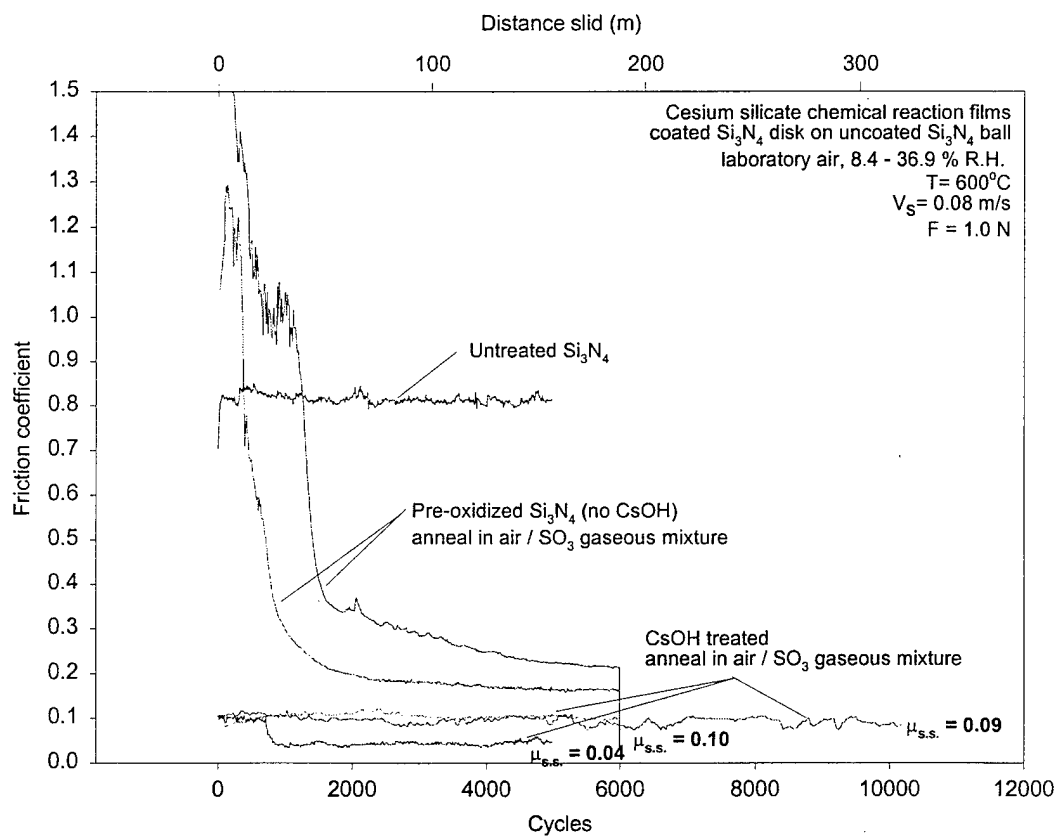
Figure 25. Effect of CsOH Treatment and Modified Annealing Procedure (i.e., Air + SO_3
Gas Mixture) on Friction Coefficient of Pre-Oxidized Si_3N_4

Friction experiments performed on pre-oxidized Si_3N_4 samples not treated with CsOH, but annealed in similar fashion as those discribed above (i.e., SO_2/SO_3 oxidizing environment) showed extremely high initial friction coefficients (above 1.0). Surprisingly, this was followed by relatively low steady friction ($\mu_{s.s.}$ = 0.17 to 0.21). Friction traces obtained on these are also portrayed in Figure 25. The low friction obtained at the end of these experiments suggest that a relatively soft lubricious film was also formed on these samples, despite the absence of cesium, though friction and wear was measurably higher than those containing cesium. SEM micrograph taken from inside the wear track of one sample (Figure 26) illustrates that small rolls, 5- to 20-μm long, were present on the surface. These were typically aligned perpendicular to the sliding direction. Similar rolls have been observed by others and it is believed that these are made of soft SiO_2 sheets that are rolled during sliding [35, 36, 39, 43]. There also appeared to be small voids or cracks (< 1.0 μm in size) throughout the surface.

Ball wear factors for all the cesium silicate films are shown in Figure 27. The lowest wear was obtained on CsOH treated samples annealed in the air gas mixtures containing sulfur (i.e., SO_2/SO_3). Wear factors were of the range of 4×10^{-9} to 1×10^{-8} $mm^3/N \cdot m$ for these samples. These values are comparable to those obtained on Si_3N_4/SiC whisker reinforced composites lubricated with 5W30 engine oil at room temperature [46] and Si_3N_4 under boundary liquid lubricated conditions [47]. Also, the wear rate of the sample contaminated with sulfur was comparable to that of the samples annealed with sulfur.

Figures 28 through 30 show wear scars and corresponding wear tracks generated on samples annealed in air and in air/SO_3 gas mixtures. The samples annealed in air exhibited considerable fine white wear debris attached to the balls, as shown in Figure 28a. This was not the case for the sample contaminated with sulfur, as shown in Figure 28b. The wear track was barely noticeable on this sample. The very low wear rate obtained on the samples annealed in the sulfur-rich oxidizing environment is evident from Figure 29b, which shows that the wear scar diameter was just slightly larger than the initial Hertzian contact diameter.

All of the samples annealed in the sulfur-rich environment displayed metallic gray globules or droplets which were transferred to the balls during sliding. This is shown in Figure 29. Some were clearly visible inside the wear scar as thin surface films (Figure 29a). In some areas, the globules appeared to coalesce into larger, needle-like structures, as depicted in Figure 29b. Some of the needle-like crystals were visible with the unaided eye and were present on the surface of the two samples that gave a friction coefficient of 0.10. The needles and globules were confirmed to be crystalline cesium sulfate by surface analysis.

Needles were not observed on the sample that gave ultralow friction (0.04) but very fine globules were on the surface (Figure 30). Unlike all previous ball wear scars, this sample had a noticeable film on the trailing edge of the wear scar and not nearly as much material buildup at the leading edge, suggesting liquid-like behaviour [48]. A narrow strip was also present toward the center of the wear track. SEM micrographs taken from

small voids and
cracks suggest
grain pullout

20 μm

sliding direction
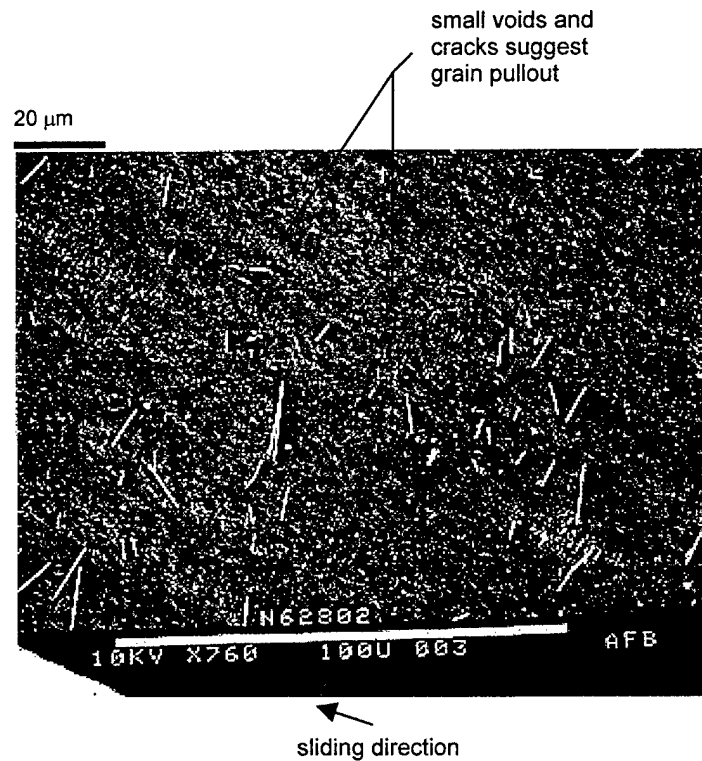
Figure 26. SEM of Wear Track of Pre-Oxidized Si_3N_4 Annealed in Sulfur-Rich Air After Sliding at 600°C

Note: Rod-like debris is believed to be made of soft SiO_2 sheets that have been rolled
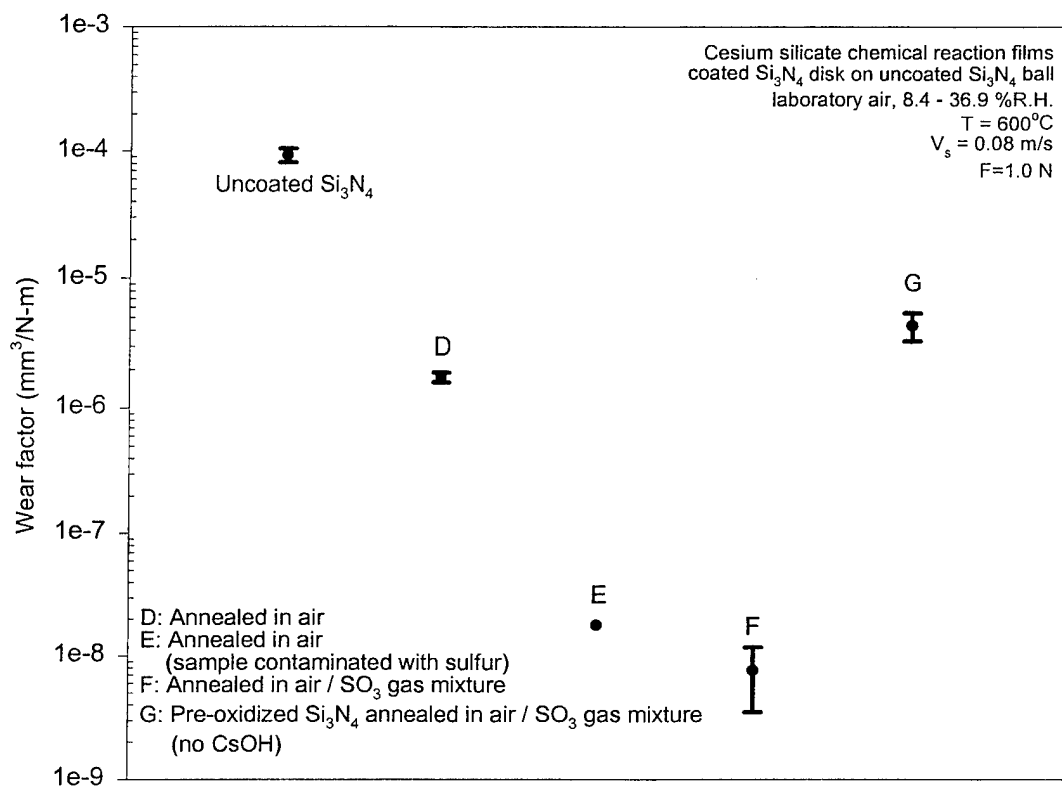
Figure 27. Mean Wear Factors and Standard Deviation of Balls Slid Against Cesium
Silicate Chemical Reaction Films at 600°C
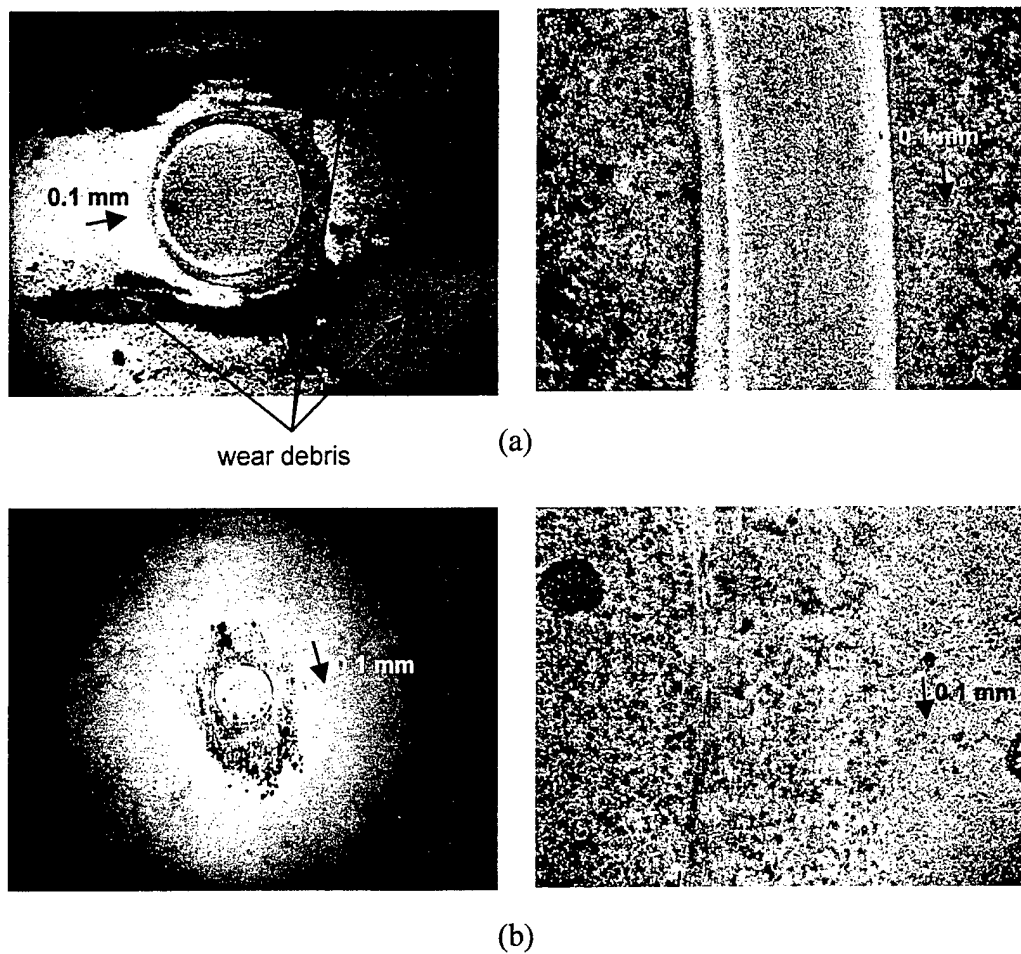
Figure 28. Optical Micrographs of Ball Wear Scars (Left) and Disk Wear Tracks (Right) of Cesium Silicate Chemical Reaction Film Samples Annealed in Air

Note: (a) $\mu_{s.s.}$ = 0.35 ± 0.01 (b) $\mu_{s.s.}$ = 0.10 ± 0.03, sulfur contaminant detected inside wear track of post tested sample. F = 1.0 N, V_s = 0.08 m/s, and T = 600°C. Arrow indicates relative ball sliding direction and scale.
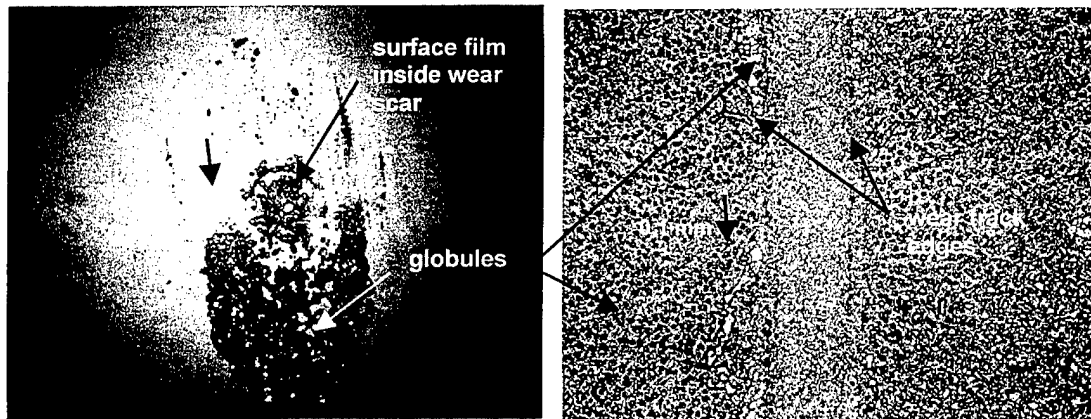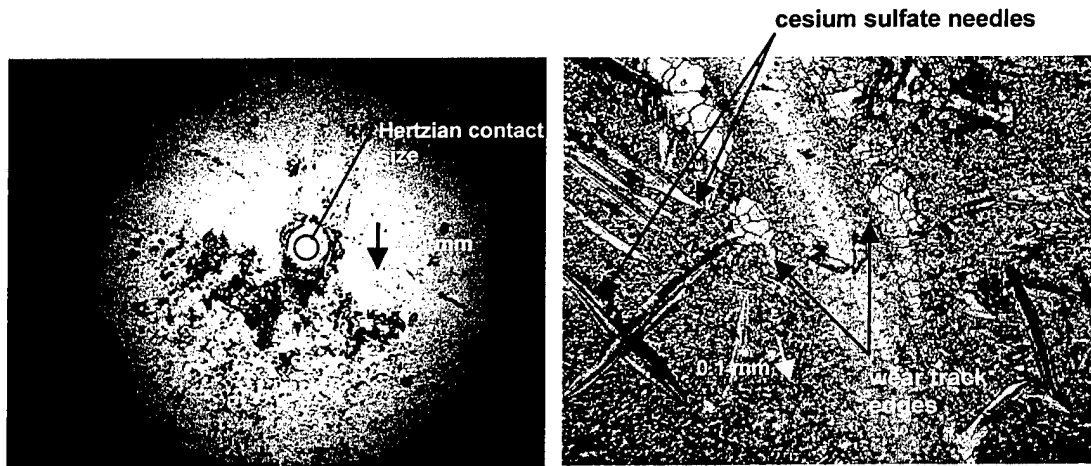
Figure 29. Optical Micrographs of Ball Wear Scars (Left) and Disk Wear Tracks (Right) of Cesium Silicate Chemical Reaction Films. Samples Annealed in Air/SO_3 Gas Mixture

Note: (a) $\mu_{s.s.}$ = 0.10, k = 9.0x10^{-9} mm^3/N·m (b) $\mu_{s.s.}$ = 0.09, k = 3.0x10^{-9} mm^3/N·m. All at F = 1.0 N, V$_s$ = 0.08 m/s, and T = 600°C. Small arrow indicates relative ball sliding direction and scale.
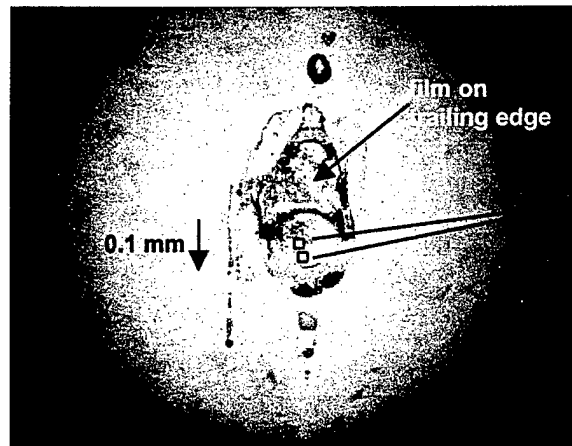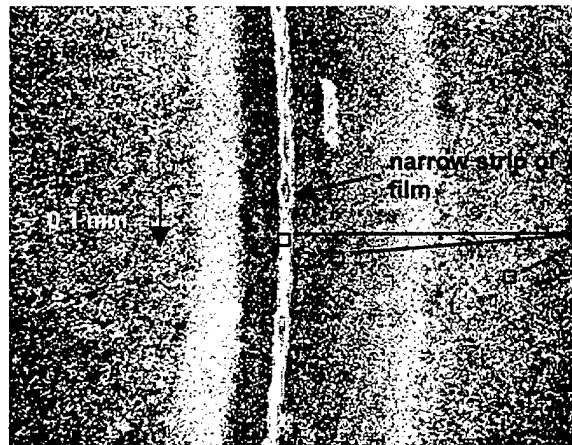
Figure 30. Optical Micrographs of Ball Wear Scar (Top) and Disk Wear Track (Bottom) of Cesium Silicate Chemical Reaction Film

Note: Sample annealed in air/SO₃ gas mixture. $\mu_{s.s.}$ = 0.04, k = 1.1x10⁻⁸ mm³/N·m at F = 1.0 N, V_s = 0.08 m/s, and T = 600°C. Arrow indicates relative ball sliding direction and scale.

these areas are depicted in Figures 31 and 32. In Figure 31, the top micrograph was taken within the top window (small box) shown in Figure 30 of the ball wear scar, while the bottom one was taken within the lower box. The surface consists of a smooth film or crust that exhibits considerable cracking. The cracking of the layer could be due to cristobalite (c-SiO_2), which undergoes a large volume change associated with its β to α phase transformation during cooling [108]. The presence of fibril-like morphologies, possibly silicate crystals, were also apparent. Unfortunately, the energy dispersive spectroscopy (EDS) detector on the SEM was not operational at the time, so chemical analysis of this these areas was not available.

Figure 32 shows that the narrow strip found near the center of the wear track consists of a film of globular-like morphology. Isolated globules were also present outside this film, but still inside the wear track (Figure 32c). Auger microprobe analysis and Raman and FTIR indicate that this film is primarily composed of Cs_2SO_4 and also contains magnesium and silicon. It is also apparent that the wear track surface, between the globules in Figure 32c, is remarkably smooth. There were shallow fissures throughout the surface, many of which appeared to emanate from underneath the globules. The surface outside the wear track was covered with a patchy film which also contained individual globules.
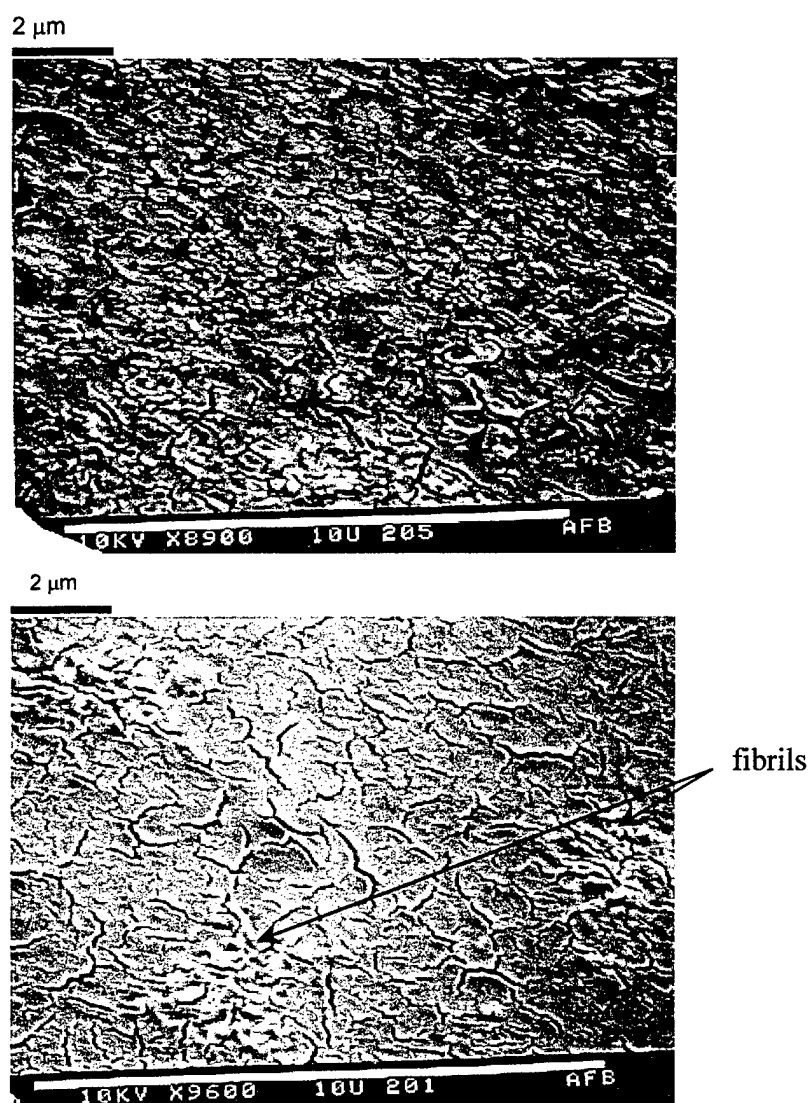
Figure 31. SEM of the Ball Wear Scar of CsOH Treated Sample Annealed in Air/SO$_3$
Gas Mixture ($\mu_{S.S.}$ = 0.04 at 600°C)
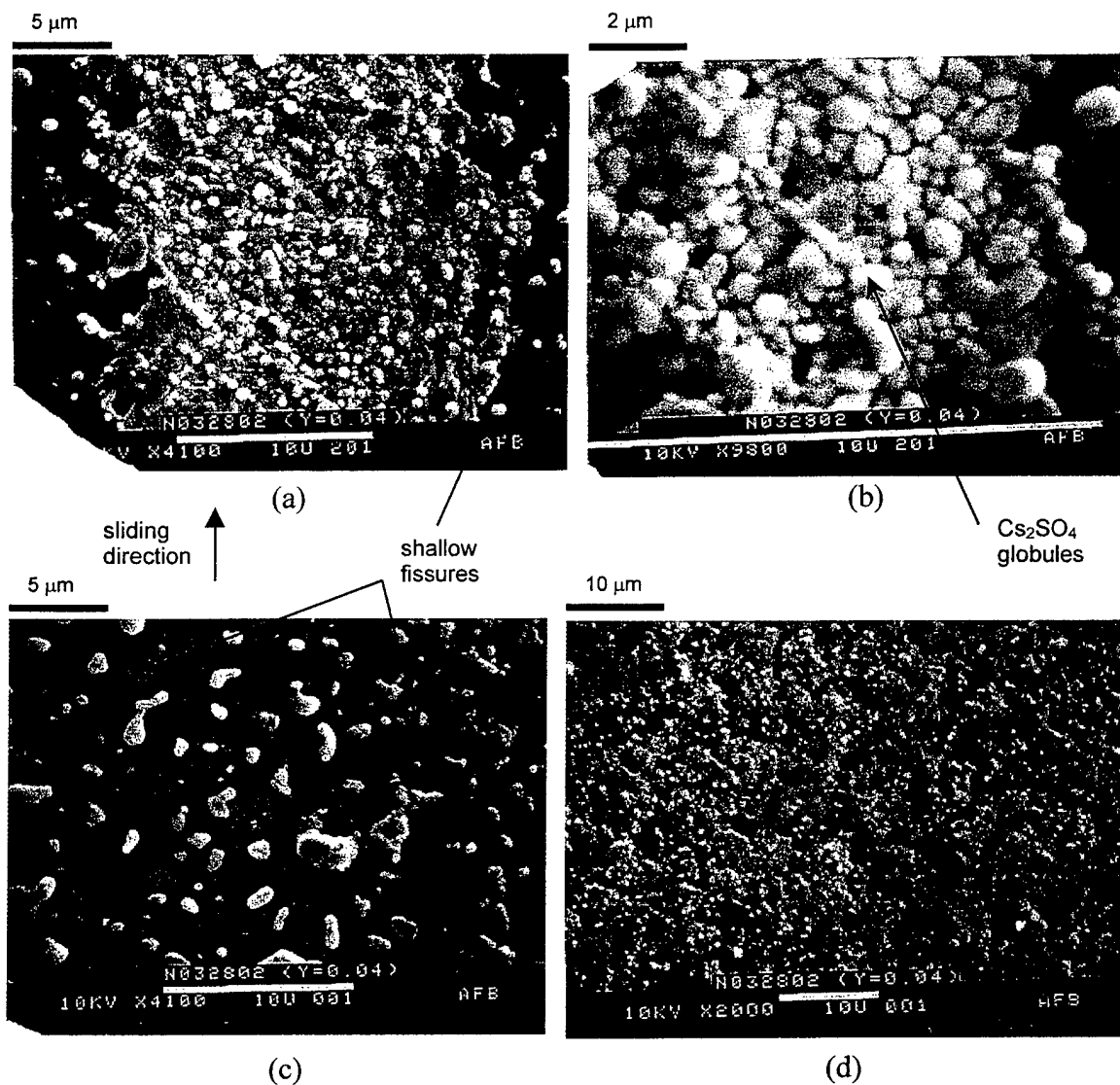
Figure 32. SEM Micrographs of Low Friction ($\mu_{s.s.}$ = 0.04) Chemical Reaction Film
Sample

Note: (a) and (b) narrow strip found near center of wear track consists globular-like
morphology. Surface analysis shows this film to be mostly Cs_2SO_4; (c) isolated globules
inside wear track but outside film; (d) patchy film outside wear track.

4. SURFACE ANALYSIS RESULTS

The surface analysis results obtained from inside the wear tracks of selected samples are reported in this section. Thirteen tested and 5 untested reference samples were analyzed. Tables 5 and 6 lists the samples analyzed and describe the experimental conditions and the frictional performance obtained on each sample. The surface chemistry was probed using Auger electron spectroscopy (AES) with depth profiling, micro-Fourier transform infrared spectroscopy (μ-FTIR), and laser Raman spectroscopy. AES results are reported first.

4.1 AES Results

Typical surface scan and depth profile results obtained on as-received Si_3N_4 and from inside the wear track of an uncoated Si_3N_4 sample tested at 600°C (sample 13) are shown in Figures 33 and 34. Except where noted, the depth profile sputter rate was ~80 Å/min. The as-received material shows high levels of surface carbon and a thin oxide layer < 10.0 nm thick. After sputtering the surface for 2 minutes the carbon due to surface contamination is removed and the carbon level remains at about 10 at.% thereafter. This suggests that carbon is present in bonded form. FTIR, presented later, indicates the presence of amorphous SiC. The results from inside the wear track of sample 13 show that carbon is significantly reduced and a thin oxide layer, approximately 20 nm thick, has formed. Underneath this layer, the material appears to be a mixture of Si_3N_4 and SiO_2 and/or silicon oxynitride. The magnesium Auger signal from the sintering aid also increased slightly on this sample as shown in Figure 33(b).

The approximate surface chemical composition of the Cs_2WOS_3 bonded coated samples and an untested aged sample (No. 16) are given in Table 7. There was a sodium-oxygen-rich layer on the surface of the aged reference sample. Unfortunately, AES was not conducted on a fresh as-coated sample for comparison. AES surface scans and depth profile results obtained from wear tracks are shown in Figures 35 and 36. Carbon was not included in the depth profile results. The low friction samples all exhibited relatively high surface oxygen and tungsten levels and low nitrogen and sulfur levels. The surface cesium level was about the same for all samples, while sodium and silicon levels varied. Magnesium from the Si_3N_4 sintering aid was essentially absent in all samples.

The depth profiles obtained on the samples that gave low friction (Figure 36a-c) indicate there is a thin tungsten-rich surface layer, several nm thick that could contain tungsten oxide and/or cesium tungstate. Beneath this layer, there is a thicker film, 80 to 110 nm thick, containing mostly silicon and oxygen and lesser amounts of tungsten, cesium, and sodium. The shape of the oxygen and nitrogen depth profiles are similar to mass diffusion profiles obtained from two semi-infinite sources bound at a common interface [49-50]. There is also an apparent accumulation of sodium and cesium near the oxide – Si_3N_4 interface. The pileup is believed to be an artifact due to electron-induced or

Table 5. Samples Selected for Surface Analysis[*]				
Sample Set No.	Coating System	Friction coefficient[**]	Experiment duration (cycles)	Analysis Technique
Sodium Silicate Bonded Cs_2WOS_3 Films				
1	bonded Cs_2WOS_3	0.17	20,258	AES
2	bonded Cs_2WOS_3	0.11	5,675	AES
3	bonded Cs_2WOS_3	0.15	4,800	AES, FTIR, Raman
4	bonded Cs_2WOS_3	1.23	6,000	AES, FTIR, Raman
Chemical Reaction Films				
5	CsOH treated	0.35	3,675	FTIR, Raman
6	CsOH treated	0.25	6,000	AES
7	CsOH treated	0.10	11,000	AES, FTIR, Raman
8	$CsOH + SO_3$ treated	0.10	6,000	AES, FTIR, Raman
9	$CsOH + SO_3$ treated	0.09	10,201	AES, FTIR, Raman
10	$CsOH + SO_3$ treated	0.04	5,000	AES, FTIR, Raman
11	Pre-oxid. + SO_3	0.17	6,000	AES, FTIR, Raman
Uncoated Si_3N_4				
12	uncoated Si_3N_4 (23°C)	0.57	5,000	FTIR, Raman
13	uncoated Si_3N_4 (600°C)	0.77	5,000	AES, FTIR, Raman

* Unless otherwise noted test conditions were: F = 1.0 N, V_s = 0.08 m/s, and T = 600°C.
** Average steady-state friction coefficient.

Table 6. Untested Reference Samples Selected for Surface Analysis		
Sample Set No.	Condition / Coating System	Analysis Technique
14	As-received NBD-200 Si_3N_4	AES, FTIR, Raman
15	As-received UBE Si_3N_4	AES, FTIR, Raman
16	Aged silicate bonded Cs_2WOS_3 coating on Si_3N_4	AES, FTIR, Raman
17	Pre-oxidized Si_3N_4	AES, FTIR, Raman
18	Pre-oxid. Si_3N_4 + CsOH + SO_3 treated	AES, FTIR, Raman
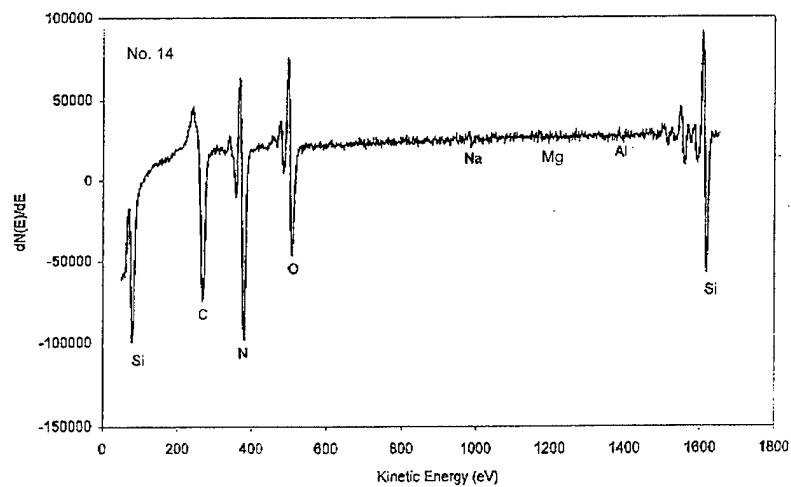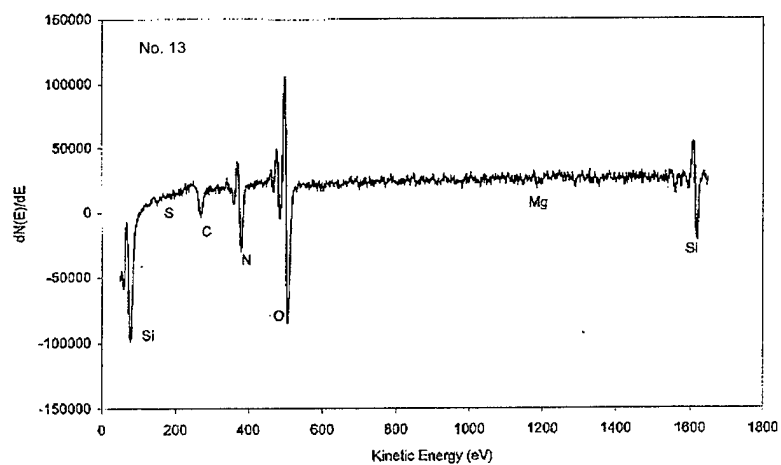
Figure 33. AES Surface Scans of (a) As-Received NBD-200 Si_3N_4 and (b) From Inside Wear Track of Uncoated Si_3N_4 Sample Tested at 600°C ($\mu = 0.77$)
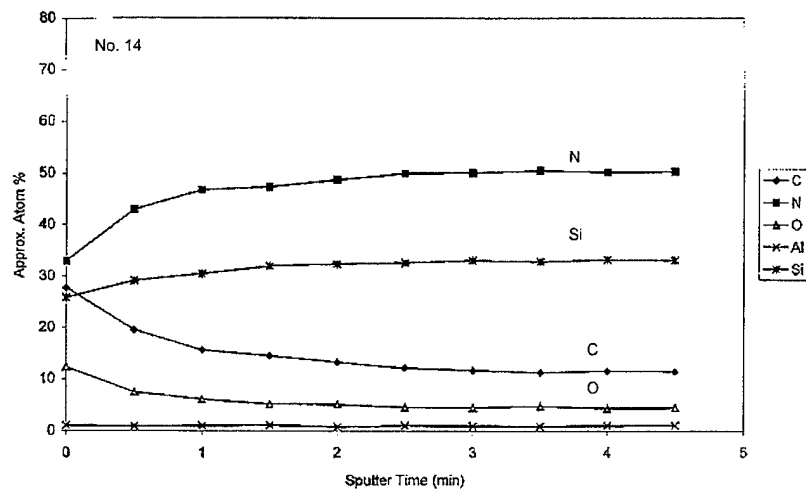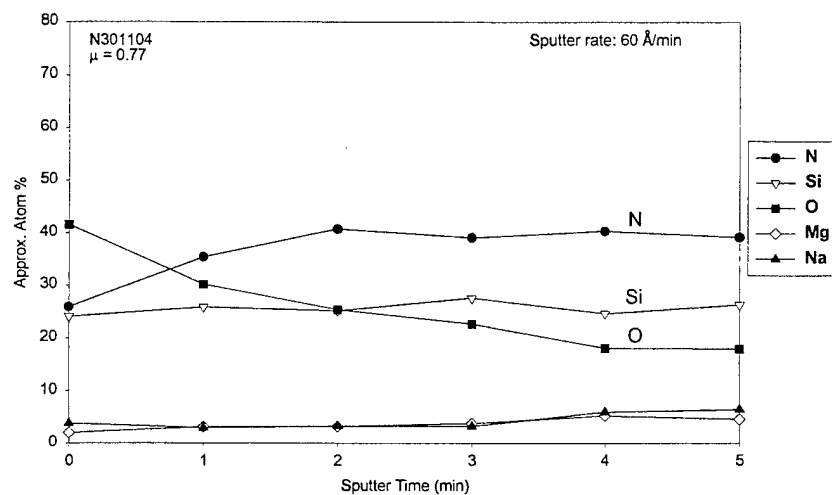
Figure 34. AES Depth Profiles of (a) As-Received NBD-200 Si₃N₄ and (b) From Inside
Wear Track of Uncoated Si₃N₄ Tested at 600°C (μ = 0.77)

Sample[**]	S	C	N	O	Cs	Na	Mg	W	Si
1 (0.17)	2.2 ± 0.7	3.3 ± 0.9	2.1 ± 0.3	56.1 ± 3.3	9.8 ± 1.9	3.0 ± 0.8	< 1.0	19.7 ± 1.9	3.8 ± 1.1
2 (0.11)	1.7 ± 0.8	5.2 ± 0.7	2.8 ± 1.3	45.0 ± 1.8	12.3 ± 1.2	8.7 ± 1.0	< 1.0	12.7 ± 1.5	11.6 ± 0.6
3 (0.15)	3.4 ± 0.1	20.4 ± 5.1	4.8 ± 1.9	43.8 ± 0.5	13.0 ± 0.8	8.4 ± 0.5	< 1.0	13.4 ± 1.0	5.1 ± 2.4
4 (1.23)	5.4 ± 2.8	13.4 ± 2.3	17.0 ± 3.1	31.2 ± 2.4	11.6 ± 0.4	6.7 ± 1.8	< 1.0	7.6 ± 1.3	13.8 ± 3.3
16	3.4 ± 0.8	8.8 ± 2.5	-	39.7 ± 1.3	2.0 ± 0.8	24.7 ± 5.1	-	10.9 ± 2.7	10.4 ± 2.0

Table 7. Approximate Atomic % Surface Composition of Cs_2WOS_3 Coated Sample Wear Track Films as Determined by AES[*]

*   Mean value and standard deviation given based on three surface scans.

**   Sample numbers from Tables 5 and 6. Average steady-state friction coefficient given in parenthesis.
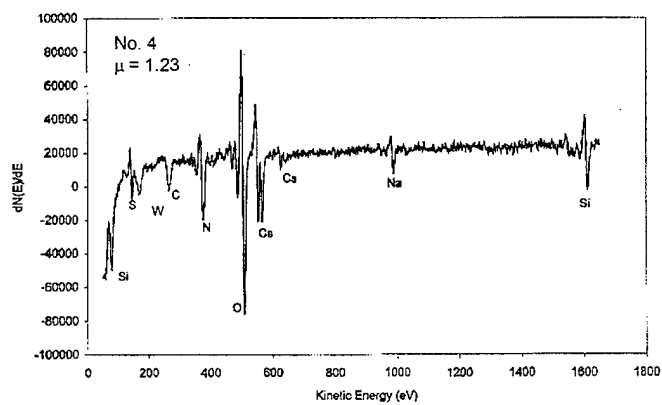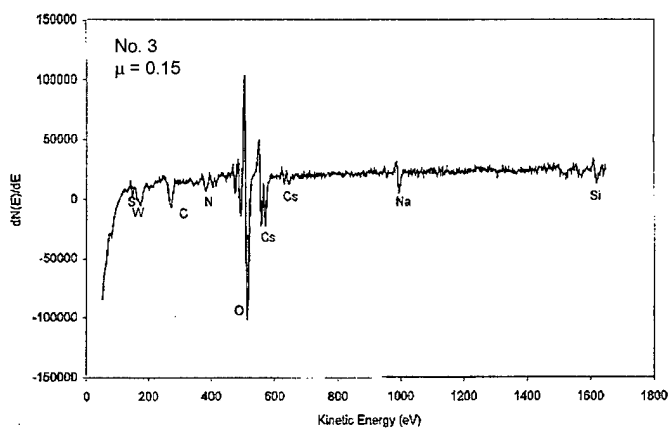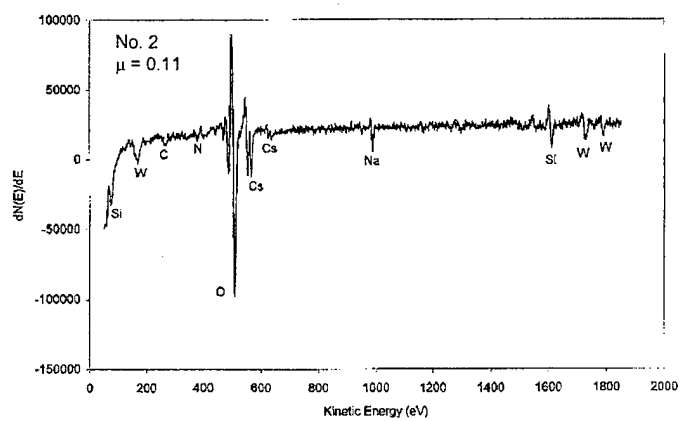
Figure 35. AES Surface Scans Obtained From Inside Wear Tracks of Cs_2WOS_3 Bonded Coated Samples
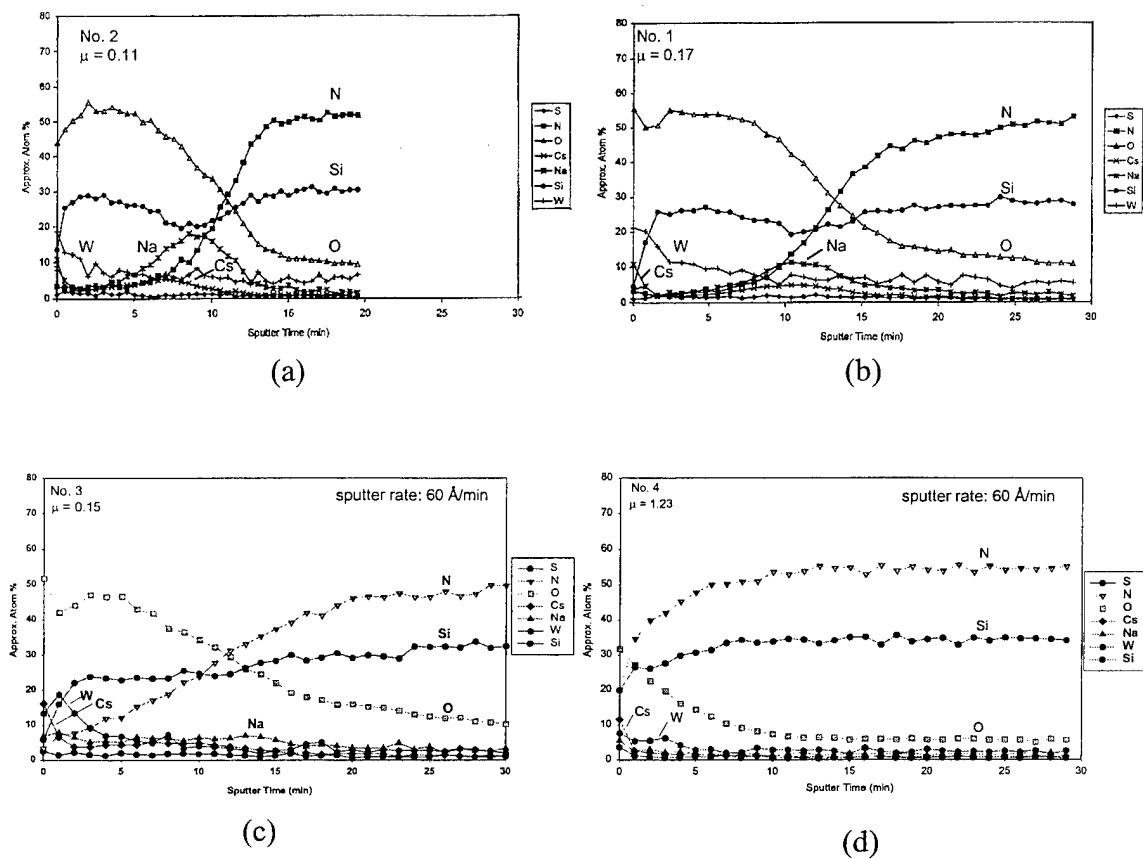
Figure 36. AES depth profiles obtained inside the wear tracks of Cs_2WOS_3 coated Si_3N_4 samples

Note: (a) – (c) Low friction samples exhibit 80 to 110-nm thick film containing mostly silicon and oxygen with tungsten, cesium, and sodium as secondary elements and (d) high-friction sample has thin oxide film, ~ 20 nm thick, with fewer secondary elements.

ion-induced migration caused by the sputtering process. It is known that alkali metal ions in glass are quite mobile and will tend to move under the influence of electric fields set up during ion-sputtering [51]. This was confirmed with a sample that was sputtered at a lower energy (1.0 versus 2.0 keV) which showed less pileup. The levels of sodium and cesium throughout the glassy surface layer may then be quite uniform, contrary to what is indicated by the depth profiles shown in Figures 36a-c. The greater pileup of sodium is probably attributed to its higher mobility due to its small ionic radius compared to cesium. The oxide film thickness of the sample that gave high friction was similar to that obtained on uncoated Si_3N_4 at 600°C (i.e., about 23 nm thick) and contained less oxygen and secondary elements. Also note the high surface nitrogen level on this sample indicating the underlying Si_3N_4 substrate is detected through the thin surface film.

The approximate surface chemical composition of the chemical reaction films are given in Table 8. Two untested reference samples were also analyzed; a pre-oxidized Si_3N_4 sample (No. 17) and a pre-oxidized + CsOH treated sample annealed in sulfur-rich air (No. 18). The surface compositions are fairly similar for the samples that gave low friction (samples 7, 8, 9, and 10). The results from sample 17 indicate that magnesium (sintering aid) diffuses out from the Si_3N_4 substrate during the static pre-oxidation given at 900°C. This is shown in Figure 37. Silicon and oxygen are also present suggesting that a magnesium silicate surface scale, about 110 nm thick, is formed during sample pre-oxidation. Figure 38 shows that the CsOH treatment and the 800°C-anneal in the sulfur-rich air environment causes growth of the pre-oxidation layer to about 170 nm with cesium being incorporated into the magnesium silicate film. Sulfur appears to remain mostly at the surface. The results confirm that the treatment and annealing process developed here are effective in producing a silicate film containing cesium.

The AES surface scan of sample 7 (Figure 39, top) shows that sulfur, which was introduced as a contaminant, is detected. Surface carbon levels are also high on this sample. Results shown for two of the CsOH + SO_3 treated samples indicate that the surface films contain oxides of cesium, magnesium, and silicon. The depth profiles shown in Figure 40 show that cesium and sulfur appear to concentrate at the near surface region, though cesium levels could be higher than that shown since sputtering may cause this particular element to migrate away from the analysis region, as previously described. Sample 10, which gave the lowest friction ($\mu = 0.04$), had slightly higher surface sulfur level than the other low friction samples. The ratio of surface cesium to sodium is also higher. The most obvious difference, however, is the higher cesium and slightly lower magnesium levels inside the film, below the surface, as depicted in the Figure 40 (bottom). This is graphically represented in Figure 41, which shows that the ratio of cesium to magnesium beneath the surface is significantly higher in sample 10.

The globular-like narrow strip that was observed on this sample was analyzed with Auger electron microprobe (electron beam diameter of about 0.5 μm). Results are shown in Figure 42. The sample was coated with a thin gold film to prevent charging. The results show that most areas are rich in sulfur, cesium, and oxygen while other areas also

Table 8. Approximate Atomic % Surface Composition of Chemical Reaction Wear Track Films as Determined by AES[*]								
Sample[**]	S	C	N	O	Cs	Na	Mg	Si
6 (0.25)	2.4 ± 0.2	16.3 ± 0.2	2.1 ± 0.2	49.9 ± 0.6	9.7 ± 0.4	3.3 ± 1.4	4.5 ± 0.3	11.7 ± 0.9
7 (0.10)	5.0 ± 0.2	53.7 ± 9.5	< 1.0	21.2 ± 5.5	3.8 ± 0.8	2.3 ± 0.5	5.5 ± 1.3	8.5 ± 1.2
8 (0.10)	3.3 ± 0.5	7.4 ± 1.5	< 1.0	46.9 ± 1.1	9.5 ± 1.1	4.5 ± 0.8	15.2 ± 1.1	10.9 ± 1.0
9 (0.09)	2.8 ± 0.6	7.1 ± 3.3	< 1.0	48.1 ± 2.5	7.8 ± 0.8	2.6 ± 0.4	17.4 ± 0.7	12.6 ± 0.9
10 (0.04)	7.6 ± 0.5	19.0 ± 4.4	1.3 ± 0.1	39.8 ± 3.1	9.1 ± 0.3	1.6 ± 0.3	11.8 ± 1.3	9.9 ± 1.0
11 (0.17)	0.6 ± 0.4	16.3 ± 2.0	5.9 ± 1.1	48.1 ± 0.7	< 0.5	< 1.0	2.6 ± 2.1	25.1 ± 1.2
17	0.8 ± 0.2	18.2 ± 3.5	< 1.0	45.1 ± 1.6	< 0.5	5.8 ± 0.4	15.2 ± 1.6	13.5 ± 0.8
18	7.0 ± 0.1	5.8 ± 0.6	4.0 ± 0.6	49.2 ± 0.5	7.2 ± 0.3	2.5 ± 0.5	11.9 ± 0.2	12.4 ± 0.7

[*]   Mean value and standard deviation given based on three surface scans.
[**] Sample numbers from Tables 5 and 6. Average steady-state friction coefficient given in parenthesis.
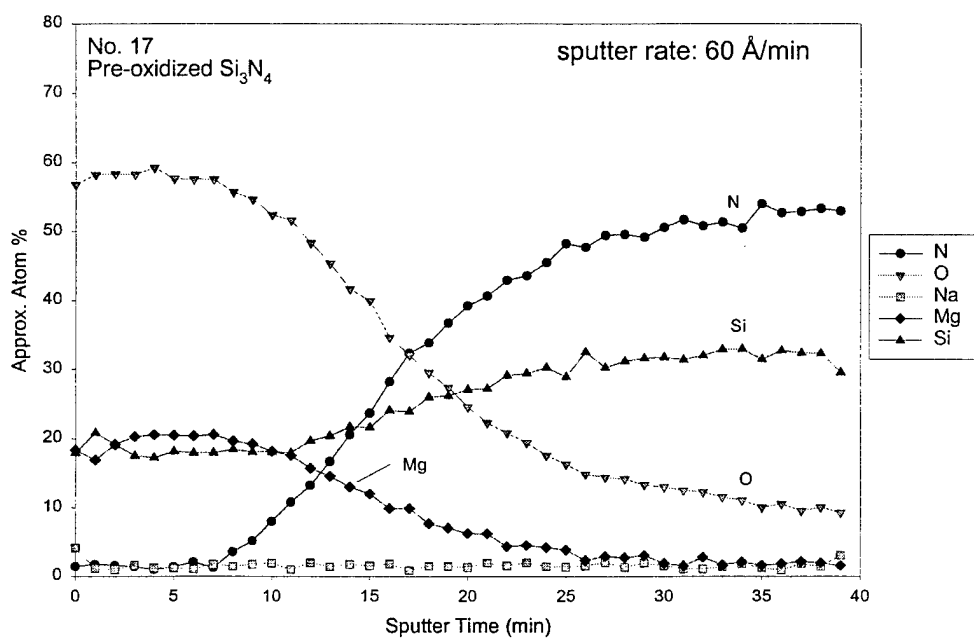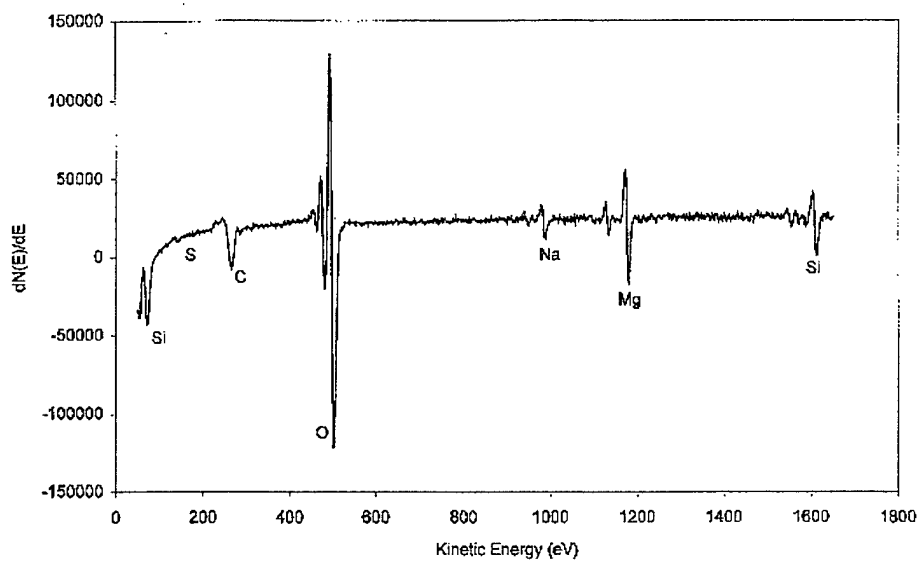
Figure 37. AES Surface Scan (Top) and Depth Profile (Bottom) of Pre-Oxidized Si_3N_4 Reference Sample Showing Formation of Magnesium Silicate Scale (~ 110 Nm Thick)
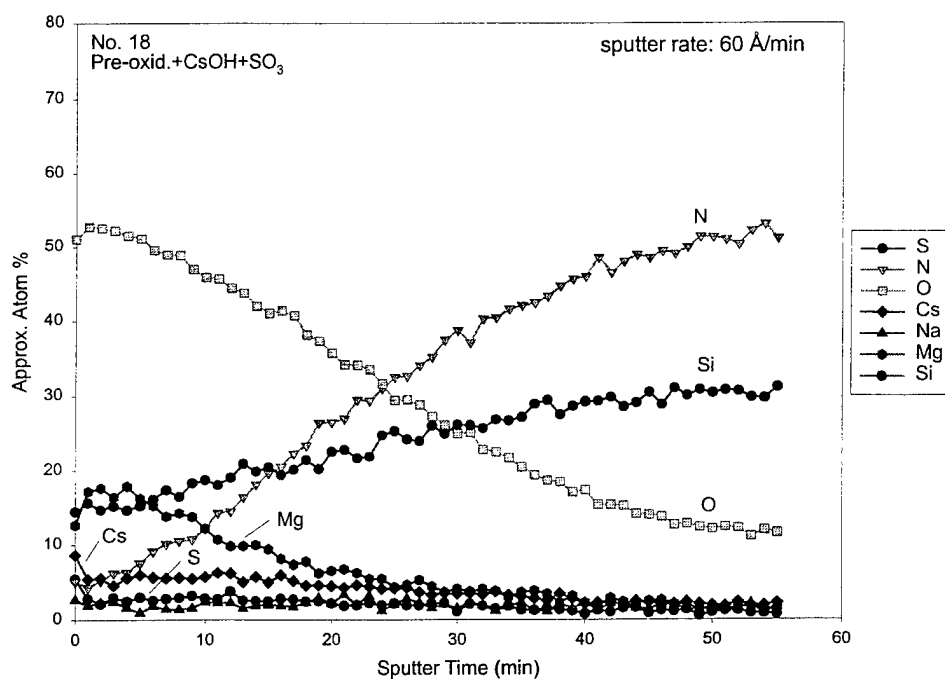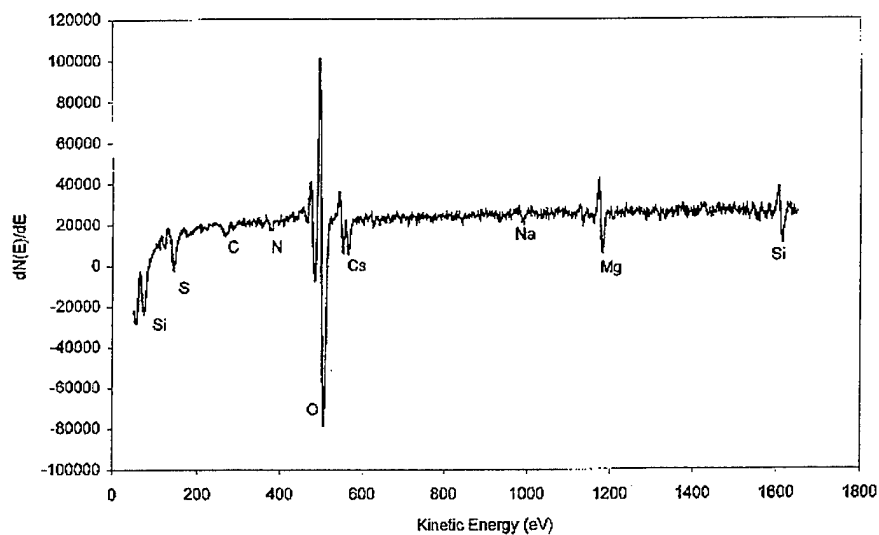
Figure 38. AES Surface Scan and Depth Profile of As-Deposited Chemical Reaction Film

Note: Cesium is incorporated into glassy magnesium silicate scale following CsOH treatment and 800°C anneal in sulfur-rich air. Sulfur remains mostly at the surface. As deposited film is ~170 nm thick.
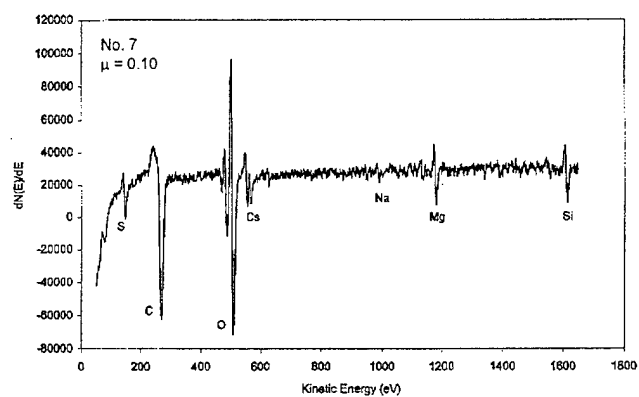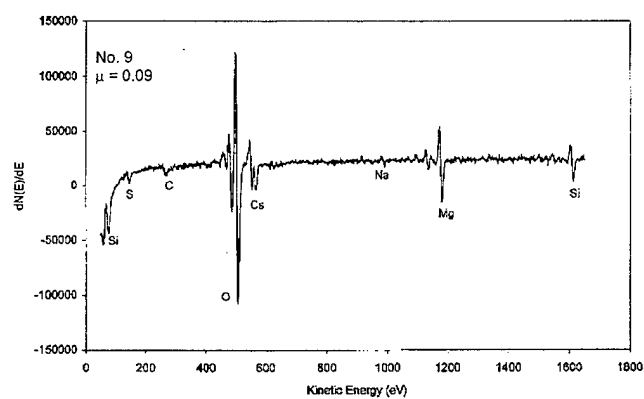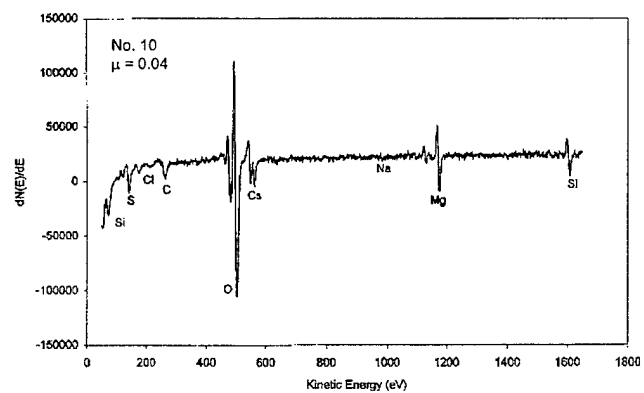
Figure 39. AES Surface Scans of Cesium Silicate Chemical Reaction Wear Track Films;
(a) CsOH Treated Sample Contaminated with Sulfur; (b) and (c) CsOH + SO₃ Treated
Samples
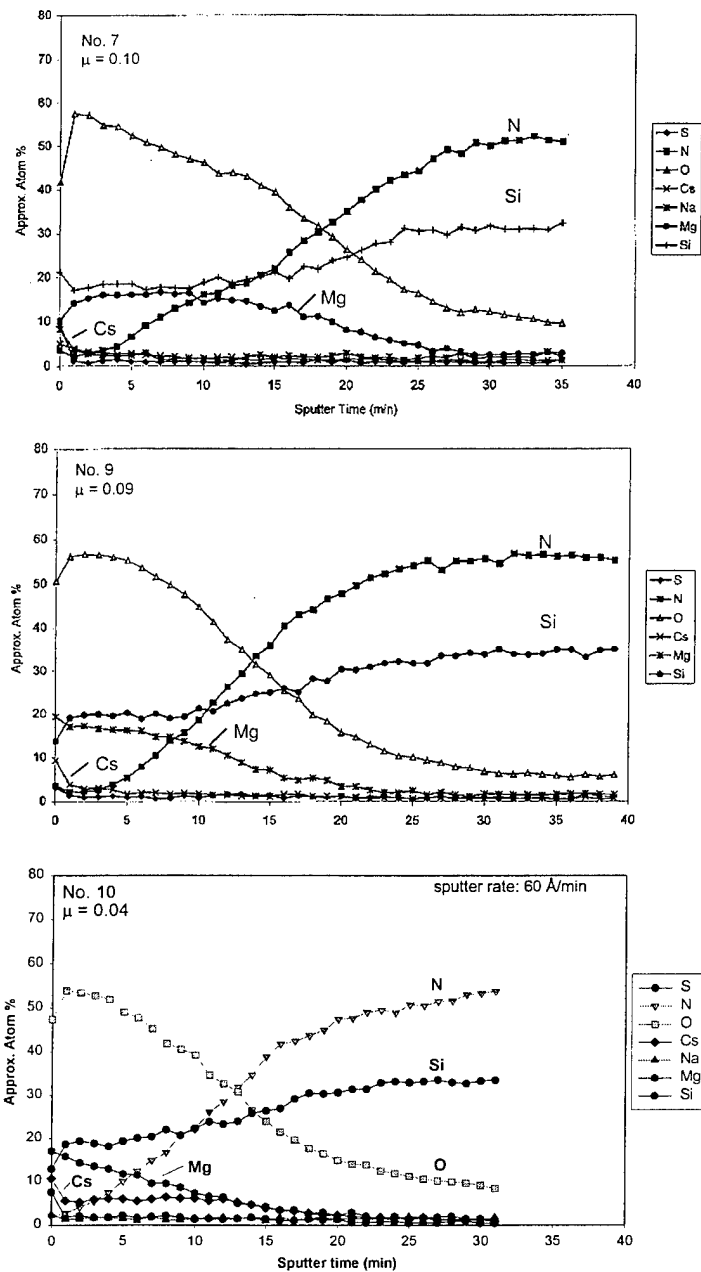
Figure 40. AES Depth Profiles Obtained From Inside the Wear Tracks of Low Friction
Chemical Reaction Film Samples

Note: Sample with lowest friction (No. 10) exhibits higher cesium levels inside glassy
film.
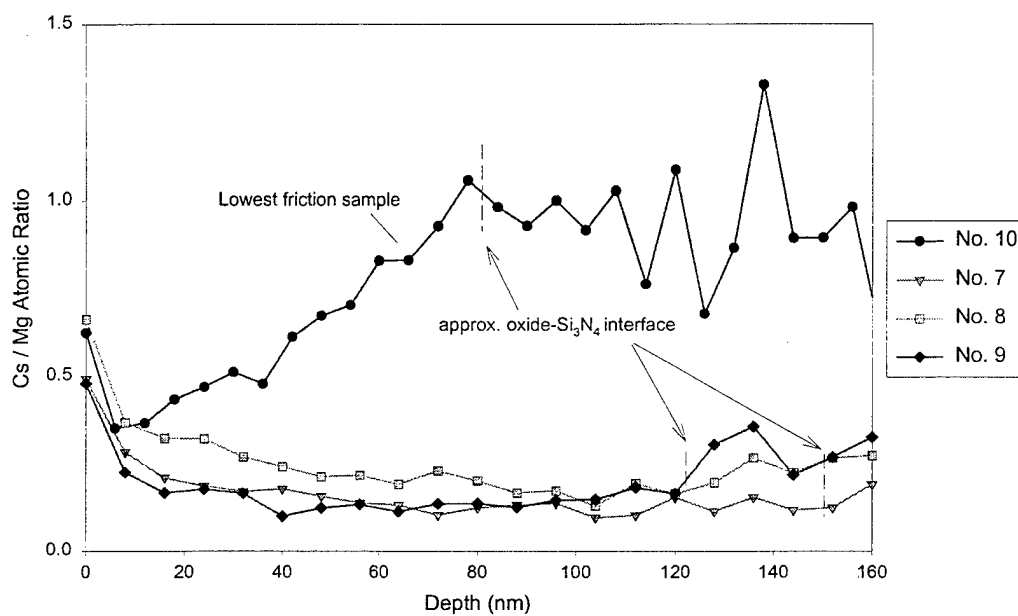
Figure 41. Ratio of Cesium to Magnesium as a Function of Depth of Low Friction
Chemical Reaction Films

Note: Sample with lowest friction ($\mu = 0.04$) shows highest cesium to magnesium atomic
ratio inside glassy surface film.
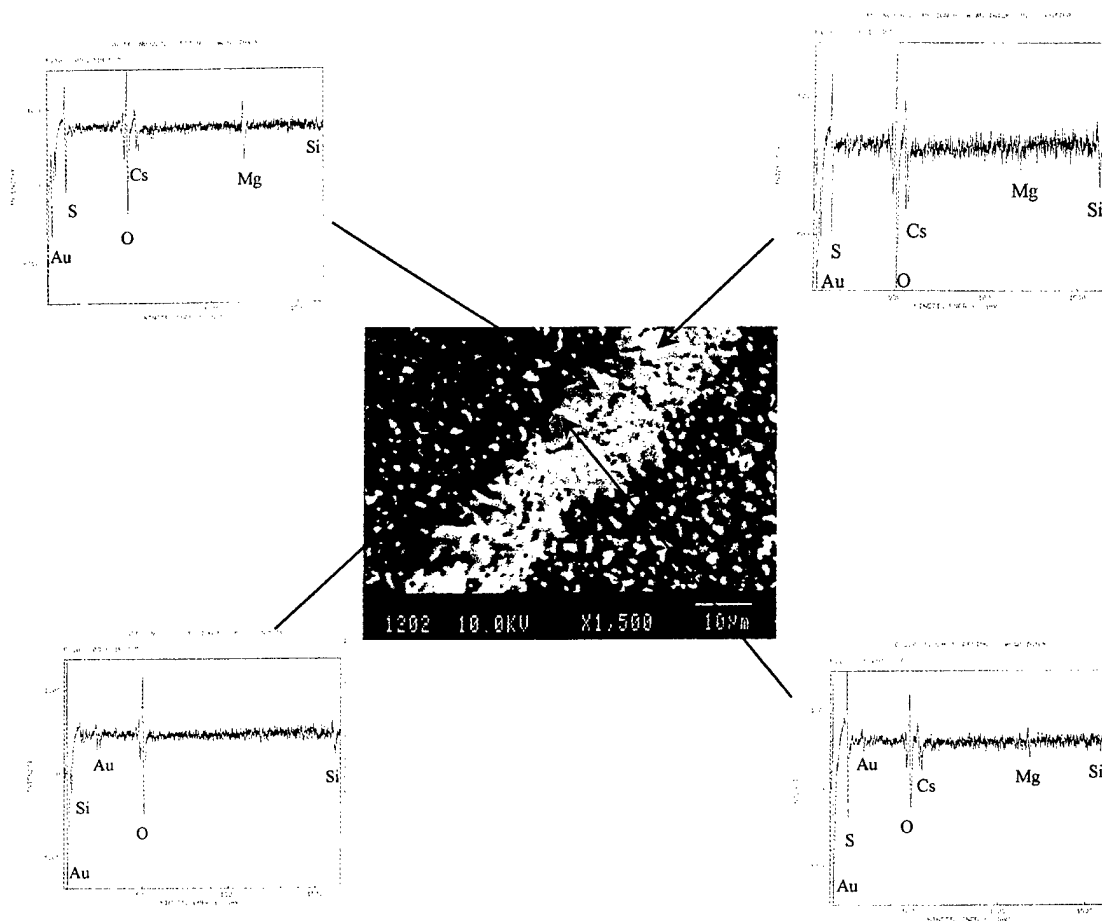
Figure 42. Auger Electron Microprobe Analysis of Narrow Strip Inside Wear Track of Low Friction Chemical Reaction Film Sample (μ = 0.04)

Note: Electron beam spot diameter is about 0.5 μm.

70

contain magnesium and silicon. The surface in between globules consists mainly of SiO_2. The shallow fissures observed to emmanate from underneath isolated globules were not analyzed.

Surprisingly, the depth profiles obtained on these samples are very similar to that obtained on the as-deposited film shown in Figure 38, suggesting that the film is maintained under dynamic conditions. The shape of the nitrogen, oxygen, and magnesium profiles implies a diffusional film growth mechanism, similar to the Cs_2WOS_3 bonded films. Film thicknesses inside the wear tracks ranged from 80 to 150 nm.

Figure 43 shows the depth profile results obtained from two samples that gave high friction. Sample 6 (Figure 43a) was treated with CsOH and annealed in air, while sample 11 (Figure 43b) was untreated but annealed in sulfur-rich air. The samples were pre-oxidized in the same fashion as all the previous ones. Both samples exhibited very high initial friction coefficients; 0.85 for sample 6 and 1.22 for sample 11. The relatively low friction coefficient obtained on these toward the end of the experiment indicates that a relatively soft film was formed after considerable sliding and wear. The profiles show that there is a layer containing mostly oxygen and silicon on both samples. The film is about 27 nm thick in sample 6 and 75 nm in sample 11. Cesium is detected in sample 6 at levels close to those obtained on the low friction samples, and sulfur was essentially absent in sample 11, despite the fact that this sample was annealed in a sulfur-rich air environment. The absence of magnesium in both samples indicates that the original pre-oxidized glassy layer has been worn away and was not replenished. These results indicate that both cesium and sulfur are necessary for low friction at 600°C.

As mentioned in Section 3, gray globules were observed on the surface of all of the samples that were treated with CsOH and annealed in a sulfur-rich oxidizing environment. Some of the globules appeared to coalesce into larger needle-like structures that were visible with the unaided eye. The AES surface scan obtained from one such needle is shown in Figure 44. The needle is composed predominantly of cesium, oxygen, and sulfur. This is consistent with cesium sulfate. As will be shown next, Raman and FTIR confirm this result.

4.2 Raman Results

The Raman spectra obtained from the untested (as-received) Si_3N_4 is shown in Figure 45. Surprisingly, the Raman spectrum obtained from the polished surface of the as-received NBD-200 material exhibits a sharp intense band at 520 cm^{-1} corresponding to crystalline cubic silicon [52-53]. The precise origin of the free silicon in the NBD-200 material is unknown. This band was essentially absent in the spectrum obtained from a polished HIP'ed β-Si_3N_4 material from a different vendor also shown in this figure. With the exception of the 520 cm^{-1} peak and the weak bands at 305, 800, 1140 cm^{-1}, and the shoulder at about 980 cm^{-1}, all other peaks in NBD-200 agree very well with crystalline β-Si_3N_4 [54-55]. The broad band centered around 800 cm^{-1} in NBD-200 is believed to be
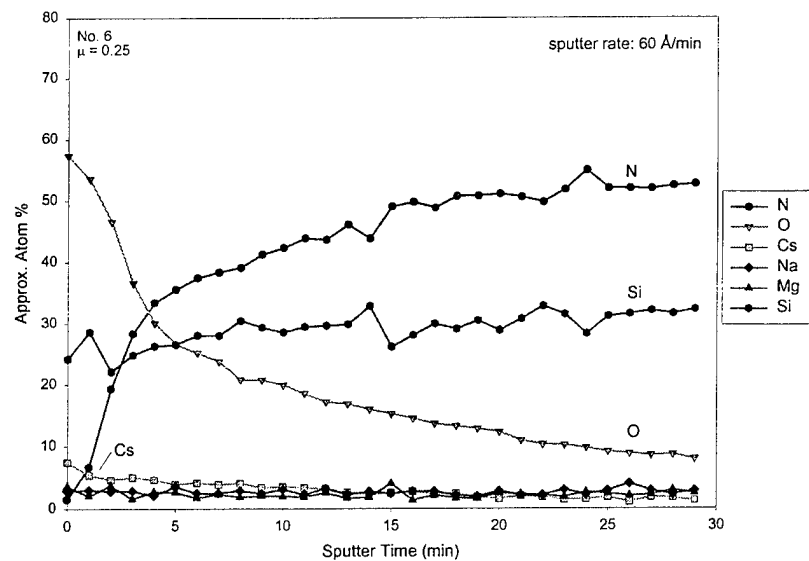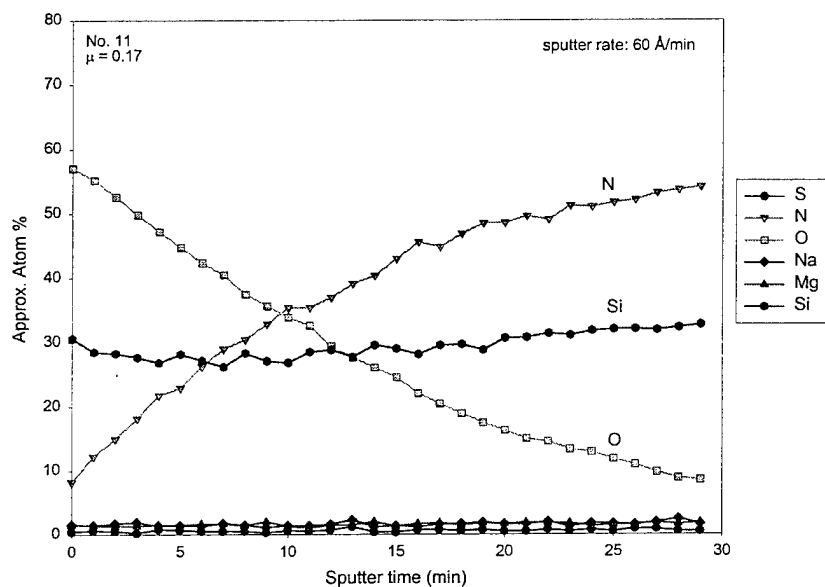
Figure 43. AES Depth Profiles Obtained From Inside Wear Tracks of High-Friction Chemical Reaction Films; (a) CsOH Treated, Annealed in Air; (b) Untreated, Annealed in Sulfur-Rich Air

Note: Both samples were pre-oxidized.
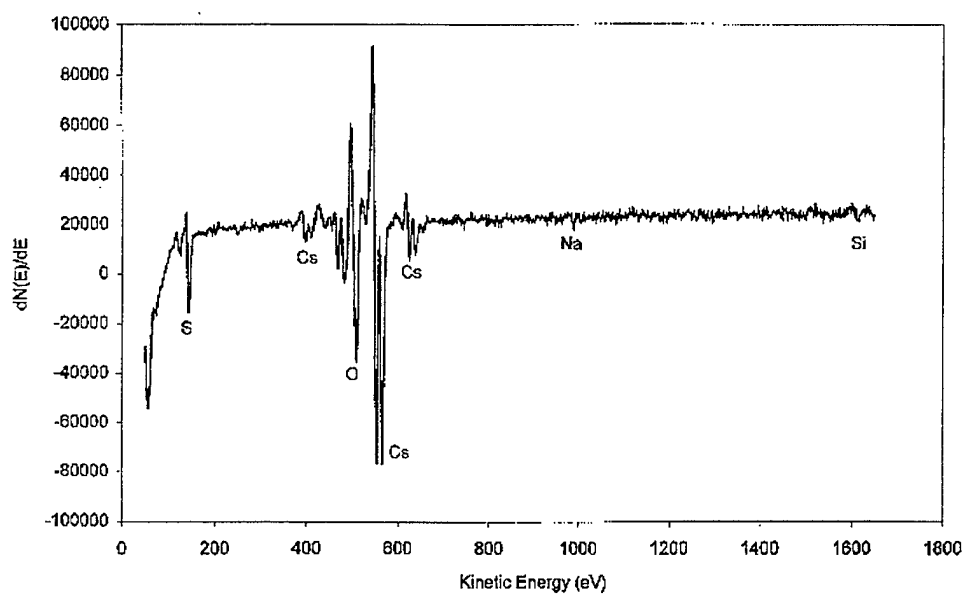
Figure 44. AES Spectrum of Needle-Like Structure Formed on CsOH + SO₃ Treated
Sample

Note: The composition is consistent with cesium sulfate.
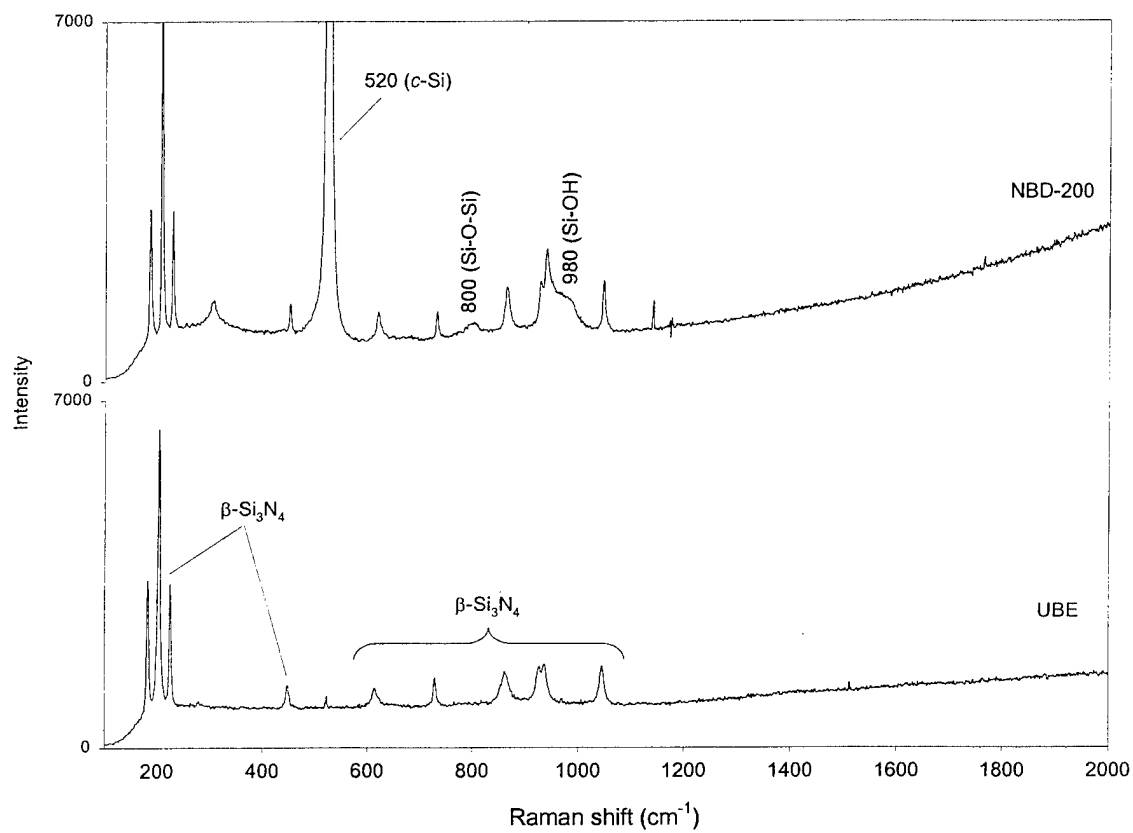
Figure 45. Raman Spectra of As-Received NBD-200 and UBE Si_3N_4 Materials

associated with the network structure of vitreous SiO_2 [56-57]. The shoulder at 980 cm^{-1} is tentatively assigned to Si-OH stretching [57]. The sharp peak at 1140 cm^{-1} is believed to be an atmospheric artifact while the 305 cm^{-1} peak could not be identified at this time.

The spectrum obtained on a tribochemical film present inside the wear track of uncoated Si_3N_4 tested at 23°C (sample 12) shows a measurable increase in fluorescence background (Figure 46). The wear track of this sample was previously shown in Section 3 (Figure 13a). This sample was tested at the upper end of the relative humidity encountered in the study (37 percent) and its friction coefficient was relatively low when compared to the mean value of the group ($\mu = 0.57$ vs. $\mu_m = 0.70$). In contrast, the spectrum recordedoutside the film, but also within the wear track does not exhibit an increase in fluorescence and is similar to the as-received material. A marked increase in fluorescence background was also noted in the sample tested at 600°C (No. 13) (not shown).

The Raman spectrum obtained on the untested aged-Cs_2WOS_3 bonded coated sample is shown in Figure 47. With the exception of the peaks at 521, 929, and 1069 cm^{-1}, the spectrum exhibits the primary bands associated with the [WOS_3] anion of the Cs_2WOS_3 molecule. These are in excellent agreement with values reported in the literature [58], and the assignment of these are given in the Appendix A. The high fluorescence background is believed to be attributed to the amorphous sodium silicate binder. The very weak band at 520 cm^{-1} is from the Si_3N_4 substrate (silicon). The sharp 1069 cm^{-1} band agrees well with the in-phase stretch of the CO_3 ion in sodium carbonate (Na_2CO_3) [59-60]. This is consistent with the AES results presented before that showed high surface sodium and oxygen levels on this sample and was confirmed with FTIR, which will be presented later. The source of the carbonate is believed to be from the reaction between the sodium silicate binder and atmospheric CO_2. The origin of the weak 929 cm^{-1} band is less clear, though tungstates exhibit their strongest Raman band in this region [61-63]. Sodium or cesium tungstate are viable compounds.

Figure 48 shows the Raman spectra for the low and high friction Cs_2WOS_3 samples. It appears the surface films in the center of the wear tracks are too thin to support Raman scattering and only the underlying Si_3N_4 is detected. AES showed these films to be around 80 and 20 nm in samples 3 and 4, respectively. Still, there appears to be an increase in relative intensity of the 940 cm^{-1} band of the Si_3N_4 substrate in the low friction sample. The analysis of the edges of the wear tracks, where the films were probably thicker, is shown in Figure 48b. The prominent doublet at about 1340 and 1580 cm^{-1} observed in both samples is characteristic of amorphous carbon with strain in the lattice [64]. The carbon is believed to originate from the decomposition of the sodium carbonate discovered on these samples. Decomposition of the [WOS_3] anion has also taken place in both samples as noted by the decrease in intensity of the 474 cm^{-1} band (W-S stretch) with respect to the 181 cm^{-1} band and the shoulder at 485 cm^{-1}. A decrease in the 250-263 cm^{-1} doublet (W-S deformation) and 867 cm^{-1} band (W-O stretch) are also apparent. This is consistent with the results obtained on heated Cs_2WOS_3 powder,
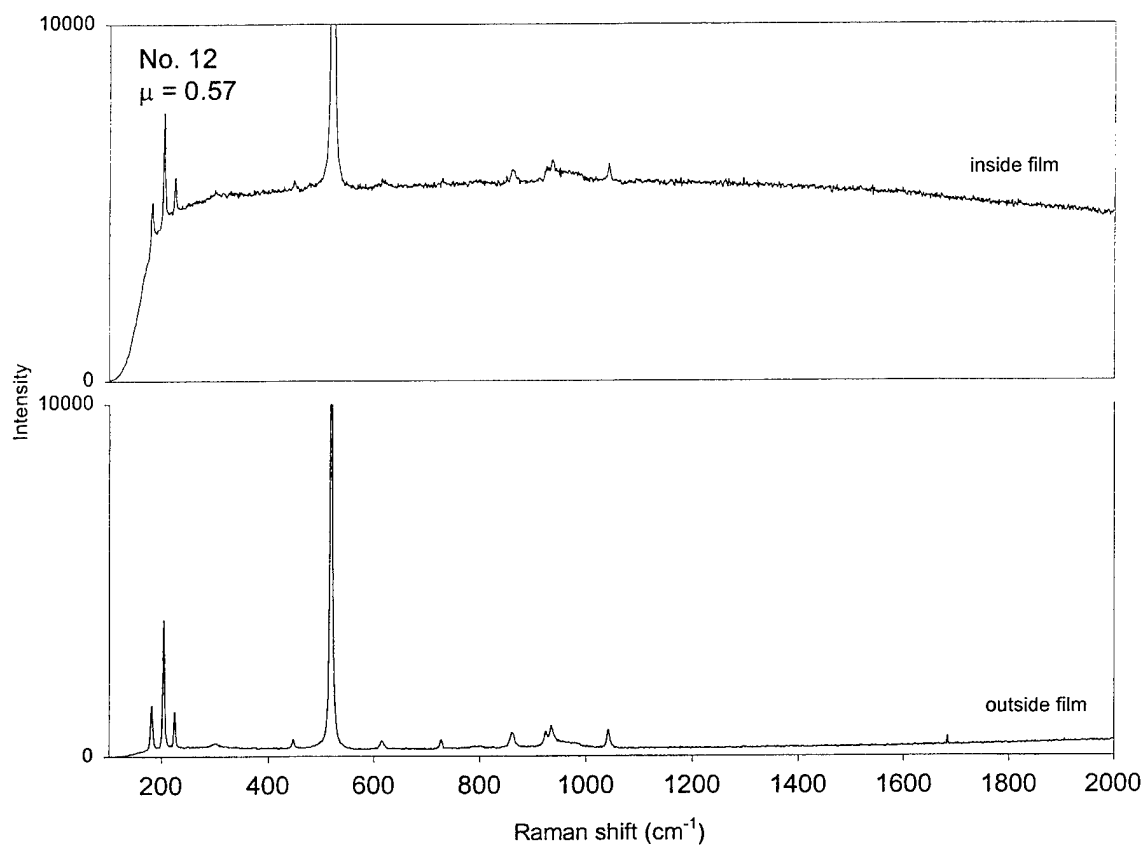
Figure 46. Raman Spectra of Uncoated Si_3N_4 Tested at 23°C and 37% (R.H) ($\mu = 0.57$)

Note: Spectrum obtained on tribochemical film inside wear track exhibits an increase in background fluorescence.
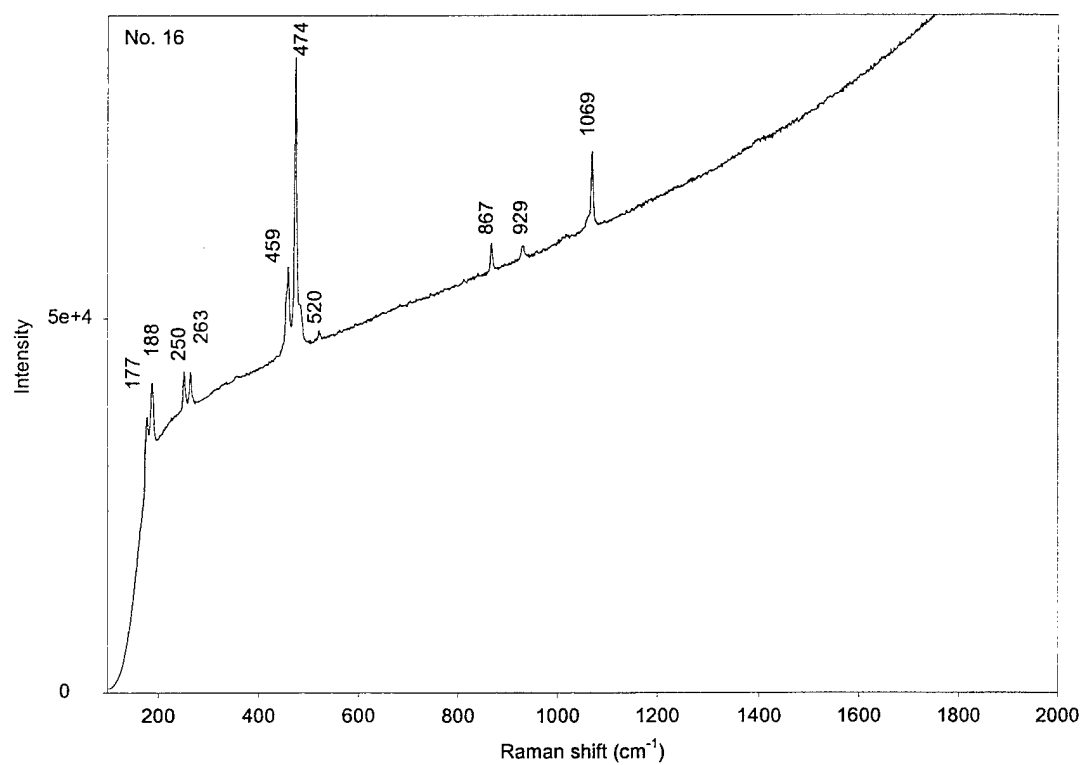
Figure 47. Raman Spectrum of Untested, Aged Sodium Silicate Bonded Cs_2WOS_3 Coating on Si_3N_4 Showing Presence of $[WOS_3]^{2-}$ Anion and Carbonate Contaminant
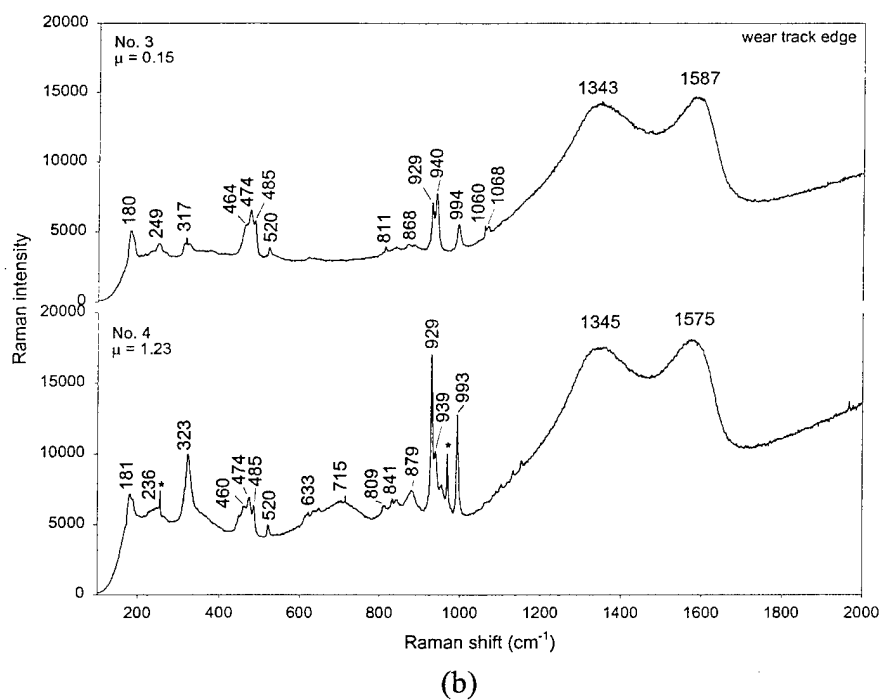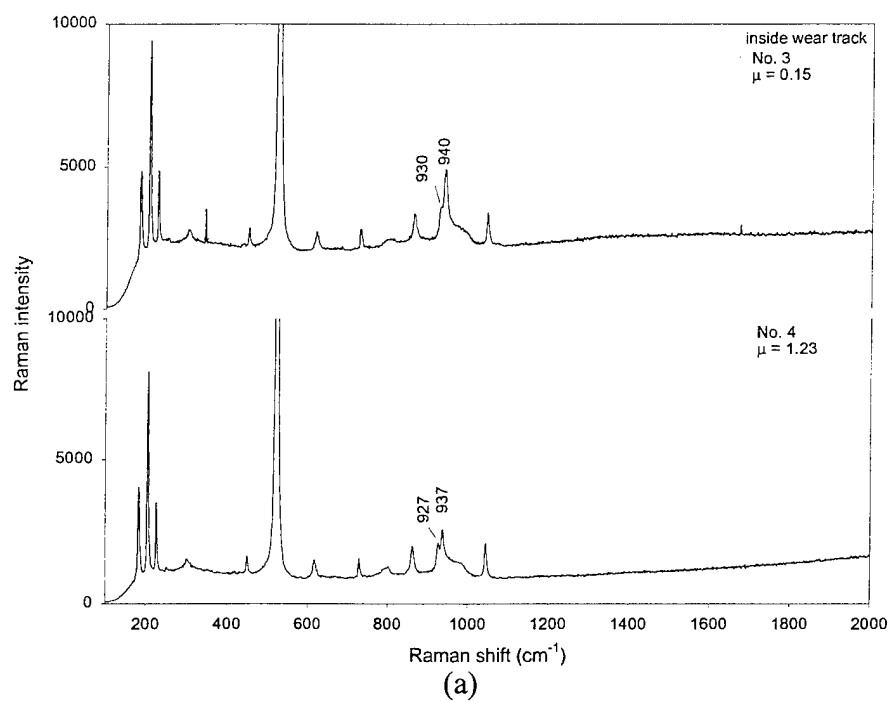
Figure 48. Raman Spectrum of Low and High Friction Cs_2WOS_3 Samples; (a) Inside Wear Track and (b) Wear Track Edge

78

presented in the Appendix B. The high friction sample exhibits a broad weak band centered around 715 cm^{-1}, which is absent in the low friction one. A similar feature was observed in a 600°C heated Cs$_2$WOS$_3$ powdered sample presented in the Appendix B. The 323, 929, and 993 cm^{-1} bands are also significantly more intense in this sample. Although these seem to originate from the Si$_3$N$_4$ substrate, the concurrent presence of weak bands in the 809 to 879 cm^{-1} range together with those at 323 and 929 cm^{-1} are indicative of tungstate [WO$_4$] type structures [65].

All of the Raman spectra from the chemical reaction film samples, including reference samples 17 and 18, exhibited substantial fluorescence background indicating that either the films are amorphous, the crystalline phases present are below the detection limit, or the film is Raman inactive. It is believed that the high fluorescence is primarily caused by the amorphous nature of the films. Typical spectra obtained on samples 8, 9, and 10 (low friction samples) are shown in Figure 49. Bands associated with the Si$_3$N$_4$ substrate were present in all the spectra. The AES results presented earlier indicated that the wear track films are enriched in silicon, oxygen, magnesium, and cesium. Sulfur waspresent mostly at the surface and was highest in sample 10. There were also needle-like structures outside the wear track on samples 8 and 9. These seem to originate from gray globules or deposits. Raman analysis of the gray deposits that accumulated near the edges of the wear track of samples 8 and 9 (shown previously in Figure 29) shows the presence of crystalline (orthorhombic) cesium sulfate [66]. This is shown in Figure 49 for sample 8. Crystalline sulfate was not detected by Raman inside the wear track of the samples, with the exception of sample 10, where a very weak band, noted at 969 cm^{-1}, suggests the presence of sulfate species, perhaps as microcrystallites. This analysis was performed on the narrow strip of film previously shown in Figures 30 and 32, confirming the Auger microprobe results. FTIR, which is more sensitive than Raman, also indicates the presence of sulfate.

4.3 FTIR Results

The FTIR spectra obtained from the as-received NBD-200 Si$_3$N$_4$ and the uncoated sample tested at 600°C are shown in Figure 50. In these spectra and those shown throughout, the peaks near 2350 cm^{-1} could be disregarded since these are due to absorption of CO$_2$ in the instrument. The spectrum of the as-received material shows a marked dissimilarity from that reported in the literature for crystalline β-Si$_3$N$_4$ [67] and hot-pressed β-Si$_3$N$_4$ with 4.7% MgO added [68]. In addition, the strong broad band near 719 cm^{-1} is located well below the Si-N and Si-O stretching bands of a-SiN$_x$ [69] and a-SiO$_2$ [70-72], respectively. Interestingly, the spectrum obtained from the UBE material (not shown) was similar. Since Raman confirmed both materials to be predominantly β-Si$_3$N$_4$, the inconsistency must lie in the different sampling depths between Raman and FTIR. Infrared penetration depths are less than 1.0 μm with the Ge-ATR device used here, whereas Raman typically samples at depths in the order of 5.0 μm. Thus, the FTIR spectra represent the near surface region of the samples, which apparently has undergone a structural or chemical change.
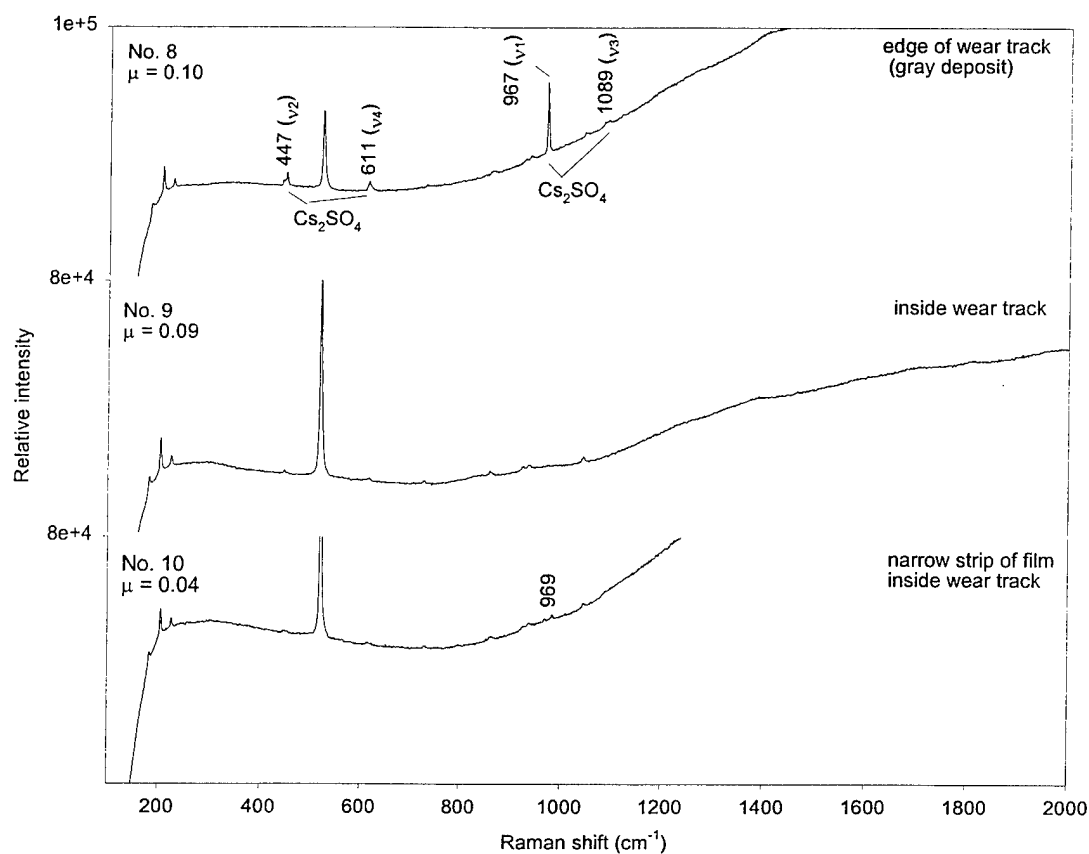
Figure 49. Raman Spectra of Low Friction Chemical Reaction Films Showing Presence of Cs_2SO_4 and Amorphous Films
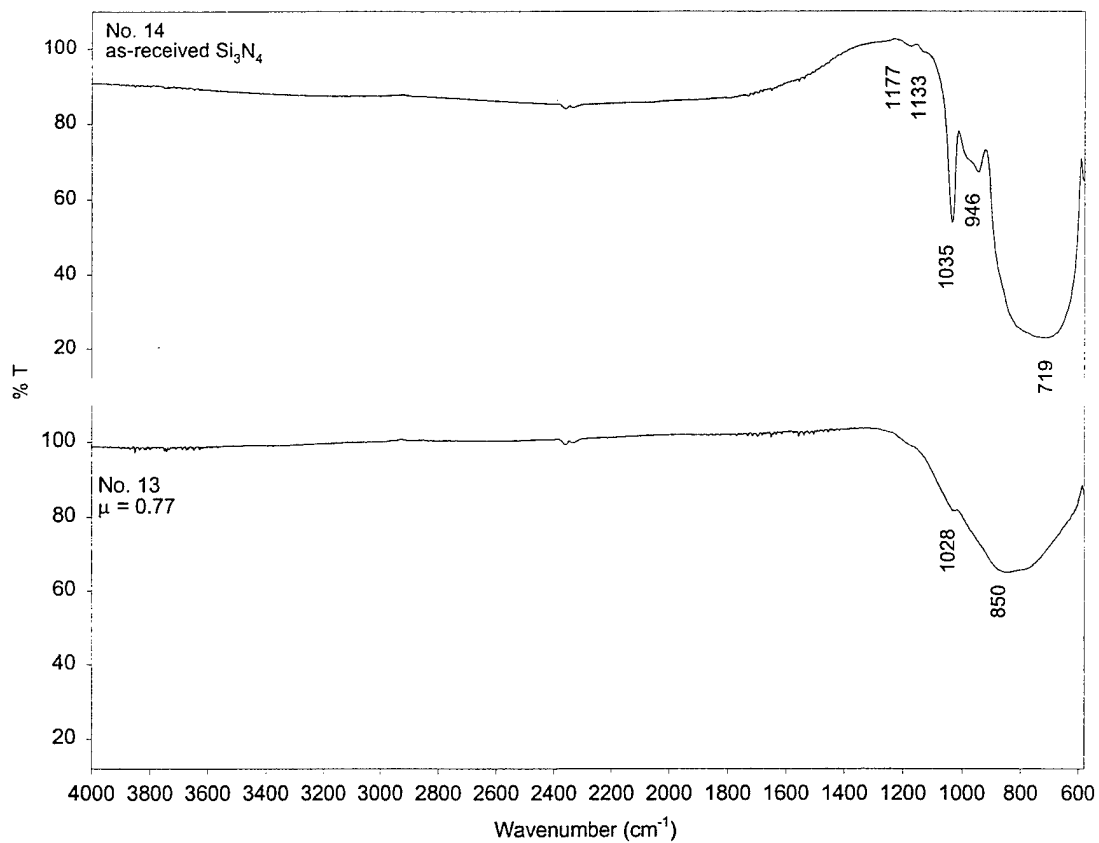
Figure 50. FTIR Spectra of As-Received NBD-200 Si_3N_4 and From Inside the Wear
Track of Uncoated Sample Tested at 600°C

An unambiguous assignment of the strong feature at 719 cm^{-1} could not be made at this time, though it agrees fairly well with the Si-C stretch in a-SiC [73]. This is partly supported by the AES results presented before, which showed that carbon levels remained steady and at a considerable level after removing carbon due to surface contamination by sputtering. It is possible that SiC was introduced during cutting or polishing of the samples. Another explanation could be that surface grinding and finishing has resulted in a localized deformation layer that is microstructurally different than the bulk. This has been observed by others in alumina and other ceramics, though not by FTIR [74, 75]. The sharp absorption band at 1035 cm^{-1} corresponds to the asymmetric stretch of bridging Si-O-Si bonds in vitreous SiO$_x$ structures [70-72] while the band at 946 cm^{-1} and the shoulder at about 980 cm^{-1} can be assigned to either the asymmetric Si-N-Si stretching mode of β-Si$_3$N$_4$ [67-68, 76] or to a nonbridging (NB) Si-O bond [77]. Si-OH stretching modes also absorb in this region [78].

The strong, broad peak at about 850 cm^{-1} observed in the 600°C tested sample is consistent with that of amorphous Si$_3$N$_4$ [69]. The broadness of this band is believed to be due to the coexistence of Si-O and Si-N structures, which have strong absorptions in the 800 to 1000 cm^{-1} region [69, 79-80]. This is consistent with the AES results that show an increase in oxygen levels. The FTIR spectra obtained from the sodium silicate bonded Cs$_2$WOS$_3$ coated samples are shown in Figure 51. The spectrum of the untested, aged sample agrees well with that of sodium carbonate [81] and is consistent with the Raman results. However, unlike Raman, the [WOS$_3$] anion is not detected here. This is due to the difference in penetration depth between Raman and FTIR. As noted previously, sodium silicates are known to react with atmospheric CO$_2$ in humid environments forming a thin weathered reaction layer in which carbonate salts can precipitate out [82-83]. It is unknown how quickly this layer developed nor whether it had an effect on friction results since a fresh, as-prepared sample was not analyzed.

The spectra from inside the wear tracks of samples 3 and 4 indicate that the Cs$_2$WOS$_3$ bonded coating has been worn away. There is a slight broadening and shift of the primary Si$_3$N$_4$ band, now centered at around 750 cm^{-1} in both samples. The broadening is probably caused by formation of Si-O structures and appears to be slightly greater in the low-friction sample (note 940 cm^{-1} band is less resolved). There is also a very weak shoulder at 1089 cm^{-1} in the high-friction sample which could be due to S-O stretching of sulfate that has formed from decomposed Cs$_2$WOS$_3$. This is supported by the AES results, which showed slightly higher sulfur inside the wear track of this sample.

The FTIR spectra of the pre-oxidized Si$_3$N$_4$ reference (sample 17) and the as-deposited chemical reaction film (CsOH treated sample annealed in sulfur-rich air, sample 18) are shown in Figure 52. The spectrum of the as-received substrate is also shown for comparison. Pre-oxidation causes a reduction in intensity of the major broad band at 719 cm^{-1} and apparently shifts the frequency to a slightly lower value. A shoulder also develops at about 1079 cm^{-1} and a relatively strong band appears at 995 cm^{-1}. The appearance of these bands causes the general region between 900 and 1100 cm^{-1} to broaden. As noted earlier, local Si-O vibrational modes absorb strongly in this spectral
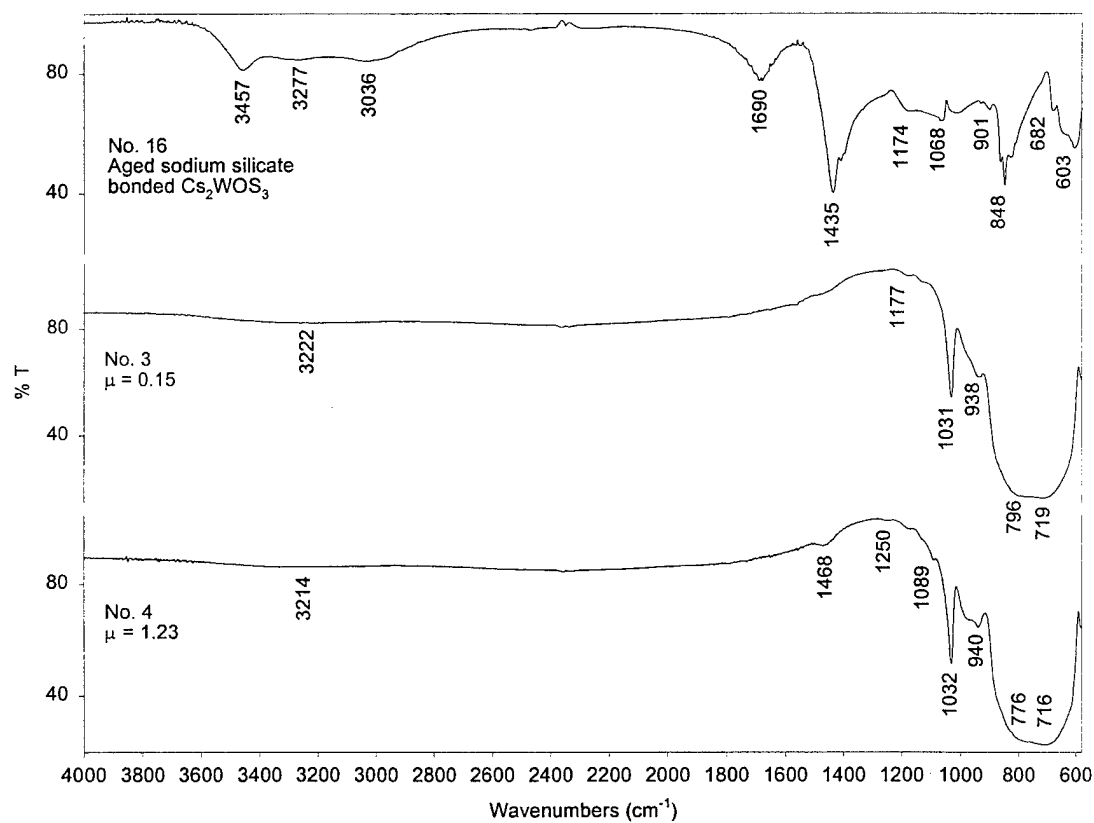
Figure 51. FTIR Spectra of Cs_2WOS_3 Bonded Coated Samples

Note: Untested, aged sodium silicate bonded Cs_2WOS_3 (top), from inside wear track of low friction (center) and high friction (bottom) samples. Spectrum of aged sample (top) is consistent with sodium carbonate.
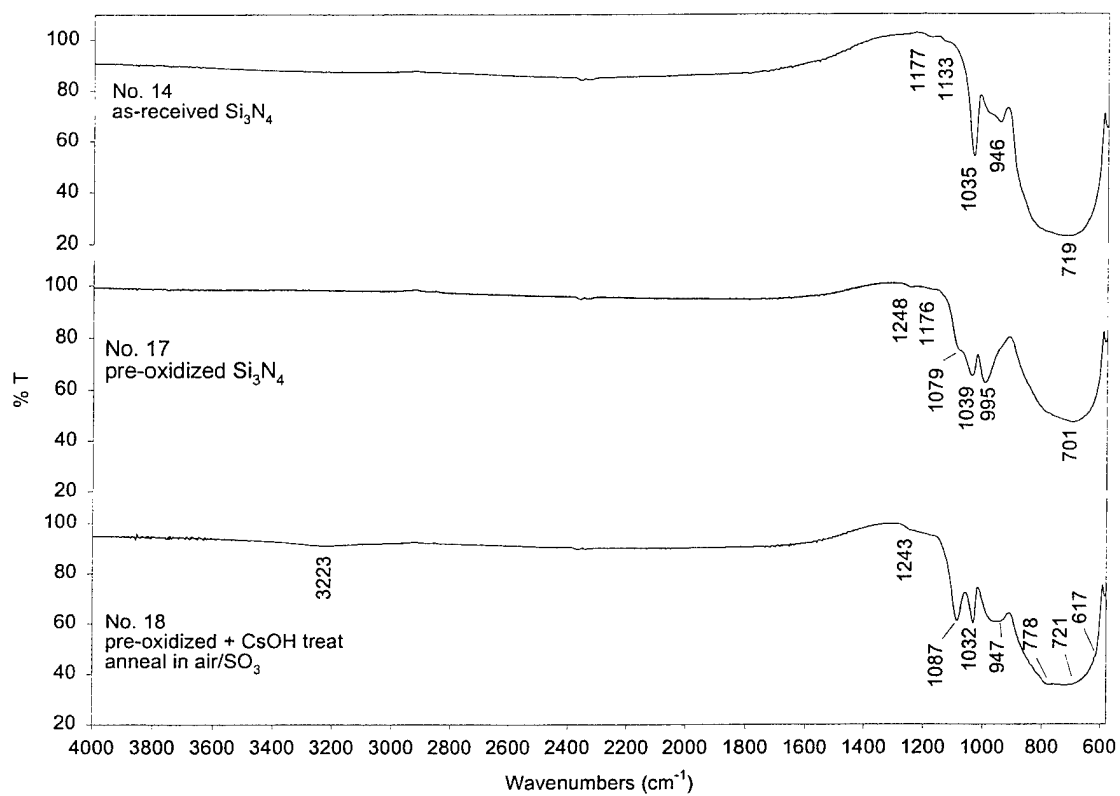
Figure 52. FTIR Spectra of As-Received Si₃N₄ (Top), Pre-Oxidized Si₃N₄ (Center), and As-Deposited Chemical Reaction Film (Bottom)

region. The 1079 cm^{-1} shoulder agrees very well with the bridging Si-O-Si asymmetric stretching mode in defect-free a-SiO$_2$ [70-72, 77]. This is supported by the appearance of the low intensity band at about 1248 cm^{-1}, which is coupled to this mode. The 995 cm^{-1} absorption band falls within the values reported for NB Si-O bonds in a-SiO$_2$ structures, such as in silicate and silicon oxynitride glasses [77, 79, 84].

The spectrum of the as-deposited film (sample 18) reveals an apparent increase in intensity of the 1079 cm^{-1} shoulder (Si-O-Si stretch), which appears to shift to 1087 cm^{-1}. In reality, the 1087 cm^{-1} band corresponds to the S-O asymmetric stretch (v_3 mode) of sulfate [SO$_4$]. This is supported by the presence of a very weak shoulder at 617 cm^{-1} (S-O bend, v_4) and by the Raman results from sample 8. The presence of the weak band at 1243 cm^{-1}, however, indicates the 1080 cm^{-1} mode of SiO$_2$ is obscured by the sulfate v_3 band. The broad 947 cm^{-1} band is assigned to NB Si-O bonds and/or Si-OH silanol groups. This is supported by the weak broad band centered about 3223 cm^{-1} attributed to hydrogen bonded SiO-H [85].

The spectra from inside the wear tracks of samples coated with chemical reaction films are shown in Figure 53. The intensity of the SiO-H stretching absorption band, ca. 3200 cm^{-1}, is highest in the sample with the lowest friction (sample 10). This band appears in all of the samples that gave low friction, including sample 8 (not shown) and is nearly absent in those that gave high friction. The spectrum of sample 10 also resembles that of the as-deposited film, except for the stronger SiO-H stretching band and the appearance of a shoulder at 984 cm^{-1}, which is assigned to Si-OH stretch. Sulfate is also detected as noted by the strong 1089 cm^{-1} band and weak shoulder at 616 cm^{-1}. The absence of bands in the 1175 to 1230 cm^{-1} region (defect-free a-SiO$_2$) and the relatively strong band at 939 cm^{-1} suggests Si-O type structures of predominantly NB character. In contrast, the 940 cm^{-1} band (NB Si-O) is notably absent in sample 5 (highest friction). Interestingly, the spectra from samples 9 ($\mu = 0.09$) and 11 ($\mu = 0.17$) show similar trends with the only exception that the low-friction sample exhibits a SiO-H stretching absorption band at 3225 cm^{-1}. It is important to note again that the initial friction coefficient of samples 5 and 11 was very high (~ 0.80 and 1.22, respectively), whereas that of samples 8, 9, and 10 was about 0.10. The results suggest that the presence of NB Si-O or Si-OH bonds are necessary for low friction.

Finally, the presence of crystalline cesium sulfate outside the wear tracks of samples 8, 9, and 10 was confirmed by FTIR. Figure 54 shows the spectrum obtained from a needle-like structure at the edge of the wear track of sample 9. The two primary absorption bands, characteristic of orthorhombic Cs$_2$SO$_4$, are evident.
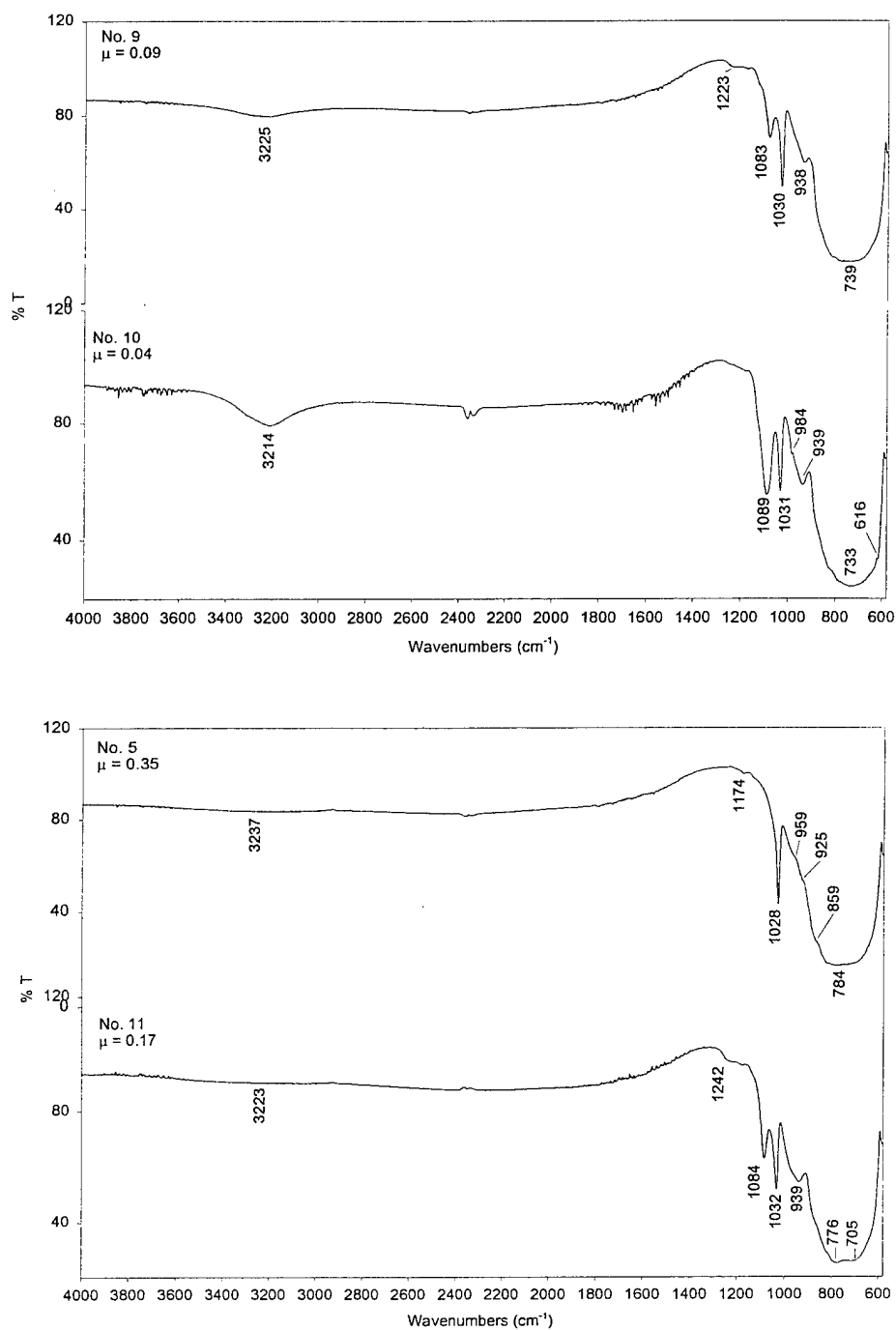
Figure 53. FTIR Spectra From Inside Wear Tracks of Low Friction (Top Two) and High
Friction (Bottom Two) Chemical Reaction Film Samples

86
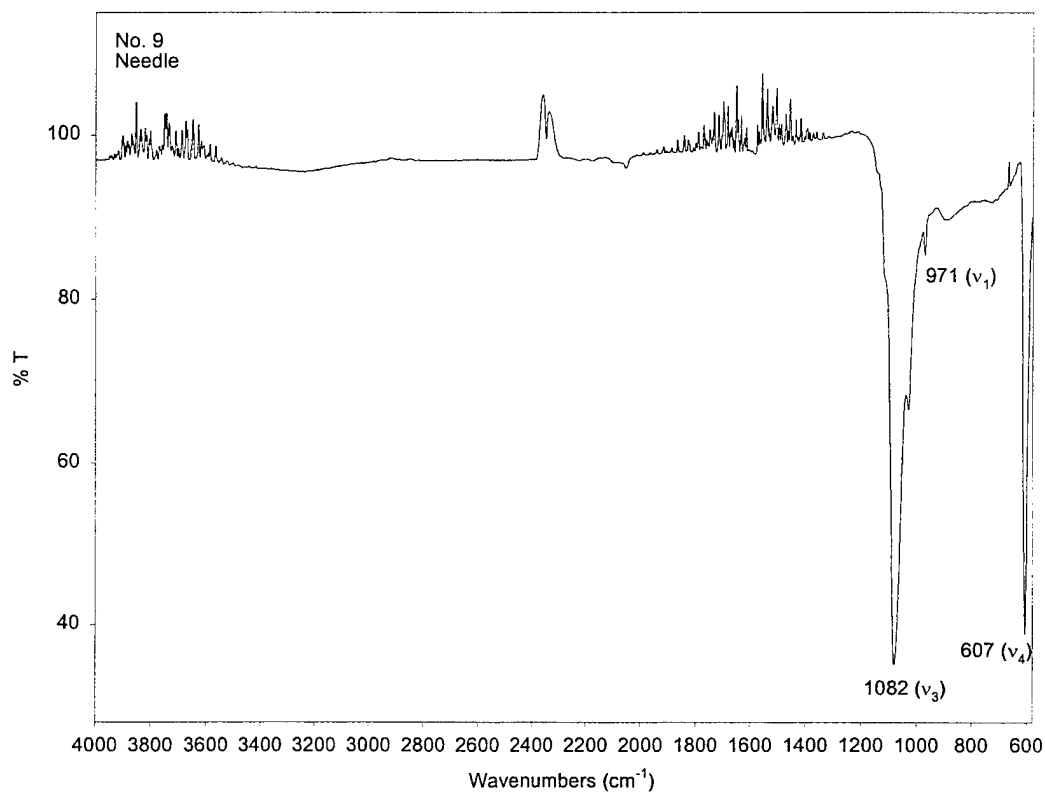
Figure 54. FTIR Spectrum of Cesium Sulfate Crystal (Needle) Found Near Edge of Wear
Track of Low-Friction Sample

5. DISCUSSION

5.1 Unlubricated Silicon Nitride

Studies show that the tribology of ceramics is exceptionally complex. The surrounding environment (i.e., oxidizing, humid, inert, etc.), presence (or absence) of third bodies (i.e., wear debris, transfer films, etc.), and operating conditions (speed, load, and temperature) all have a profound effect on friction and wear [35-43, 45, 47, 86-98]. According to Tomizawa and Fisher [35, 36], the sliding wear of Si_3N_4 in dry air is characterized by the generation of abrasive wear particles that result from the fracture of asperities (microfracture). These become trapped within the contact area and are subsequently pulverized and oxidized to a very fine dust that primarily consists of SiO_2. Under these conditions, wear surfaces appear dull and rough. Conversely, in humid air, the wear mechanism involves a combination of microfracture and tribochemistry, depending on the amount of water vapor present [35-37, 42, 43]. As the moisture content increases, tribochemistry begins to dominate the wear mechanism. This involves the formation of soft tribochemical films, believed to be amorphous hydrated silica ($SiO_2 xH_2O$). These soft films redistribute local contact stresses and can lower surface shear stresses resulting in lower friction and wear [36, 37, 92].

It is noteworthy that in water, the wear mechanism of Si_3N_4 is thought to proceed by tribochemistry alone and involves the dissolution of Si_3N_4 asperities [41, 94]. This results in ultrasmooth surfaces capable of supporting extremely thin hydrodynamic films and the absence of wear debris particles [94, 95]. Consequently, ultralow friction coefficients (μ < 0.002) can be obtained in water at very low Sommerfeld numbers ($S = V \eta/F$, where V = velocity, η = viscosity, F = load) [94, 96, 97]. The formation of colloidal silica has also been recently observed in water and has been suggested to act as a boundary lubricating film, playing a significant role in yielding the ultralow friction observed [97, 98]. These published studies are relevant to this work because, as will be discussed shortly, a somewhat analogous mechanism is observed with the cesium-based films studied here, albeit at much higher temperatures (600°C) and in relatively dry air, conditions where Si_3N_4 is expected to wear by microfracture.

In general, the friction and wear results obtained here are in agreement with that reported in the literature for Si_3N_4 sliding in dry air, despite that the near surface region of the as-received samples (< 1.0 μm depth) was uncharacteristic of Si_3N_4. Apart from a few exceptions [32, 99], the structural chemistry of the near surface region of starting materials, such as that attainable by FTIR, is usually not fully characterized and has been mainly disregarded in published studies that relate to the tribology of Si_3N_4 and other materials. Although there have been numerous studies that indicate the machining of ceramic surfaces generally results in surface and subsurface damage, which in turn affects mechanical and tribological properties [100-104], few comparable studies have been performed on the effects of machining and finishing on structural surface chemistry. The FTIR results obtained here suggest the presence of a modified layer, believed to arise

from the machining or finishing process. However, additional studies are required to further corroborate these results.

5.2 Solid Lubricated Silicon Nitride

5.2.1 Cesium Oxythiotungstate Bonded Coatings

The best frictional performance obtained on Cs_2WOS_3 bonded coatings was on those from the first series that were run-in (Group B). A mean friction coefficient of 0.17 ± 0.07 was obtained at 600°C, though steady-state friction coefficients as low as 0.09 were obtained in a few cases. The mean friction value obtained is nearly identical to that reported by King and Forster [28] on similar bonded coatings and is relatively low when compared to other high temperature (> 500°C) solid lubricants on silicon nitride [105]. The value, however, is significantly higher than the 0.03 friction coefficient obtained at 600°C by Strong [31] on pulsed-laser deposited Cs_2MoOS_3 thin films on Si_3N_4.

The friction traces obtained on samples from Group B suggest film formation during sliding. Also, the relatively high friction coefficients obtained during break-in of the coatings ($\mu_i \sim 0.30$ to 0.40) indicate that the bulk coating was not very lubricious at these test conditions. Since posttest examination of wear surfaces showed that all of the coatings from this group were worn through, the lubricious film must have been present as a thin film on the worn and polished substrate surface (primary wear track/wear scar). AES surface analysis confirmed the presence of thin films, approximately 80 to 110 nm thick, on the primary wear tracks of samples that gave low friction. Such a film was notably absent on a sample that gave high friction. The films are composed primarily of silicon and oxygen with lower levels of cesium, sodium, and tungsten, consistent with that of a mixed metal oxide silicate glass. Sulfur was also detected but at very low levels and was mostly confined to the near-surface region. This specific result is inconsistent with that reported by Strong, who did not detect sulfur on any of the wear tracks lubricated with Cs_2MoOS_3 exposed to high temperatures. The inconsistency is believed to be due to the difference in sliding distance or number of cycles. Friction experiments were typically 50,000 cycles or more in Strong's work and were 5,000 to 10,000 cycles long here. The longer sliding time in Strong's experiments would have allowed more time for sulfur species to react and volatilize from wear tracks.

The AES compositional depth profiles strongly suggests that chemical interactions involving the Si_3N_4 substrate (and/or SiO_2 layer), the coating constituents, and oxygen, has taken place. The shape of the profiles imply a diffusional mechanism, similar to that observed in the thermal oxidation of Si_3N_4 at higher temperatures [106, 107]. This is consistent with previous work [30] and the thermal analysis results presented in Appendix B that indicate that Cs_2WOS_3 / sodium silicate mixtures accelerate the oxidation of Si_3N_4 at relatively low temperatures (< 700°C). It is believed that this is caused by the glass-modifying nature of the metal oxides that are formed when Cs_2WOS_3, and perhaps the sodium silicate binder, thermally decompose in air.

89

It is well known that certain metal oxides, and in particular alkali metal oxides such as Cs_2O and Na_2O, can enter and modify the three-dimensional network of the SiO_2 glassy surface scale on silicon-based ceramics, diminishing its protective qualities [108, 109]. The excess oxygen provided by these oxides disrupts the SiO_2 network connectivity by causing bridging oxygen atoms connecting SiO_4 tetrahedra to be replaced by nonbridging oxygen atoms [108, 110]. The reaction could be expressed as:

$$\equiv Si\text{-}O_b\text{-}Si\equiv\ +\ M_2O\ \longrightarrow\ 2\equiv Si\text{-}O_{nb}M,$$
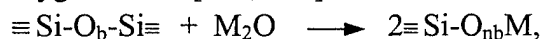
where M = Cs or Na and O_b and O_{nb} are bridging and nonbridging oxygen, respectively. In turn, the network breakdown results in an increase in cation mobility and accelerated mass transport across the SiO_2 scale, which can lead to increased oxidation rates [108, 111, 112]. Also, the alkali silicate glass that eventually forms through this process generally exhibits a significant reduction in shear strength, viscosity, and eutectic temperature when compared to pure SiO_2 [108, 111]. These are fundamental properties of low friction films. It should be remarked that the AES depth profiles showed that cesium and sodium were quite mobile during sputtering and appeared to pileup at the oxide-Si_3N_4 interface. This is in agreement with the foregoing discussion.

The role that tungsten plays here is less straightforward. Though it appeared to concentrate mostly at the surface of wear tracks, diffusion into the silicon oxide or silicate film was also apparent from the depth profiles. A number of tungsten compounds possible at the surface include the trioxide (WO_3), tungstates (i.e., Cs_2WO_4 or Na_2WO_4), tungsten bronzes of the form Cs_xWO_3 or Na_xWO_3, $0<x<1$, and alkali metal (M) tungstate glasses of the form $xM_2O(1\text{-}x)WO_3$. Based on the coordination number, valence, and bond strength of tetrahedrally coordinated tungsten oxide species, it is speculated that the tungsten found *inside* the film, acting as a glass former, replaces silicon in the SiO_2 network. This would tend to stabilize the network, which may not be desirable for very low friction. The lower friction obtained on the chemical reaction films, where tungsten was absent, tends to support this. This is not unreasonable considering that tungsten is a known intermediate in glass-forming systems [109] and its relatively small cation size makes it acquiescent for isomorphous substitution. Such substitutions have been observed with aluminum and other transition metals in silicate glasses [109, 113].

The wear rate of balls slid against bonded coatings was moderately high but within the range expected for solid lubricating behavior (10^{-6} $mm^3/N\,m$) [105, 114]. The optical micrographs strongly suggests that the wear debris played a significant role during sliding and probably had an affect on the measured friction coefficients. It is highly suspected, though it could not be fully substantiated here, that compacted debris trapped ahead of the ball imposed a frictional resistance during sliding that resulted in friction coefficients somewhat higher than what could have otherwise been achieved with this system. The relatively thick coatings studied here likely contributed to this problem.

Aged bonded coatings (Group C) showed a marked increase in friction, despite the running-in, indicating that a change in the coating had occurred. Surface analysis revealed the presence of a thin sodium carbonate layer on the surface of an aged sample. It is unknown if this layer was present on samples from Groups A and B since surface analysis was not conducted on any of the as-coated samples. Still, Raman detected

amorphous carbon at the edges of the wear track of a sample from Group B, implying that the carbonate film may have formed relatively quickly.

As indicated before, most of the Group C wear tracks contained pieces and sometimes entire segments of original coating material still attached to the substrate surface inside the wear tracks, suggesting that the physical properties of the coating and/or its bonding strength characteristics had changed with time. It is suspected that dehydration of the sodium silicate binder during storage resulted in a hard glassy coating that strongly adhered to the substrate. Water content in sodium silicate glasses is known to influence mechanical properties, with higher fracture strength observed at low water content or dry conditions [115]. Also, it is well known that sodium silicate binders slowly set (or harden) with time. Exposure to acidic gases, such as CO_2, SO_2, and H_2S, has been shown to accelerate the setting time and results in increased bond strength with the formation of highly condensed polysilicate species [116, 117]. The setting time, bond strength, and mechanical properties also depend on the pH of the sodium silicate binder, which in turn depends on the ratio of SiO_2 to Na_2O (also known as the modulus, m) [116, 118]. For instance, it is generally observed that higher modulus values (i.e., m = 3.0 to 4.0) produce films that are more brittle and whose rate of water loss are greater than those of lower modulus [118]. Although the silicate binder used here had an initial modulus of 2.88, the observed sodium-enrichment at the surface of the samples (as Na_2CO_3) indicates preferential leaching out of sodium from the coating. This would drive the silicate in the bulk coating to higher modulus values, potentially causing an increase in brittleness and water loss.

It is then reasonable to assume that during storage, hardening or polymerization of the silicate binder and an increase in coating-to-substrate bond strength was caused by a combination of factors, including storage in a low humidity laboratory environment, presence of atmospheric CO_2 and probably SO_2 from the Cs_2WOS_3 pigment, the natural tendency for the silicate binder to set with time, and the preferential leaching of sodium to the surface. The relatively high binder content in the bonded coatings investigated here (pigment-to-binder wt. ratio of 1:1.6) would cause a noticeable manifestation of these effects. A coating with lower silicate binder content or perhaps of lower modulus would probably help minimize these effects. It is therefore quite possible that the poor experimental reproducibility obtained on bonded coated bearings in previous studies may have been in part caused by these factors.

Because of the change encountered and the considerable wear debris generated, no further work was performed on silicate bonded Cs_2WOS_3 coatings. The research then focused on thin cesium silicate chemical reaction films formed on pre-oxidized Si_3N_4.

5.2.2 Chemical Reaction Films

The most significant findings from the research were obtained with chemical reaction films formed on pre-oxidized Si_3N_4. The results clearly show that the CsOH treatment given to pre-oxidized samples and the subsequent annealing in a sulfur-rich oxidizing environment (CsOH + SO_3 samples) results in thin films, ~ 170 nm thick, that

exhibit remarkable frictional and wear characteristics. The initial friction coefficient obtained at 600°C was 0.10 in all cases, though there was a sudden drop to 0.04 in one case after a short period of sliding. The wear scar of this particular sample showed evidence of liquid-like behavior. Wear factors were similar to those obtained with liquid boundary lubricating films at low temperatures. Moreover, the results provide conclusive evidence that neither tungsten nor molybdenum are needed for low friction and wear at 600°C. They also confirm that both cesium *and* sulfur are necessary since pre-oxidized samples containing only cesium or only sulfur displayed very high initial friction coefficients and high wear.

Similar to the bonded films, the AES depth profiles suggest that mass diffusion is involved in film formation with oxygen and nitrogen being the primary diffusing elements. Cesium also appeared to diffuse into the oxide. This is also consistent with the results reported by Strong. In general, the composition of the films is compatible with that of a mixed metal oxide silicate glass with high levels of oxygen and silicon and lower amounts of cesium. A major difference from that obtained with the bonded coatings and from Strong's work however, is that magnesium from the Si_3N_4 sintering aid was detected at significant levels inside the oxide films. The results show that magnesium diffuses out from the Si_3N_4 substrate during the static pre-oxidation given at 900°C. Based on AES depth profiles, it is estimated that the magnesium silicate scale is roughly 110 nm thick, and its composition agrees well with that of $MgSiO_3$ (enstatite) or $MgO \cdot SiO_2$. This is not altogether surprising, as the oxidation of polycrystalline Si_3N_4 materials sintered with magnesia show preferential migration of magnesium cations to the SiO_2 scale via grain boundaries [119-122]. In fact, there is general agreement in the literature that the outward diffusion of magnesium is the rate limiting step in the oxidation of Si_3N_4 materials containing this additive [119-122].

The results obtained on pre-oxidized samples that did not contain cesium but were annealed in sulfur-rich air suggests that the $MgSiO_3$ scale is not lubricious, presumably because of its very high eutectic temperature (>1500°C) [108]. The initial friction coefficient obtained on these was greater than 1.0 and wear factors were about $4x10^{-6}$ $mm^3/N \cdot m$. Oddly, relatively low friction coefficients (~ 0.17 to 0.21) were obtained after extensive sliding and wear. The AES depth profile detected only silicon and oxygen and no magnesium indicating that the $MgSiO_3$ scale had been worn away and was replaced with a soft silicon oxide film. This soft film was subsequently rolled into cylindrical rods 5 to 20 μm long. The loss of magnesium from grain boundaries probably also weakened the underlying Si_3N_4 grain structure, which in turn resulted in grain pullout during high friction sliding and high wear. The observation of very small voids and cracks throughout the wear track surface by SEM supports this.

Unlike the bonded coatings, where the lubricating film was believed to have formed during sliding, the $CsOH + SO_3$ samples displayed low initial friction coefficients, indicating that a lubricious film was on the surface prior to sliding. The surface analysis confirmed the presence of c-Cs_2SO_4 on the as-deposited film and as globules and needles outside the wear tracks of samples. Furthermore, the SEM and surface analysis of the sample that gave ultralow friction confirmed the presence of a narrow (~ 20 μm wide)

globular-like film near the center of the wear track that was mostly amorphous Cs_2SO_4. This implies that the initial friction coefficient of 0.10 was that of Cs_2SO_4 initially present on the surface. Low friction coefficients have been reported for various sulfates at high temperature, including Cs_2SO_4 [123, 124]. This result is important as it provides some clues as to the film formation mechanism.

It is apparent that Cs_2SO_4 deposits or droplets were formed on the surface during the annealing in sulfur-rich air. This indicates that SO_3 partial pressures were high enough for the reaction shown below to proceed.

$$2CsOH\ (s) + SO_3\ (g) \longrightarrow Cs_2SO_4\ (s) + H_2O\ (g)$$

AES depth profiles show that some of the cesium also diffuses into the magnesium oxide silicate layer, where it either recombines into a mixed oxide silicate glass of the form $xCs_2O\,yMgO\,zSiO_2$ or forms a separate cesium silicate phase. An important result is that the sample with the lowest friction exhibited the highest cesium-to-magnesium atomic ratio inside the oxide film. Therefore, a silicate film rich in cesium and low in magnesium appears to be essential for very low friction ($\mu \leq 0.04$). This is not surprising since $MgSiO_3$ showed high friction and alkali silicate glasses generally soften at lower temperatures than alkaline earth silicates [125, 126]. It is worth adding that the Si_3N_4 substrate material used by Strong was of high purity and contained no major additives. This would have favored the formation of cesium silicate alone and hence, the ultralow friction observed. Nonetheless, the results obtained here are of practical significance as most engineering or structural Si_3N_4 ceramics contain varying amounts of sintering aids, which as shown, can play a role in high-temperature tribology.

In view of the very smooth surface observed by SEM on the ultralow friction sample, it is apparent that a polishing mechanism was involved in the wear process. A tribo-chemical process, akin to that observed with water and with other chemical polishing media, is proposed here. In this case, however, the dissolution of SiO_2/Si_3N_4 asperities into a sulfate deposit melt with subsequent formation of a soft, lubricious silicate film results in a very smooth surface. The observation of liquid-like behavior and shallow fissures along the periphery of the sulfate globules supports this mechanism. These fissures are believed to be areas where the SiO_2 (or $MgSiO_3$) scale has dissolved into the sulfate. This would explain why magnesium and silicon were detected in the globular a-Cs_2SO_4 film by the Auger microprobe.

Therefore, it is proposed here that the Cs_2SO_4 deposit plays three important roles. First, it yields an initial low friction of about 0.10 at 600°C, minimizing surface damage and wear. Secondly, it serves as a polishing agent by dissolving SiO_2 via a hot-corrosion mechanism. And third, it serves as a reaction path for the formation of a lubricious cesium silicate glass by decomposing into Cs_2O and SO_3 during sliding. The process is analogous to the hot-corrosion of Si_3N_4 with Na_2SO_4 deposits under static conditions, but at much lower temperatures [112, 127, 128]. The two-step mechanism, which was proposed elsewhere [30, 31], is shown below:

$$Cs_2SO_4\ (l) \longrightarrow Cs_2O\ (l) + SO_3\ (g)$$
$$xSiO_2\ (s) + Cs_2O\ (l) \longrightarrow Cs_2O\,xSiO_2\ (l)$$
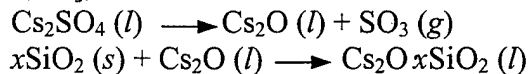
According to the hot-corrosion studies of Jacobson [112, 127] and Blanchere and Pettit [128] with Na_2SO_4, dissolution of acidic SiO_2, as shown above, is expected to occur at low SO_3 partial pressures (basic conditions) and at temperatures between the melting point and dew point of the sulfate. Although low SO_3 partial pressures were likely favored during sliding in air (basic conditions), the test temperature was obviously below the melting point of Cs_2SO_4 (1010°C). It is quite possible that the sliding action and the impurities present in the SiO_2 scale caused the Cs_2SO_4 to decompose at lower temperatures. Since the sliding velocity was too low for any significant increase in temperature, decomposition must have been primarily driven by tribo-chemical effects and by the impurities present. It is well known that friction and wear can accelerate chemical reaction rates [129]. Strong also observed that Cs_2SO_4 decomposed at temperatures below 700°C and attributed this to the frictional action during sliding [31]. In addition, MgO and carbon impurities are known to promote basic conditions by reducing the acidity of sulfate deposits [127, 128]. This results in an increase in wetting by the sulfate and a greater affinity between the sulfate and silica scale, causing an increase in hot-corrosion and SiO_2 dissolution at lower temperatures than for pure SiO_2 [128].

The FTIR results probably provide the most direct evidence of the formation of a silicate glass. As described previously, the excess oxygen provided by modifying cations in silicate glasses results in SiO_2 network breakdown as NB Si-O bonds are formed. FTIR is a reasonable tool for differentiating between bridging and NB Si-O bonds, though nuclear magnetic resonance (NMR) may have been better. The results illustrate that the molecular structure of the surface oxide on low-friction samples was largely of NB Si-O character, consistent with that of alkali silicates. More significantly, the Si-OH absorption band at about 3200 cm^{-1}, which was apparent in all of the low-friction samples and was most intense in the sample that gave 0.04 friction, further supports this given that alkali silicates have great affinity for moisture. The position of this band agrees with hydrogen bonded Si-OH of dissolved water [85]. Recent studies show that hydration reactions in alkali silicate glasses proceed as a result of the interaction between H_2O and NB Si-O bonds [130]. For cesium silicate, this could expressed as follows:
$$\equiv Si-O_{nb}Cs + H_2O \longrightarrow \equiv Si-OH\cdots(OH)^-Cs^+.$$
This would explain the higher intensity Si-OH absorption band in the ultralow friction sample, where more cesium silicate was formed and hence, more NB Si-O bonds were available for OH termination.
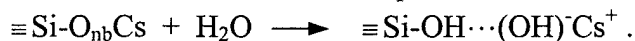
Finally, it is thought that the lubricious silicate films observed in this study are replenished, to some extent, by the inward diffusion of oxygen from the surrounding air and cesium oxides formed from a sulfate. The tenacity of the film is enhanced by this diffusional or oxidational mechanism, which produces a continuous and seamless film with no clear boundary or interface. Based on the analytical evidence, the mechanism represented in Figure 55 is proposed here. For simplicity, the carbon (or SiC) layer originally present on the samples is not taken into account. Nonetheless, it is believed that carbon would promote basic conditions, which would further augment Cs_2SO_4 decomposition and SiO_2 dissolution as shown [112].

94

Si$_3$N$_4$

bulk cesium sulfate deposit
containing Mg & Si

dissolved SiO$_x$ and other
surface impurities in
sulfate

Si$_3$N$_4$ particles being
slowly dissolved in
silicate

SO$_3$

N$_2$

O$_2$

SiO$_2$
(silicate layer)

Cs$_2$O

Mg^{++} ions

β-Si$_3$N$_4$ grains

glassy grain boundaries
mostly magnesium silicate
with other impurities
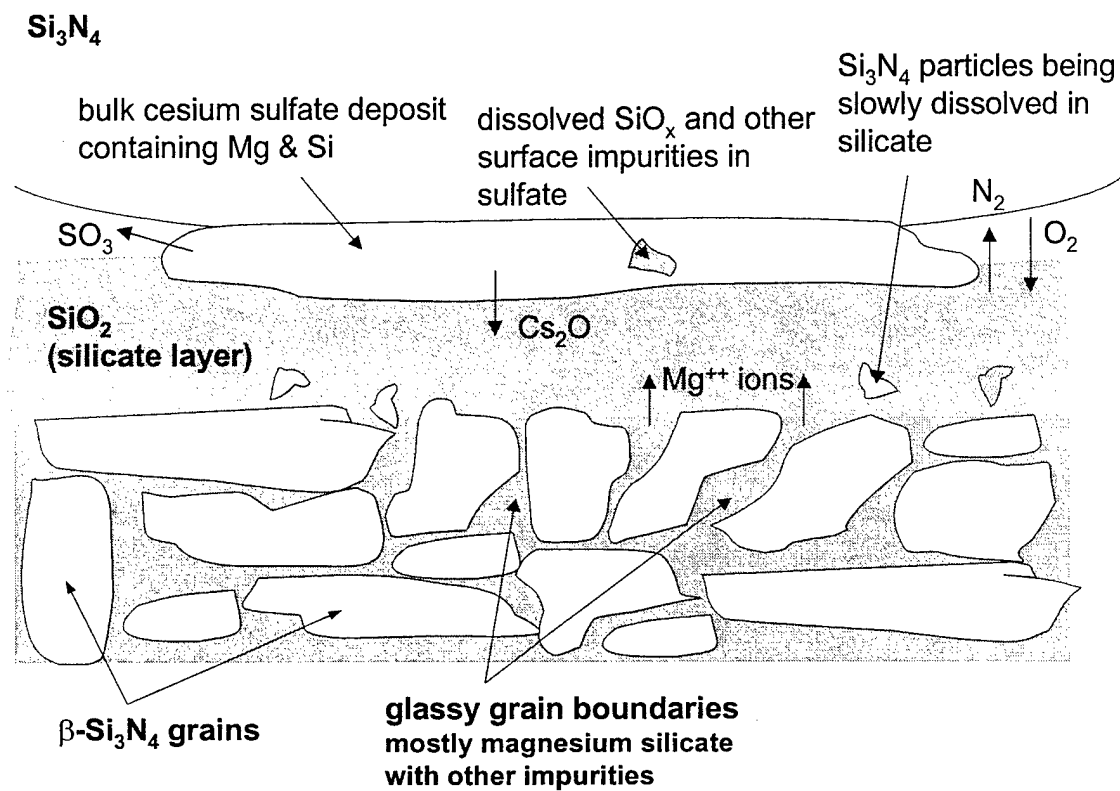
Figure 55. Schematic of Reactions Involved in the Proposed Tribo-Oxidational
Mechanism of Si$_3$N$_4$ at 600°C

95

6. CONCLUSIONS

The sliding friction and wear of unlubricated Si_3N_4 and Si_3N_4 lubricated with inorganic cesium-containing films was investigated in air, mostly at 600°C, using a ball-on-disk configuration. The surface morphology and chemistry of posttested samples was characterized using various analytical techniques. The main conclusions are as follows.

Results on unlubricated Si_3N_4 at 600°C were similar to that reported in the literature for Si_3N_4 sliding in dry air. Very high friction and wear was observed. Friction coefficients were in the range of 0.80, and high levels of wear occurred predominately by microfracture. Some tribo-chemical films, consistent with previous studies, were observed at 23°C and at the upper end of the relative humidity encountered in the study.

For the sodium silicate bonded Cs_2WOS_3 coatings, it was found that lower friction coefficients and reduced data scatter were obtained when coatings were given an initial running-in at low speed and reduced load. This resulted in a mean friction coefficient of 0.17 at 600°C. Although the coatings offered moderate wear protection to Si_3N_4 at 600°C, significant coating wear debris was generated in all cases. This was attributed to the thick coatings (~ 42 μm). The optical micrographs of worn surfaces indicate that the debris played a significant role during sliding, and it is believed that compacted debris trapped between the ball and disk, ahead of the sliding direction, resulted in higher friction coefficients than otherwise could have been achieved with this system.

The results also indicate that the bulk sodium silicate/Cs_2WOS_3 coating was not very lubricious at 600°C and that the actual lubricating film was formed during sliding as the bulk coating was worn through and rubbing contact with the Si_3N_4 substrate was established. This resulted in highly polished surfaces containing lubricious thin films, 80 to 110 nm thick, that were enriched with oxygen and silicon with lower levels of cesium, sodium, and tungsten. The composition is suggestive of a mixed metal oxide silicate glass. The oxides, which form when the sodium silicate-Cs_2WOS_3 system decomposes, modify the SiO_2 scale that naturally forms on silicon-based ceramics, lowering its shear strength, viscosity, and hardness. It is believed that at 600°C, the silicate is either a liquid or a very soft solid film. Also, the shape of the compositional profiles suggests that a diffusional mechanism, analogous to the thermal oxidation of Si_3N_4, is involved. No such film was detected on a sample that yielded high friction.

Silicate bonded Cs_2WOS_3 coatings that were aged for several months in ambient laboratory air resulted in extremely high friction coefficients ($\mu > 1.0$). These results were attributed to a combination of factors including dehydration of the sodium silicate binder, the natural tendency of the binder to set with time (hardening), and an increase in coating-to-substrate bond strength, caused by exposure of the binder to acidic SO_2/SO_3 gas from the Cs_2WOS_3 pigment and ambient CO_2 during storage. An increase in coating brittleness was probably caused by the leaching out of sodium. This was partly confirmed by Raman and FTIR analysis, which detected the presence of a sodium carbonate layer on the surface of an aged sample. The increased adhesion between the coating and substrate prevented intimate contact between the slider and Si_3N_4 substrate, which was

apparently necessary for the films to form. It is believed that these were major contributing factors to the poor experimental reproducibility in previous high-temperature bearing development studies that used sodium silicate bonded complex chalcogenide solid lubricants.

Of all the cesium-containing films investigated, the best tribological performance was obtained on pre-oxidized Si_3N_4 samples treated with CsOH annealed in a sulfur-rich oxidizing environment (CsOH + SO_3). The friction coefficient and wear factors obtained at 600°C were 0.04 to 0.10 and 4×10^{-9} to 1×10^{-8} mm^3/N m, respectively. These are comparable to values reported for liquid boundary lubricating films at much lower temperatures. The results also provide conclusive evidence that neither tungsten nor molybdenum is necessary for good tribological performance at the test conditions investigated here. In addition, the results strongly suggest that both cesium *and* sulfur are required, since films containing only cesium or only sulfur showed very high initial friction and high wear.

It was found that magnesium diffused out from the Si_3N_4 substrate (sintering aid) during the static pre-oxidation and segregated towards the surface as $MgSiO_3$ or $MgO\ SiO_2$ (the pre-oxidation was given in order to thicken the natural SiO_2 scale and facilitate the formation of cesium silicate by CsOH treatment). Furthermore, the results indicate that the $MgSiO_3$ layer is not lubricious at 600°C and that a silicate film rich in cesium and low in magnesium seemed necessary for ultralow friction ($\mu \sim 0.04$).

The initial friction coefficient of 0.10 obtained on the CsOH + SO_3 films was attributed to Cs_2SO_4 deposits formed during annealing. This was confirmed by AES, Raman, and FTIR analysis. The sudden drop in friction observed on one sample after a short period of sliding was attributed to the higher cesium and lower magnesium levels found in inside the silicate film. The wear scar of this sample also showed evidence of liquid-like behavior and SEM showed that the wear track surface was extremely smooth and showed the presence of a globular-like film inside the wear track. Surface analysis confirmed this film to be mostly amorphous Cs_2SO_4.

It is proposed that the Cs_2SO_4 deposit plays three important roles: (1) it provides an initial low friction coefficient of about 0.10 at 600°C, minimizing surface damage and wear, (2) it serves as a polishing agent by dissolving SiO_2 asperities, hence producing very smooth surfaces that can carry very thin films with minimal asperity interaction, and (3) it provides a reaction path for the formation of a lubricious cesium silicate glass by decomposing into Cs_2O and SO_3 gas during sliding, similar to the hot-corrosion of Si_3N_4 with Na_2SO_4 deposits under static conditions. The energy provided by the sliding process (i.e., tribo-chemical effect) and impurities present in the SiO_2 scale (carbon and MgO) are believed to drive this decomposition. The lubricious silicate film is formed as Cs_2O diffuses into the SiO_2 scale and causes breakdown of the SiO_2 network. This lowers the shear strength, softening point, and viscosity of the film. The film is replenished by the inward diffusion of oxygen from the surrounding air and cesium oxide from the sulfate. This tribo-oxidational mechanism creates a tenacious film that is resistant to delamination and wear, since it is essentially diffusion-bonded to the substrate.

7. RECOMMENDATIONS FOR FUTURE WORK

The results of this study have shown that the films produced by the CsOH + SO$_3$ treatment developed here can provide remarkably low sliding friction and excellent wear protection to Si$_3$N$_4$ at very high temperatures. This system offers some potential advantages since it requires no binder and theoretically could be applied to complex Si$_3$N$_4$ parts. Also, the films produced are sufficiently thin so that wear debris generation is kept to a minimum. However, more work is clearly needed to apply this to high-speed, full-scale rolling element bearings. The following are some areas that require further study.

1. Optimization of the annealing process should be undertaken under well controlled O$_2$/SO$_2$/SO$_3$ partial pressures and at annealing temperatures and times beyond those investigated here. This should also involve a comprehensive thermodynamic analysis of the hot-corrosion process (i.e., Gibbs free energy calculations), which would provide insight to better control the reactions.
2. The tribological characteristics should be investigated at lower temperatures. If necessary, low temperature performance could be enhanced with WS$_2$. Though, high temperature oxidation of WS$_2$ to WO$_3$ and the effect this would have on the high temperature film formation would certainly have to be considered.
3. The structure of the lubricious films should be investigated further using other surface analytical techniques such as NMR. This technique has been successfully used to study the molecular structure of silicate glasses and would provide invaluable information regarding film structure. Cross-sectional imaging of wear tracks using transmission electron microscopy (TEM) would also be extremely fruitful in determining the exact mechanisms of film formation and wear.
4. Finally, the effect of Si$_3$N$_4$ pre-oxidation (i.e., SiO$_2$ scale thickness) and sintering aids on friction and wear are areas that obviously merit further study. The outward diffusion of MgO observed in this study and the apparent negative effect it had on friction shows that this needs to be better understood. It may be possible to bypass the pre-oxidation step if a sufficiently thick SiO$_2$ layer is initially present on the surface. This would minimize the outward diffusion of MgO. The selection of an alternate Si$_3$N$_4$ material with a different sintering aid package is another solution. Other widely used oxide-sintering aids, such as Al$_2$O$_3$ and Y$_2$O$_3$, are not quite as mobile as MgO and tend to stabilize the glassy grain boundary phase. However, this improves the hot-corrosion resistance, which may inhibit the formation of a lubricious silicate film. In the same fashion that MgO appeared to increase friction, other sintering aids may be tailored to reduce friction by forming a glassy film with optimum viscosity and shear strength properties. This could be a viable approach for extreme temperature (> 600°C), limited-life applications in which film lubricity and endurance are enhanced by the intentional and sacrificial leaching out of sintering aids.

8. REFERENCES

1. Macks, E. F., Nemeth, Z. N., and Anderson, W. J., "Preliminary Investigation of Molybdenum Disulfide – Air Mist Lubrication of Roller Bearings Operating to DN Values of 1x10^6 and Ball Bearings Operating to Temperatures of 1000°F," *NACA RM* E51G31 (1951).

2. Nemeth, Z. N. and Anderson, W. J., "Investigation of Temperature Limitations of Various Lubricants for High Temperature 20-Millimeter-Bore Ball Bearings," *NACA TN* 3337 (1955).

3. Nemeth, Z. N. and Anderson, W. J, "Effect of Air and Nitrogen Atmospheres on the Temperature Limitations of Liquid and Solid Lubricants in Ball Bearings," *Lubr. Eng.*, 11(4), pp. 267-273 (1955).

4. Bailey, C.H. and Sorem, S.S., "Research in High Temperature Bearing Lubrication in the Absence of Liquid Lubricants," WADC-TR-370, Part I (1956).

5. Bisson, E. E., Johnson, R. L., and Anderson, W. J., "Friction and Lubrication with Solid Lubricants at Temperatures to 1000°F with Particular Reference to Graphite," *Proc. Conf. on Lubr. and Wear, Inst. Mech. Engr.*, pp. 348-354 (1957).

6. Devine, M. J., Lamson, E. R., and Bowen, J. H., Jr., "The Lubrication of Ball Bearings with Solid Films," Paper 61-LUBS-11, ASME (1961).

7. Wilson, D. S., "Evaluation of Unconventional Lubricants at 1200°F in High-Speed Rolling Contact Bearings," Paper 61-LUBS-9, ASME (1961).

8. Sliney, H. E., "Bearings Run at 1250°F with Solid Lubricants," *Space Aero.*, **35**(3), pp. 91-100 (1961).

9. Schlosser, A., "The Development of Lubricants for High-Speed Rolling Contact Bearings Operating Over the Range of Room Temperature to 1200 Degrees Fahrenheit," Prog. Rep. 5, Stratos Div., Fairchild Engine and Airplane Corp. (1962).

10. Taylor, K.M., Sibley, L.B., and Lawrence, J.C., "Development of a Ceramic Rolling Contact Bearing for High Temperature Use," *Wear*, **6**, pp. 226-240 (1963).

11. Wallerstein, S., "Application of a Powder Lubrication System to a Gas Turbine Engine," AFAPL-TR-65-43 (1965).

12. Boes, D.J. and Bober, E.S., "Solid Film Lubrication Research," AFAPL-TR-66-10, Westinghouse Research Laboratories (1967).

13. Sliney, H. E. and Johnson, R. L., "Preliminary Evaluation of Greases to 600°F and Solid Lubricants to 1500°F in Ball Bearings," *ASLE Trans.*, 11, pp. 330-337 (1968).

14. Dayton, R. D., "Experimental Investigation of AgHg-WTFE-MoSe$_2$ Solid Lubricated Ball Bearings for High Speed, High Temperature, and High Load Applications," AFAPL-TR-71-100 (1972).

15. Dayton, R. D. and Sheets, M. A., "Evaluation of Grooved Solid Lubricated Bearings," AFAPL-TR-75-76 (1976).

16. Gardos, M. N., "Solid Lubricated Rolling Element Bearings," AFWAL-TR-83-4129 (1984).

17. Bisson, E. E. and Anderson, W. J., "Advanced Bearing Technology," *NASA* SP-38, pp. 203-257, pp. 309-370 (1965).

18. Devine, G. M. and Cerini, J. P., "Investigation of a Systems Concept for High Temperature Solid Lubricated Bearings – Phase II," AFWAL-TR-88-2078 (1988).

19. Forster, N. H., "High Temperature Lubrication of Rolling Contacts with Lubricants Delivered From the Vapor Phase and as Oil Mists," WL-TR-97-2003 (1997).

20. Müller, A. and Diemann, E., "Darstellung einiger Di, Tri- und Tetrathio-molybdate und wolframate," *Z. Naturforsch.*, 23b, p. 1607 (1968).

21. Müller, A., Diemann, E., Krebs, B., and Leroy, M., "Trithiomolybdates," *Angew. Chem. internat. Edit.*, 7 (10), p. 817 (1968).

22. Müller, A. and Diemann, E., "Preparation and Structural Chemistry of Mixed Oxo-Thio-Seleno Metalates," *Angew. Chem. internat. Edit.*, 8 (11), p. 914 (1969).

23. King, J. P. and Asmeron, Y., "Investigation of Extreme-Pressure and Antiwear Properties of Antimony Thioantimonate," *ASLE Trans.*, 24(4), pp. 497-507 (1981).

24. King, J. P. and Asmeron, Y., "Solid Lubricants for Improved Wear Resistance," Final Report, AD A120092 (1982).

25. King, J. P., "Lubricating Compositions and Process Using Complex Metal Chalcogenides," U.S. Patent 4,465,604, Aug. 1984.

26. Devine, M. J. and Devine, G. M., "Investigation of a Systems Concept for High Temperature Solid Lubricated Bearings," Progress Report, Air Force Contract F33615-84-C-2462, November 1984.

27. Galbato, A. T., "High Temperature Solid Lubricant Bearing Development," WRDC-TR-90-2085 (1990).

28. King, J.P. and Forster, N.H., "Synthesis and Evaluation of Novel High Temperature Solid Lubricants," AIAA Paper 90-2044, presented at AIAA, SAE, ASME, and ASEE Joint Propulsion Conference, 26th, Orlando, FL, July 16-18, 1990.

29. Rosado, L., Forster, N. H., Trivedi, H. K., and King, J. P., "Solid Lubrication of Silicon Nitride with Cesium-Based Compounds: Part I – Rolling Contact Endurance, Friction and Wear," *Trib. Trans.*, **43**(3), pp. 489-497 (2000).

30. Rosado, L., Forster, N. H., and Wittberg, T. N., "Solid Lubrication of Silicon Nitride with Cesium-Based Compounds: Part II – Surface Analysis," *Trib. Trans.*, **43**(3), pp. 521-527 (2000).

31. Strong, K. L., "Tribological Properties of Pulsed Laser Deposited Thin Films of Cesium Oxythiomolybdate," Ph.D. Dissertation, U. of Dayton (2000).

32. Hah, S. R., Fischer, T. E., and Burk, C., "Vol 4, Tribochemical Finishing of Silicon Nitride," WL-TR-96-4018 (1995).

33. Lui, M. and Nemat-Nasser, S., "Microstructure of a Bearing-Grade Silicon Nitride," *J. Mater. Res.*, **14**(12), pp. 4621-4629 (1999).

34. Lu, P., Danforth, S. C., and Symons, W. T., "Microstructure and Grain-Boundary Characterization of HIP'ed High-Purity Silicon Nitride," *J. Mater. Sci.*, **28**(15), pp. 4217-4222 (1993).

35. Tomizawa, H. and Fischer, T. E., "Friction and Wear of Silicon Nitride at 150°C to 800°C," *ASLE Trans.*, **29**, 4, pp. 481-488 (1985).

36. Fischer, T. E. and Tomizawa, H., "Interaction of Tribochemistry and Microfracture in the Friction and Wear of Silicon Nitride," *Wear*, **105**, pp. 29-45 (1985).

37. Sasaki, S., "The Effects of the Surrounding Atmosphere on the Friction and Wear of Alumina, Zirconia, Silicon Carbide, and Silicon Nitride," *Wear*, **134**, pp. 185-200 (1989).

38. Skopp, A., Woydt, M., and Habig, K. H., "Unlubricated Sliding Friction and Wear of Various Si_3N_4 Pairs Between 22° and 1000°C," *Trib. Intl.*, **23**, 3, pp. 189-199 (1990).

39. Ying, T. N., Shen, M. C., Wang, Y. S., and Hsu, S. M., "Tribology of Si-Based Ceramics: Wear Mechanisms," *Trib. Trans.*, **40**, 4, pp. 685-693 (1997).

40. Melandri, C., Gee, M. G., de Portu, G., and Guicciardi, S., "High Temperature Friction and Wear Testing of Silicon Nitride Ceramics," *Trib. Intl.*, **28**, 6, pp. 403-413 (1995).

41. Sugita, T., Ueda, K., and Kanemura, Y., "Material Removal Mechanism of Silicon Nitride During Rubbing in Water," *Wear*, **97**, pp. 1-8 (1984).

42. Jahanimir, S. and Fisher, T. E., "Friction and Wear of Silicon Nitride Lubricated by Humid Air, Water, Hexadecane + 0.5 Percent Stearic Acid," *STLE Trans.*, **31** (1), pp. 32-43 (1987).

43. Fisher, T., E., Zhu, Z., Kim, H., and Shin, D. S., "Genesis and Role of Wear Debris in Sliding Wear of Ceramics," *Wear*, **245**, pp. 53-60 (2000).

44. Blau, P. J., Friction and Wear Transitions of Materials, Noyes Publ., Park Ridge, pp. 271-348 (1989).

45. Winn, A. J., Dowson, D., and Bell, J. C., "The Lubricated Wear of Ceramics - Part I: The Wear and Friction of Silicon Nitride, Alumina, and Steel in the Presence of Mineral Oil Based Lubricant," *Trib. Intl.*, **28** (6), pp. 383-393 (1995).

46. Yust, C. S. and DeVore, C. E., "The Friction and Wear of Lubricated Si_3N_4 / $SiC_{(w)}$ Composites," *Trib. Trans.*, **34** (4), pp. 497-504 (1991).

47. Gates, R. S. and Hsu, S. M., "Silicon Nitride Boundary Lubrication: Effect of Phosphorus-Containing Organic Compounds," *Trib. Trans.*, **39** (4), pp. 795-802 (1996).

48. Winn, A. J., Dowson, D., and Bell, J. C., "The Lubricated Wear of Ceramics - Part II: The Wear and Friction of Silicon Nitride and Steel in the Presence of Mineral Oil or an Ester Based Lubricant," *Trib. Intl.*, **28** (6), pp. 395-402 (1995).

49. Shewmon, P. G., Diffusion in Solids, The Minerals, Metals & Materials Society, 2nd Ed., pp. 19-24 (1989).

50. Borg, R. J. and Dienes, G. J., An Introduction to Solid State Diffusion, Academic Press, Inc., San Diego, CA, pp. 15-18 (1988).

51. Pantano, C. G., Dove, D. B., and Onoda, G. Y., "Glass Surface Analysis by Auger Electron Spectroscopy," *J. Non-Cryst. Sol.*, **19**, pp. 41-53 (1975).

52. Zabinski, J. S. and McDevitt, N. T., "Raman Spectra of Inorganic Compounds Related to Solid State Tribochemical Studies," WL-TR-96-4034, p. 54 (1996).

53. Lucazeau, G. and Abello, L., "Micro-Raman Analysis of Residual Stresses and Phase Transformation in Crystalline Silicon Under Microindentation," *J. Mater. Res.*, **12** (9), pp. 2262-2273 (1997).

54. Clarke, D. R. and Adar, F., "Raman Microprobe Spectroscopy of Polyphase Ceramics," from <u>Advances in Materials Characterization</u>, Vol. 15, Plenum Publ. Corp., Eds. Rossington, D. R., Condrate, R. A., and Snyder, R. L., p. 199 (1983).

55. Zabinski, J. S. and McDevitt, N. T., "Raman Spectra of Inorganic Compounds Related to Solid State Tribochemical Studies," WL-TR-96-4034, p. 55 (1996).

56. Matson, D. W., Sharma, S. K., and Philpotts, J. A., "The Structure of High-Silica Alkali-Silicate Glasses, A Raman Spectroscopic Investigation," *J. Non-Cryst. Sol.*, **58**, pp. 323-352 (1983).

57. Brinker, C. J. and Scherer, G. W., <u>Sol-Gel Science-The Physics and Chemistry of Sol-Gel Processing</u>, Academic Press Inc., Boston, pp. 541-546 (1990).

58. Müller, A., Weinstock, N., and Schulze, H., "Laser-Raman-Spektren der Ionen MoS_4^{2-}, WS_4^{2-}, $MoOS_3^{2-}$, and WOS_3^{2-} in wässriger Lösung sowie der entsprechenden kristallinen Alkalisalze," *Spectrochim. Acta*, **28A**, pp. 1075-1082 (1972).

59. Colthup, N. B., Daly, L. H., and Wiberley, S. E., <u>Introduction to Infrared and Raman Spectroscopy</u>, Academic Press, Boston, p. 310 (1990).

60. Nyquist, R. A., Putzig, C. L., and Leugers, M. A., "Infrared and Raman Spectral Atlas of Inorganic Compounds and Organic Salts: Raman Spectra," from the <u>Handbook of Infrared and Raman Spectra of Inorganic Compounds and Organic Salts</u>, Vol. 2, Academic Press, San Diego, p. 60 (1997).

61. Cape, T. W., Maroni, V. A., Cunningham, P. T., and Bates, J. B., "Raman and IR-Emission Studies of Some Tungstate- and Molybdate-Containing Melts," *Spectrochim. Acta*, **32A**, pp. 1219-1223 (1976).

62. Burcham, L. J. and Wachs, I. E., "Vibrational Analysis of the Two Non-Equivalent, Tetrahedral Tungstate (WO_4) Units in $Ce_2(WO_4)_3$ and $La_2(WO_4)_3$," *Spectrochim. Acta*, Part A, **54**, pp. 1355-1368 (1998).

63. Nyquist, R. A., Putzig, C. L., and Leugers, M. A., "Infrared and Raman Spectral Atlas of Inorganic Compounds and Organic Salts: Raman Spectra," from the <u>Handbook of Infrared and Raman Spectra of Inorganic Compounds and Organic Salts</u>, Vol. 2, Academic Press, San Diego, pp. 148-149 (1997).

64. Nakamizo, M., Kammereck, R., and Walker, P. L., "Laser Raman Studies of Carbon," *Carbon*, **12**, pp. 259-267 (1974).

65. Horsley, J. A., Wachs, I. E., Brown, J. M., Via, G. H., and Hardcastle, F. D., "Structure of Surface Tungsten Oxide Species in the WO_3/Al_2O_3 Supported Oxide

System from X-ray Absorption Near-Edge Spectroscopy and Raman Spectroscopy," *J. Phys. Chem.*, **91**, pp. 4014-4020 (1987).

66. Montero, S., Schmölz, R., and Haussühl, S., "Raman Spectra of Orthorhombic Sulfate Single Crystals, I: K_2SO_4, Rb_2SO_4, Cs_2SO_4, and Tl_2SO_4," *J. Raman Spectrosc.*, **2**, pp. 101-113 (1974).

67. Luongo, J. P., "Infrared Characterization of α- and β-Crystalline Silicon Nitride," *J. Electrochem. Soc.*, **130** (7), pp. 1560-1562 (1983).

68. Takase, A., Umebayashi, S., and Kishi, K., "Infra-Red Absorption Spectroscopic Study of β-Sialons in the System Si_3N_4-Al_2O_3·AlN," *Jpn. J. Appl. Phys.*, **21** (10), pp. 1447-1450 (1982).

69. Luongo, J. P., "IR Study of Amorphous Silicon Nitride Films," *Appl. Spectrosc.*, **38**(2), pp. 195-199 (1984).

70. Lisovskii, I. P., Litovchenko, V. G., Lozinskii, V. B., Frolov, S. I., Flietner, H., Fussel, W., and Schmidt, E., "IR Study of Short-Range and Local Order in SiO_2 and SiO_x Films," *J. Non-Cryst. Sol.*, **187**, pp. 91-91 (1995).

71. Suchaneck, G., Steinke, O., Alhallani, B., and Schade, K., "Oxygen-Rich Phase Segregation in PECVD a-SiO_x:H Semi-Insulators," *J. Non-Cryst. Sol.*, **187**, pp. 86-90 (1995).

72. Trchová, M., Zemek, J., and Jurek, K., "Photoelectron and Infrared Spectroscopy of Semi-Insulating Silicon Layers," *J. Appl. Phys.*, **82**(7), pp. 3519-3527 (1997).

73. Dkaki, M., Calcagno, L., Makthari, A. M., and Raineri, V., "Infrared Spectroscopy and Transmission Electron Microscopy of Polycrystalline Silicon Carbide," *Mater. Sci. in Semicond. Proc.*, **4**, pp. 201-204 (2001).

74. Xu, H. H. K. and Jahanmir, S., "Simple Technique for Observing Subsurface Damage in Machining of Ceramics," *J. Am. Ceram. Soc.*, **77**, pp. 1388-1390 (1994).

75. Odén, M. and Ericson, T., "Near-Surface Deformation in an Alumina-Silicon Carbide-Whisker Composite due to Surface Machining," *J. Am. Ceram. Soc.*, **79**, pp. 2134-2140 (1996).

76. Baraton, M. I., Marchand, R., and Quintard, P., "Comparative Infrared Study of Silicon and Germanium Nitrides," *J. Mol. Struct.*, **143**, pp. 9-12 (1986).

77. Garrido, B., Samitier, J., Bota, S., Dominguez, C., Montserrat, J., and Morante, J. R., "Structural Damage and Defects Created in SiO_2 Films by Ar Ion Implantation," *J. Non-Cryst. Sol.*, **187**, pp. 101-105 (1995), and references thereof.

78. Brinker, C. J. and Scherer, G. W., <u>Sol-Gel Science, The Physics and Chemistry of Sol-Gel Processing</u>, Academic Press, Boston, p. 544 (1990).

79. Ward, G. L. and Lewis, M. H., "Oxynitride Glasses and Their Glass-Ceramic Derivatives," from <u>Glasses and Glass-Ceramics</u>, Chapman and Hall, London, Ed. Lewis, M. H., p. 126 (1989).

80. Vuotto, J. L., Huong, P. V., and Meaudre, R., "Structure of Amorphous Hydrogenated Silicon-Nitrogen Alloys Studied by Fourier Transform Infrared Spectroscopy," *J. Mol. Struct.*, **143**, pp. 13-16 (1986).

81. Nyquist, R. A., Putzig, C. L., and Leugers, M. A., "Infrared and Raman Spectral Atlas of Inorganic Compounds and Organic Salts: Infrared Spectra," from the <u>Handbook of Infrared and Raman Spectra of Inorganic Compounds and Organic Salts</u>, Vol. 3, Academic Press, San Diego, p. 56 (1997).

82. Mackenzie, K. J. D., Brown, I. W. M., Ranchod, P., and Meinhold, R. H., "Silicate Bonding of Inorganic Materials: Part I – Chemical Reactions in Sodium Silicate at Room Temperature," *J. Mater. Sci.*, **26**, pp. 763-768 (1991).

83. Carter, M. M. C., McIntyre, N. S., King, H. W., and Pratt, A. R., "The Aging of Silicate Glass Surfaces in Humid Air," *J. Non-Cryst. Sol.*, **220**, pp. 127-138 (1997) and references thereof.

84. Koenderink, G. H., Brzesowsky, R. H., and Balkenende, A. R., "Effect of the Initial Stages of Leaching on the Surface of Alkaline Earth Sodium Silicate Glasses," *J. Non-Cryst. Sol.*, **262**, pp. 80-98 (2000).

85. Colthup, N. B., Daly, L. H., and Wiberley, S. E., <u>Introduction to Infrared and Raman Spectroscopy</u>, Academic Press, Boston, p. 210 and 358 (1990).

86. Muratov, V. A., Luangvaranunt, T., and Fisher, T. E., "The Tribochemistry of Silicon Nitride: Effects of Friction, Temperature, and Sliding Velocity," *Trib. Intl.*, **31**(10), pp. 601-611 (1998).

87. Fischer, T. E., Anderson, M. P., Jahanimir, S., and Salher, R., "Friction and Wear of Tough and Brittle Zirconia in Nitrogen, Air, Water, Hexadecane and Hexadecane Containing Stearic Acid," *Wear*, **124**, pp. 133-148 (1988).

88. Denape, J. and Lamon, J., "Sliding Friction of Ceramics: Mechanical Action of the Wear Debris," *J. Mater. Sci.*, **25**, pp. 3592-3604 (1990).

89. Ajayi, O. O. and Ludema, K. C., "Mechanism of Transfer Film Formation During Repeat Pass Sliding of Ceramic Materials," *Wear*, **140**, pp. 191-206 (1990).

90. Imada, Y., Kamamura, K., Honda, F., and Nakajima, K., "The Tribological Reaction Accompanying Friction and Wear of Silicon Nitride Containing Titanium Nitride," *J. of Trib.*, **114**, pp. 230-235 (1992).

91. Gee, M. G., "The Formation of Aluminum Hydroxide in the Sliding Wear of Alumina," *Wear*, **153**, pp. 201-227 (1992).

92. Gee. M. and Butterfield, D., "The Combined Effect of Humidity and Sliding Speed on the Wear of Silicon Nitride," *Wear*, **162-164**, pp. 234-245 (1993).

93. Jisheng, E., Stolarski, T. A., and Gawne, D. T., "Mechanical and Tribochemical Effects During Accelerated Wear of Silicon Nitride in Diamond Slurries," *Trib. Trans.*, **40** (4), pp. 597-604 (1997).

94. Tomizawa, H. and Fisher, T. E., "Friction and Wear of Silicon Nitride and Silicon Carbide in Water: Hydrodynamic Lubrication at Low Sliding Speed Obtained by Tribochemical Wear," *ASLE Trans.*, **30**(1), pp. 41-46 (1987).

95. Saito, T., Imada, Y., and Honda, F., "An Analytical Observation of the Tribochemical Reaction of Silicon Nitride Sliding with Low Friction in Aqueous Solutions," *Wear*, **205**, pp. 153-159 (1997).

96. Chen, M., Kato, K., and Adachi, K., "The Difference in Running-In Period and Friction Coefficient Between Self-Mated Si_3N_4 and SiC Under Water Lubrication," *Trib. Ltr.*, **11** (1), pp. 23-28 (2001).

97. Xu, J., Kato, K., and Hirayuma, T., "The Transition of Wear Mode During the Running-in Process of Silicon Nitride Sliding in Water," *Wear*, **205**, pp. 55-63 (1997).

98. Xu, J. and Kato, K., "Formation of Tribochemical Layer of Ceramics Sliding in Water and its Role for Low Friction," *Wear*, **245**, pp. 61-75 (2000).

99. Bertrand, P. A., "Reactions of Tricresyl Phosphate with Bearing Materials," *Trib. Ltr.*, **3**, pp. 367-377 (1997).

100. Blau, P. J., "Effects of Surface Preparation on the Friction and Wear Behavior of Silicon Nitride / Silicon Carbide Sliding Pairs," *J. Mater. Sci.*, **27**, pp. 4732-4740 (1992).

101. Bandyopadhyay, B. P., "The Effects of Grinding Parameters on the Strength and Surface Finish of Two Silicon Nitride Ceramics," *J. Mater. Proc. Tech.*, **53**, pp. 533-543 (1995).

102. Blau, P. J., Martin, R. L., and Zanoria, E. S., "Effects of Surface Grinding Conditions on the Reciprocating Friction and Wear Behavior of Silicon Nitride," *Wear*, **203-204**, pp. 648-657 (1997).

103. Zanoria, E. S. and Blau, P. J., "Effects of Machined Surface Condition on the Repeated Impact Behavior of Silicon Nitride," *Wear*, **218**, pp. 66-77 (1998).

104. Zanoria, E. S., Watkins, T. R., Breder, K., Riester, L., Bashkansky, M., Reintjes, J., Sun, J. G., Ellingson, W. A., and Blau, P. J., "Assessment of Techniques for Characterizing the Surface Quality of Ground Silicon Nitride," *J. Mater. Eng. Perf.*, 7(4), pp. 533-547 (1998).

105. Murray, S. F. and Calabrese, S. J., "Effect of Solid Lubricants on Low Speed Sliding Behavior of Silicon Nitride at Temperatures to 800°C," *Lubr. Engr.*, **49**(12), pp. 955-964 (1993).

106. Ogbuji, L. U. and Byran, S. R., "The SiO_2-Si_3N_4 Interface, Part I: Nature of the Interface," *J. Am. Ceram. Soc.*, **78**(5), pp. 1272-1278 (1995).

107. Ogbuji, L. U., "The SiO_2-Si_3N_4 Interface, Part II: O_2 Permeation and Oxidation Reaction," *J. Am. Ceram. Soc.*, **78**(5), pp. 1279-1284 (1995).

108. Kingery, W. D., Bowen, H. K., and Uhlmann, D. R., Introduction to Ceramics, 2nd Ed., John Wiley & Sons, New York (1993).

109. Rawson, H., Inorganic Glass-Forming Systems, Academic Press, London (1967).

110. Hannon, A. C, Vessal, B., and Parker, J. M., "The Structure of Alkali Silicate Glasses," *J. Non-Cryst. Sol.*, **150**, pp. 97-102 (1992).

111. Cheong, Y., Du, H., and Withrow, S. P., "Reduction of Sodium-Accelerated Oxidation of Silicon Nitride Ceramics by Aluminum Implantation," *J. Mater. Sci.*, **32**, pp. 2391-2396 (1997), and references thereof.

112. Jacobson, N. S., "Corrosion of Silicon-Based Ceramics in Combustion Environments," *J. Am. Ceram. Soc.*, **76**(1), pp. 3-28 (1993).

113. Uhlmann, D. R. and Kreidl, N. J., Glass: Science and Technology, Vol. 1-Glass-Forming Systems, Academic Press, New York, p. 159 (1983).

114. Dunaevsky, V. V., "Generalized Wear Coefficients," from Tribology Data Handbook, CRC Press, Ed. E. R. Booser, Boca Raton, pp. 455-461 (1997).

115. Tomozawa, M., "Water in Glass," *J. of Non-Cryst. Solids.*, **73**, pp. 197-204 (1985).

116. Machenzie, K. J. D., Brown, I. W. M., Ranchod, P., and Meinhold, R. H., "Silicate Bonding of Inorganic Materials, Part I – Chemical Reactions in Sodium Silicate at Room Temperature," *J. of Mater. Sci.*, **26**, pp. 763-768 (1991).

117. Machenzie, K. J. D., Brown, I. W. M., and Ranchod, P., "Silicate Bonding of Inorganic Materials, Part II – Reactions at High Temperatures," *J. of Mater. Sci.*, **26**, pp. 769-775 (1991).

118. Wills, J. H., "Silicon Compounds, Synthetic Inorganic Silicates," in ECT 2nd Ed., Vol. 18, pp. 134-165.

119. Tripp, W. C. and Graham, H. C., "Oxidation of Si_3N_4 in the Range 1300 to $1500°C$," *J. Am. Ceram. Soc.*, **59** (9/10), pp. 399-403 (1976).

120. Singhal, S. C., "Thermodynamics and Kinetics of Oxidation of Hot-Pressed Silicon Nitride," *J. Mater. Sci.*, **11**, pp. 500-509 (1976).

121. Cubicciotti, D., Lau, K. H., and Jones, R. L., "The Rate Controlling Process in the Oxidation of Hot-Pressed Silicon Nitride," *J. Electrochem. Soc., Acel. Bf. Comm.*, pp. 1955-1956 (1977).

122. Cubicciotti, D. and Lau, K. H., "Kinetics of Oxidation of Hot-Pressed Silicon Nitride Containing Magnesia," *J. Am. Ceram. Soc.*, **61** (11/12), pp. 512-517 (1978).

123. John, P. J. and Zabinsky, J. S., "Sulfate Based Coatings for Use as High-Temperature Lubricants," *Trib. Ltrs.*, **7**, pp. 31-37 (1999).

124. Sutor, P. A., "High Temperature Lubricant Characterization," WRDC-TR-90-2069 (1990).

125. Turkdogan, E. T. and Bills, P. M., "A Critical Review of Viscosity of CaO-MgO-Al_2O_3-SiO_2 Melts," *Ceram. Bull.*, **39** (11), pp. 682-687 (1960).

126. Poole, J. P., "Low-Temperature Viscosity of Alkali Silicate Glasses," *J. Am. Ceram. Soc.*, **32** (7), pp. 230-233 (1949).

127. Jacobson, N. S., "Sodium Sulfate: Deposition and Dissolution of Silica," *Oxid. Metals*, **31**(1/2), pp. 91-103 (1989).

128. Blachere, J. R. and Pettit, F. S., High Temperature Corrosion of Ceramics, Noyes Data Corp., Park Ridge (1989).

129. Fischer, T. E. and Sexton, M. D., "The Tribochemistry of Oxidative Wear," in Physical Chemistry of the Solid State: Applications to Metals and their Compounds, Elsevier, Ed. P. Lacombe, Amsterdam, pp. 97-108 (1984).

130. Uchino, T., Sakka, T., Ogata, Y., and Iwasaki, M., "Mechanism of Hydration of Sodium Silicate Glass in a Steam Environment: ^{29}Si NMR and ab Initio Molecular Orbital Studies," *J. Phys. Chem.*, **96**, pp. 7308-7315 (1992).

APPENDIX A

INITIAL MATERIAL CHARACTERIZATION

This appendix provides background on the synthesis and crystal structure of cesium oxythiotungstate (Cs_2WOS_3). The chemical composition and structural chemistry of the starting Cs_2WOS_3 material subsequently used in thermal analysis and friction and wear experiments are also examined here. Chemical composition was determined by ion chromatography, EDS, and XPS. XRPD, FTIR, and Raman spectroscopy were used as qualitative tools to study the chemical and molecular structure.

A1. Background

Cs_2WOS_3 has a well-defined crystal structure that's similar to other thio- and seleno salts of the molybdates and tungstates of the potassium sulfate- (β-K_2SO_4) type structure [20-22, 131, 132]. The trithiotungstate (WOS_3^{2-}) ion is simply a tungstate ion in which three of the oxygen atoms have been replaced with sulfur. This is shown schematically in Figure A-1a. The resulting molecular structure, shown in Figure A-1b, consists of a central tungsten cation that is bonded to three sulfur and one oxygen, forming a distorted tetrahedra. The cesium cations are, in turn, ionically bound to the $[WOS_3]^{2-}$ anion to balance the oxygen and sulfur negative charges.

The crystal structure of Cs_2WOS_3 has been well characterized by x-ray diffraction [131] and Raman and infrared spectroscopy [131, 133]. Cs_2WOS_3 crystallizes orthorhombically with lattice constants a = 9.78, b = 7.26, c = 12.22 with Z = 4 formula units per unit cell in the spatial group P_{nma} (D_{2h}) [131]. An approximate three-dimensional representation of the crystal lattice and Bravais unit cell are shown in Figures A-2 and A-3, respectively. The crystal model was generated with XTAL-3D software [134].

A2. Material Synthesis and Characterization

A2.1 Synthesis Procedure

For the present study, Cs_2WOS_3 was synthesized by Desilube Technology, Inc. using a procedure slightly different from that described by Müller et al. [21, 131]. The reaction is shown below:

$$Na_2WO_4 \cdot 2H_2O + 2CH_3CO_2Cs + 3H_2S \longrightarrow Cs_2WOS_3 + 5H_2O + 2CH_3CO_2Na$$
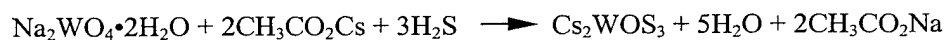
The procedure involved mixing 150 ml of distilled water (H_2O) with 88.3 g of cesium acetate (CH_3CO_2Cs) in a 800-ml beaker. After solution, 66.0 g of sodium

110

$$O = W = O$$

with O^- above and O^- below the central W

tungstate $[WO_4]^{2-}$ ion

$$S = W = S$$

with O^- above and S^- below the central W

trithiotungstate $[WOS_3]^{2-}$ ion

(a)

Cs
S
O
W
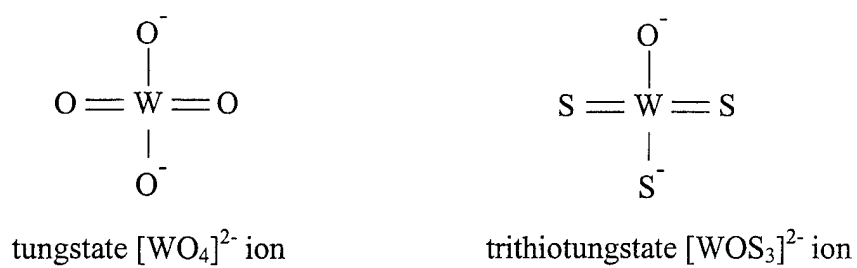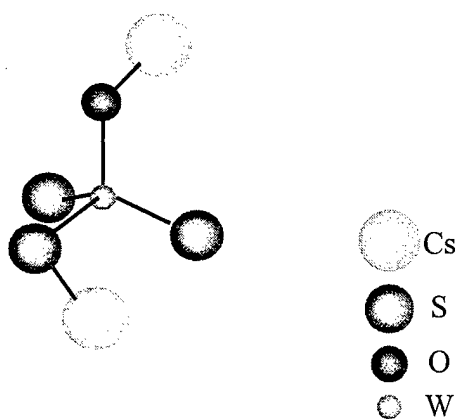
(b)

Figure A-1. Molecular Structure of Cs_2WOS_3

Figure A-2. Crystal Structure of Cs_2WOS_3
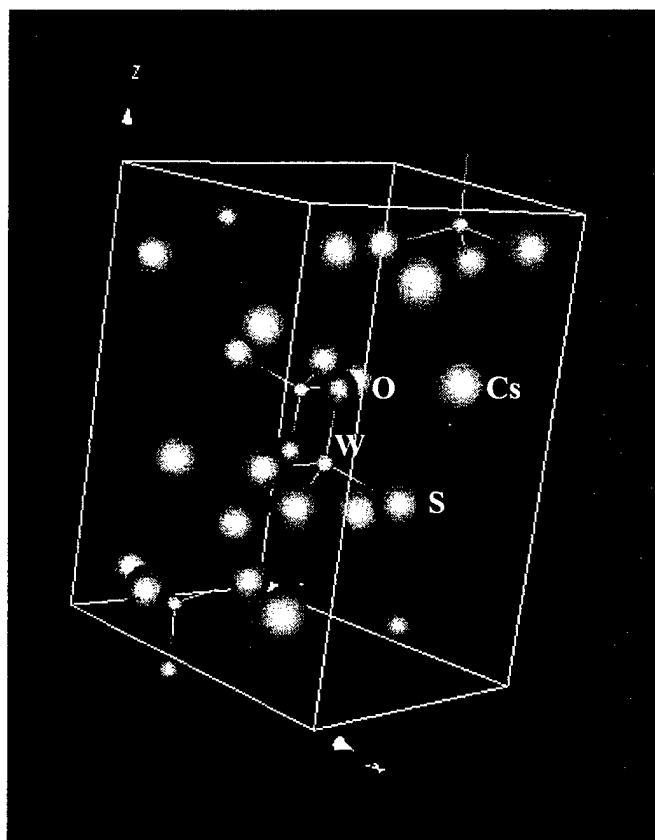
Figure A-3. Bravais Unit Cell of Cs_2WOS_3

tungstate hydrate ($Na_2WO_4 \cdot 2H_2O$) was added and rinsed in with 150 ml of concentrated ammonium hydroxide. Glacial acetic acid was then added dropwise from an addition funnel until $pH = 10$ (pH meter). The white milky slurry was transferred to a 1-liter reaction flask equipped with a hydrogen sulfide (H_2S) sparger, a stirring bar, a thermometer, a pH meter electrode and a gas outlet. H_2S gas (65.0 g) was bubbled through the slurry, which changed from white to yellow. The pH changed from 10 to about 8 during H_2S addition. Temperature was ambient. The reaction flask was cooled to about 10°C and the yellow slurry was filtered and washed sequentially with 50 ml portions of cold ethanol and two times with 100 ml portions of diethyl ether. The yellow cake was dried overnight at 100°C. Yield was 84 percent. A portion of the dried powder was ball milled in toluene for 24 hours, filtered, air dried for 12 hours and oven dried at 110°C for 2 hours. This resulted in a fine powder that was subsequently used for thermal analysis experiments and bonded coatings for friction and wear testing. The ball-milled and as-prepared powder samples were stored in plastic containers.

A2.2 Chemical Analysis

EDS results for the as-prepared and ball-milled Cs_2WOS_3 powders are given in Table A-1. The theoretical stoichiometric values are also shown. The approximate surface composition determined by XPS is given in Table A-2. The XPS survey scan is shown in Figure A-4. Because of the difference in sampling depths between EDS and XPS, the results of each did not always agree. EDS probes to a depth of about 1.0 μm and is less sensitive to light elements. XPS, on the other hand, probes to a depth of only about 5 nm an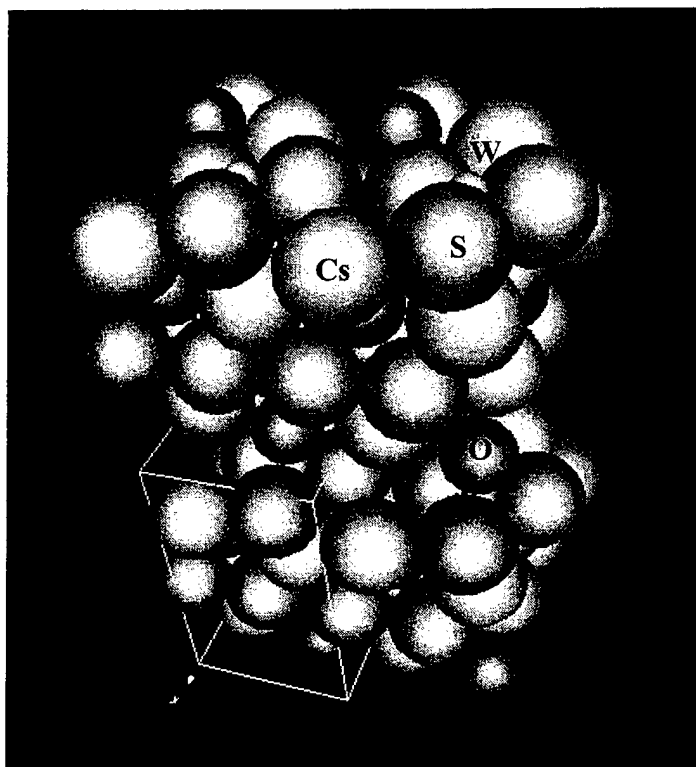d, therefore, is very surface sensitive. Hence, discrepancies are likely associated with the depth distribution of elements. Despite these differences, results were generally consistent with one another.

There was a relatively high carbon (hydrocarbon) background in XPS that is probably due, for the most part, to the adhesive tape. The contribution of carbon to the composition was neglected. Both EDS and XPS indicate that the surface oxygen level is much higher and the sulfur surface level much lower than expected for a stoichiometric compound. XPS also found that sulfur is multivalent on the surface with both sulfate (S-O) and sulfide (S-M) being detected. Tungsten levels were also low in EDS but XPS showed values closer to theoretical for this particular element.

The surface cesium level was low in all cases. Conversely, the overall (bulk) cesium concentration determined by ion chromatography was 44.2 wt.%, which is close to the theoretical value of 47.3 wt.%. These results indicate that the surface of the Cs_2WOS_3 powder has partly oxidized, probably to Cs_2SO_4 and/or Cs_2WO_4. Interestingly, the chemical composition appeared to change slightly after ball milling. As shown in Tables A-1 and A-2, a slight decrease in sulfur level was detected by both EDS and XPS. The decrease was observed specifically in S-O type species by XPS. It is likely that volatile SO_2 type species may have been driven off during the 110°C heating performed after ball milling.

Table A-1. Approximate Chemical Composition of Cs_2WOS_3 As Determined by Semiquantitative EDS				
Sample	Atomic %			
	Cs	O	S	W
as-prepared	12.9	67.0	15.5	4.7
ball milled	13.2	66.8	12.3	7.8
theoretical values	*28.6*	*14.3*	*42.9*	*14.3*

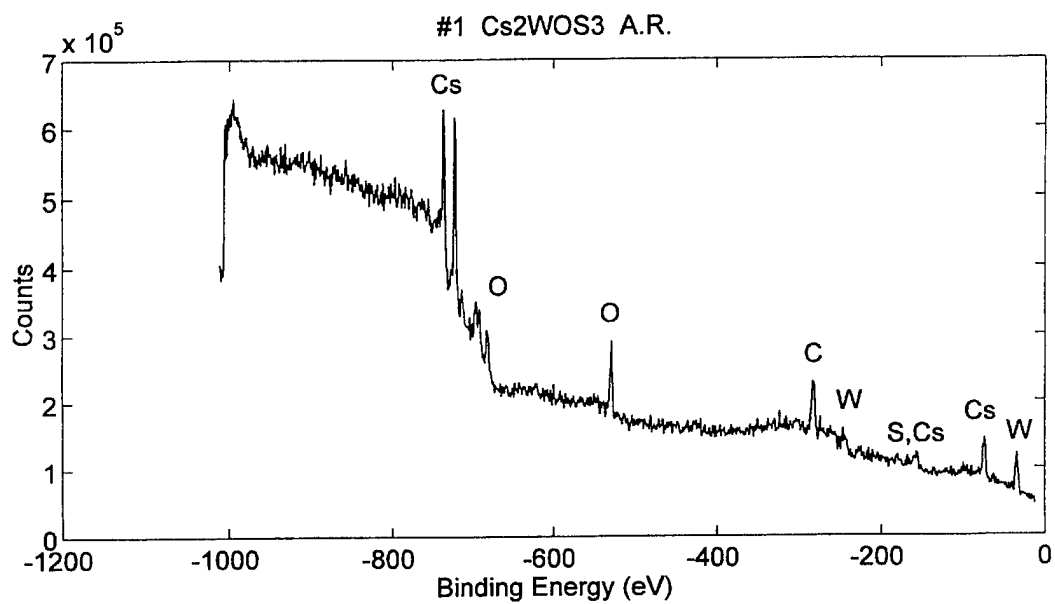| Table A-2. Approximate Atomic Percent Surface Composition of Cs_2WOS_3 As Determined by XPS*					
Sample	Atomic %				
	Cs	O	S		W
			S-O	S-M	
as-prepared	19.5	48.7	12.9	5.9	12.9
ball milled	13.7	58.0	5.6	8.2	14.5

* Contribution of carbon not included.

Figure A-4. XPS Spectrum of As-prepared Cs_2WOS_3

A2.3 Chemical and Molecular Structure

XRPD was used to characterize the crystalline phases present in the as-prepared Cs_2WOS_3 powder. The XRPD pattern obtained on the as-prepared sample is shown in Figure A-5a. The JADE PDF standard pattern is also shown for comparison. All of the peaks reported in the standard were present in the measured pattern, though some showed a slight shift to lower 2θ values. The measured relative intensities resembled those of the standard with the exception of the 29.17 (d=3.0597) and 37.93° (d=2.3756) peaks. These were significantly more intense in the measured pattern. Also, there were six additional peaks in the measured pattern from an unknown second crystalline phase.

FTIR and Raman spectroscopy were used to characterize the molecular structure of the Cs_2WOS_3 starting material. The $[WOS_3]^{2-}$ anion of the Cs_2WOS_3 molecule participates as a whole in infrared vibrations and thus, could be treated as an independent structural component. The anion could be regarded as a XY_4 type molecule where one of the Y atoms has been replaced with a Z atom resulting in a tetrahedral ZXY_3 type molecule of approximate C_{3v} symmetry [135]. The lowering of symmetry (from T_d to C_{3v}) splits the doubly and triply degenerate vibrations (i.e., E and F species) and activates IR inactive vibrations. This results in six fundamental vibrational frequencies, which are all IR and Raman active.

Figures A-6 and A-7 show the Raman and IR spectra respectively, acquired on the as-prepared Cs_2WOS_3 powder. Major band frequencies and assignments are given in Table A-3 together with those obtained from the literature. At least eight distinct bands were observed in Raman, and two strong bands with several weak absorptions were noted in IR. Both spectra indicate the Cs_2WOS_3 material is quite pure. With the exception of the weak low frequency band observed at 93 cm^{-1}, all of the bands observed in Raman agree with those reported in the literature. The weak absorptions noted at about 93, 114 and 214 cm^{-1} do not appear to be combination or overtone bands and are believed to be associated with the presence of elemental sulfur ($S_\infty + S_8$) [52, 136]. Thermal decomposition mass spectrometry, discussed in the Appendix B, confirmed that elemental sulfur is released when Cs_2WOS_3 is heated above 150°C.

In IR, two sharp prominent bands were observed at 868 and 450 cm^{-1}. These correlate well with W-O and W-S stretching modes of $[WOS_3]^{2-}$, respectively [131]. Several weak absorptions were also noted at 3383, 1732, 1640, 1121, 993, and 658 cm^{-1}. None of these were observed in Raman. The broad weak peaks at 3383 and 1640 cm^{-1} are in good agreement with O-H stretching and bending modes, respectively of lattice water [137], indicating the presence of adsorbed moisture in the Cs_2WOS_3 powder. The 1732 cm^{-1} band is probably an overtone of the 868 cm^{-1} absorption while the 1121, 993, and 658 cm^{-1} bands correlate with S-O stretching and SO_4 bending modes in sulfate- $[SO_4]^{2-}$ type structures [138, 139]. The very weak intensities of these bands suggest that SO_4^{2-}-type species, probably Cs_2SO_4, are present in minor quantities. This was confirmed by ion chromatography, which found that the Cs_2WOS_3 material contained 800 ppm of the sulfate ion. A weak shoulder near the 868 cm^{-1} band, at about 845 cm^{-1}, was also present
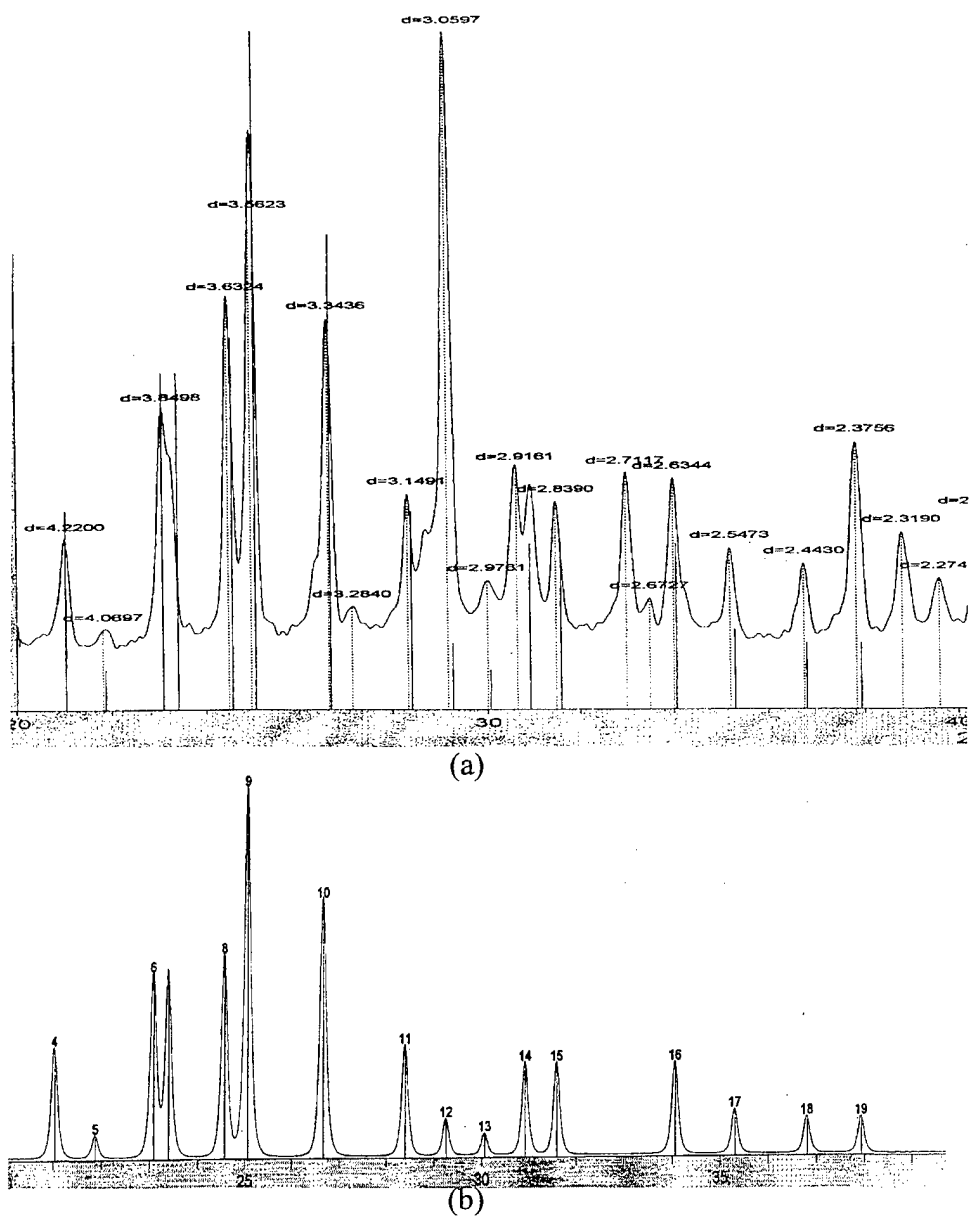
Figure A-5. XRPD Pattern of (a) As-prepared Cs_2WOS_3 and (b) Standard Pattern
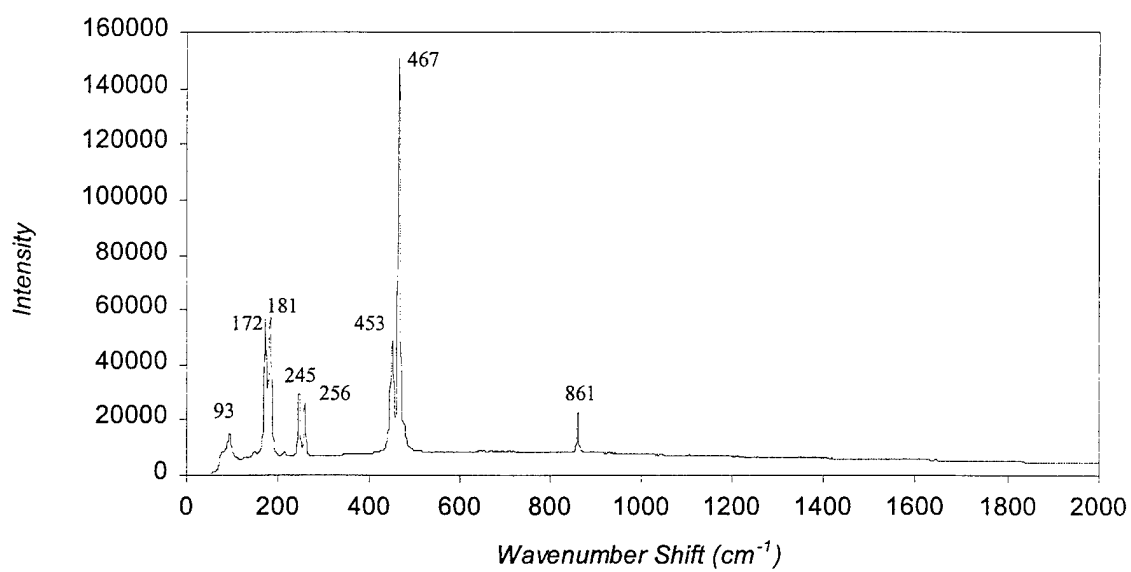
Figure A-6.   Raman Spectrum of As-prepared Cs_2WOS_3
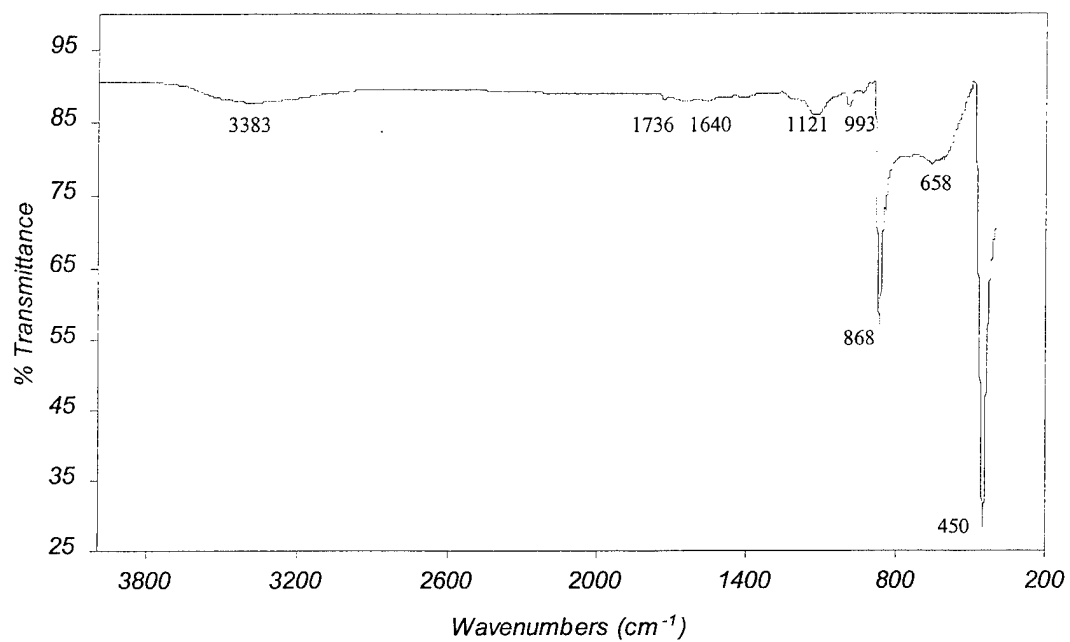
Figure A-7. FTIR Spectrum of As-prepared Cs_2WOS_3

| Table A-3. Raman and Infrared Vibrational Frequencies of Cs_2WOS_3 ||||||
Frequency (cm^{-1})				Assignment	Species
Raman	IR	Raman Ref. [131, 133]	IR Ref. [131, 133]		
	3383 w, bd			O-H stretch	
	1732 vw			$2 \times 868 = 1736$	
	1640 vw			OH bend	
	1121 w			S-O stretch (sulfate)	
	993 w			S-O stretch (sulfate)	
861 m	868 s, sh	867	872	ν(WO) stretch	$\nu_1(A_1)$
	845 w		845	ν(WO) stretch ?	
	658 w, bd			SO_4 bend (sulfate)	
467 vs		473	473	ν_s(WS) stretch	$\nu_2(A_1)$
453 s	450 vs, sh	459	457	ν_{as}(WS) stretch	$\nu_4(E)$
256 m		263	263	ρ_r (WS_3)	$\nu_5(E)$
245 m		250	252	ρ_r (WS_3)	$\nu_5(E)$
214 vw				$S_\infty + S_8$	
181 s		187	192	δ_s (WS_3) bend	$\nu_3(A_1)$
			186	δ_{as} (WS_3) bend	$\nu_6(E)$
172 s		176	175	δ_{as} (WS_3) bend	$\nu_6(E)$
147 vw				$S_\infty + S_8$	
93 w				$S_\infty + S_8$ or lattice mode?	

vs = very strong; s = strong; m = medium; w = weak; vw = very weak
sh = sharp; bd = broad

in IR. Interestingly, this shoulder also appears in IR spectra reported in the literature for other alkali metal thiotungstates, including Cs_2WOS_3, and appears to be associated with the W-O stretching mode [133].

A3. Summary

The crystal and molecular structure of Cs_2WOS_3 were reviewed, and the Cs_2WOS_3 starting material synthesized for this study was characterized by various analytical techniques. EDS and XPS chemical analysis showed that the surface of the synthesized Cs_2WOS_3 powder contained less sulfur and more oxygen than expected for a fully stoichiometric compound, suggesting that the as-prepared powder was partially oxidized, probably to Cs_2SO_4. This was confirmed by FTIR analysis, which detected the presence of sulfate-type (SO_4^{2-}) species. The amount of SO_4^{2-} ions was determined to be about 800 ppm by ion chromatography. Elemental sulfur and water were also detected by Raman and FTIR analysis. Despite the presence of these minor impurities, XRD, FTIR, and Raman analysis all showed a well-defined crystalline structure and all confirmed the presence of the $[WOS_3]^{2-}$ anion. Results were consistent with that reported in the literature for Cs_2WOS_3.

A4. APPENDIX A REFERENCES

131. Müller, A., Diemann, E. and Heidborn, U., "Darstellung, Eigenschaften, IR-Spektren und rontgenographische Untersuchungen von Trithiomolybdaten und –wolframaten," *Z. Anorg. allgem. Chem.*, **371**, p. 136 (1969).

132. Krebs, B., Müller, A., and Kindler, E., "Kristallstruktur von Cs_2MoOS_3," *Z. Naturforsch.*, **25b**, p. 222 (1970).

133. Müller, A., Weinstock, N., and Schulze, H., "Laser-Raman-Spektren der Ionen MoS_4^{2-}, WS_4^{2-}, $MoOS_3^{2-}$, and WOS_3^{2-} in wässriger Lösung sowie der entsprechenden kristallinen Alkalisalze," *Spectrochim. Acta*, **28A**, pp. 1075-1082 (1972).

134. Hewat, A. W., xtal-3D Internet software.

135. Nakamoto, K., Infrared and Raman Spectra of Inorganic and Coordination Compounds, 3rd Ed., John Wiley & Sons, New York, pp. 132-147 (1978).

136. Strauss, H. L. and Greenhouse, J. A., "Vibrational Spectra of Elemental Sulfur," in Elemental Sulfur, Interscience Publ., New York, Ed. Meyer, B., pp. 241-249 (1965).

137. Nakamoto, K., Infrared and Raman Spectra of Inorganic and Coordination Compounds, 4th Ed., John Wiley & Sons, New York, pp. 228 (1986).

138. Colthup, N.B., Daly, L.H., and Wilberley, S.E., Introduction to Infrared and Raman Spectroscopy, 3rd Ed., Academic Press, Boston, pp. 375-376 (1990).

139. Nakamoto, K., Infrared and Raman Spectra of Inorganic and Coordination Compounds, 4th Ed., John Wiley & Sons, New York, pp. 477 (1986).

APPENDIX B

THERMAL ANALYSIS

The objective of this part of the study was to investigate the thermal characteristics of Cs_2WOS_3, both with and without a sodium silicate glass encapsulate, and silicon nitride powders and mixtures of these. Most of the thermal analysis was performed using TGA. High-temperature differential thermal analysis (HT-DTA) and TDMS were used to a lesser extent to further study oxidational characteristics and to analyze the gases evolved from Cs_2WOS_3 as a function of temperature. Changes in the chemical composition and structure of annealed Cs_2WOS_3 powders were studied by XPS, laser-Raman and FTIR spectroscopy. The results obtained under the static conditions studied here provide some insight into possible interactions that may occur under high-temperature, dynamic tribo-conditions.

B1. Experimental

B1.1 Starting Materials

The Cs_2WOS_3 powder described in the Appendix A was used for thermal analysis. Since the Cs_2WOS_3 bonded lubricant coatings used in this study contained sodium silicate as a binder, it was necessary to investigate the effect of the binder on the thermal behavior of Cs_2WOS_3 and Si_3N_4 mixtures. This was accomplished by spraying Cs_2WOS_3 / $Na_2O\cdot3SiO_2$ bonded films on glass slides, discussed in detail in Section 2, and carefully scraping off the coating with a razor blade. The scraped coating was then ball milled into a fine powder and either analyzed in neat form or mixed with Si_3N_4 powder. Three $Cs_2WOS_3/Na_2O\cdot3SiO_2$ (pigment-to-binder) weight ratios were investigated; 1:1, 1:1.6, and 1:2. The sodium silicate used for this procedure was provided by The PQ Corporation and consisted of an aqueous solution containing 43.18% amorphous $Na_2O\cdot2.88SiO_2$ solids.

The atomic percent of each of the lubricant-to-binder compositions was determined by semiquantitative EDS and XPS and are listed in Table B-1 together with theoretical values. XPS and EDS results differed substantially in terms of sodium and silicon levels. XPS showed a higher percentage of sodium and significantly lower silicon than expected while EDS showed values closer to theoretical. This suggests that a thin layer enriched with sodium had formed on the surface of these mixtures. It is believed that the sodium-rich layer is caused by the reaction with ambient water vapor. All alkali silicate glasses, in general, will rapidly develop surface compositional gradients when exposed to water vapor [140, 141]. The ion exchange process that occurs causes alkali ion migration toward the surface forming an alkali-rich weathered reaction layer, presumably a hydrated alkali salt [140, 141]. If liquid water were present instead, the alkali-rich layer would dissolve and a SiO_2-rich layer would be left behind, similar to

Table B-1. Approximate Atomic Percent of Cs_2WOS_3 / $Na_2O\cdot3SiO_2$ Blends As Determined by XPS* and EDS							
Cs_2WOS_3/$Na_2O\cdot3SiO_2$ Weight Ratio	Atomic %						
	O	Cs	Na	S		W	Si
				S-O	S$^=$		
XPS							
1:1	57.2	2.1	28.0	2.9	4.0	1.7	4.0
1:1.6	55.8	2.1	30.3	3.1	2.8	1.6	2.8
1:2	55.7	1.5	33.6	2.5	2.9	0.8	3.1
EDS							
1:1	60.0	4.5	13.3	4.1		2.8	15.3
1:1.6	58.2	3.3	17.0	2.6		2.3	16.4
1:2	58.6	2.7	16.5	3.4		1.4	17.4
theoretical values							
1:1	*49.4*	*5.8*	*13.2*	*8.6*		*2.9*	*20.1*
1:1.6	*52.3*	*3.9*	*14.4*	*5.9*		*1.9*	*21.6*
1:2	*53.4*	*3.2*	*14.8*	*4.8*		*1.6*	*22.2*

* Contribution of carbon (hydrocarbon) not included.

alkali leaching typically observed in glass. XPS also showed that sulfur was multivalent with oxidized, perhaps as sulfate, and metal sulfide species being detected. The increase in sodium and decrease in cesium and tungsten levels were in fair agreement with the expected changes for the three compositions though.

Mixtures of Cs_2WOS_3 (with and without the silicate binder) and Si_3N_4 were obtained by blending 25.0 mg each in small vials. Mixing was performed by shaking in an amalgamator for 1 minute. A research grade (99.9 percent) Si_3N_4 powder, purchased from DKK, was used for this analysis. The Si_3N_4 particle morphology is depicted in the SEM micrograph shown in Figure B-1. The as-received powder mainly consists of small clusters made up of submicron size spherical particles less than 0.5 μm in diameter. The specific surface area, as measured by the BET (Brunauer-Emmett-Teller) nitrogen adsorption method was 6.25 m^2/g.

XRPD showed α-Si_3N_4 (trigonal) as being the primary phase, though β-Si_3N_4 (hexagonal) phase was also detected. This is illustrated in Figure B-2, which shows the measured and standard α–Si_3N_4 patterns [142]. The amount of β-Si_3N_4 was determined to be less than 10 wt%. Qualitative chemical analysis using x-ray fluorescence (XRF) detected iron and calcium as the main metallic impurities, while oxygen and carbon were detected as the major surface impurities by XPS.

B1.2 Thermal Analysis Equipment

TGA was conducted using a TA Instruments 2050 null-type thermobalance with a mass resolution of 0.2 μg and ±0.1 percent accuracy. A schematic of the instrument is illustrated in Figure B-3. TGA measures changes in mass of a material either as a function of temperature or isothermally as a function of time in a controlled atmosphere. For this study, powdered samples, nominally 10.0 mg, were placed in platinum pans and lightly tamped with a glass rod. Experiments were conducted under dynamic atmospheres (100 ml/min) in both laboratory air and bottled helium. Pressure at the sample was assumed to be atmospheric. Two heating rates were used for nonisothermal experiments, 1°C/min and 10°C/min. For isothermal experiments, samples were initially heated at a rate of 10°C/min to the temperature of interest and held isothermally for 16 hours.

HT-DTA was performed using a model 910 Dupont Instruments analyzer with an upper temperature limit of 1600°C and a ΔT sensitivity of about 6.3°C/cm. The temperature precision was ± 0.2°C. DTA measures temperature changes between the sample of interest and an inert reference as a function of temperature. For this study, peaks appearing at positive ordinate values are due to exothermic reactions while those appearing in negative are endothermic. Samples, 5.0 to 10.0 mg, were placed in platinum cups. Samples were lightly packed with a glass rod prior to heating. Alumina (Al_2O_3) or Si_3N_4 powder placed in Al_2O_3 or platinum cups were used as reference samples. Experiments were conducted in laboratory air flowing at 50 ml/min under atmospheric pressure conditions. Samples were heated to 1000°C at a rate of 10°C/min.
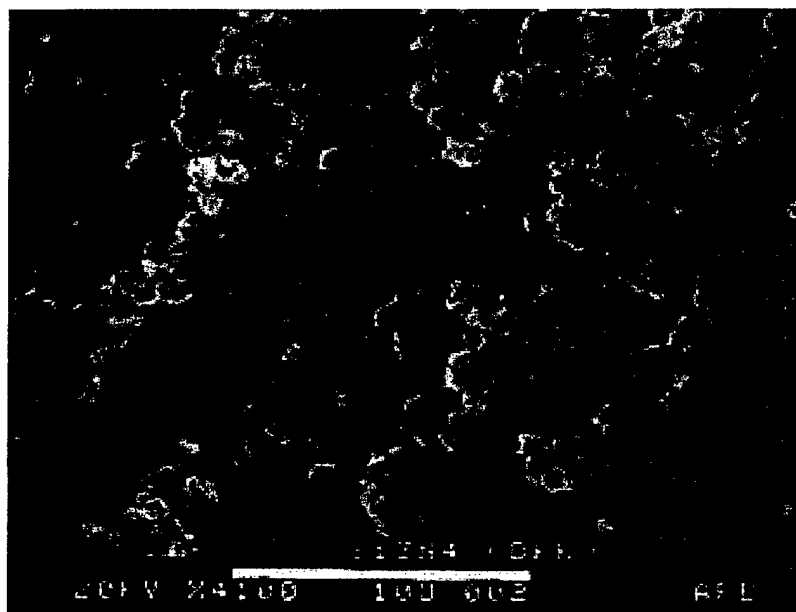
(a)
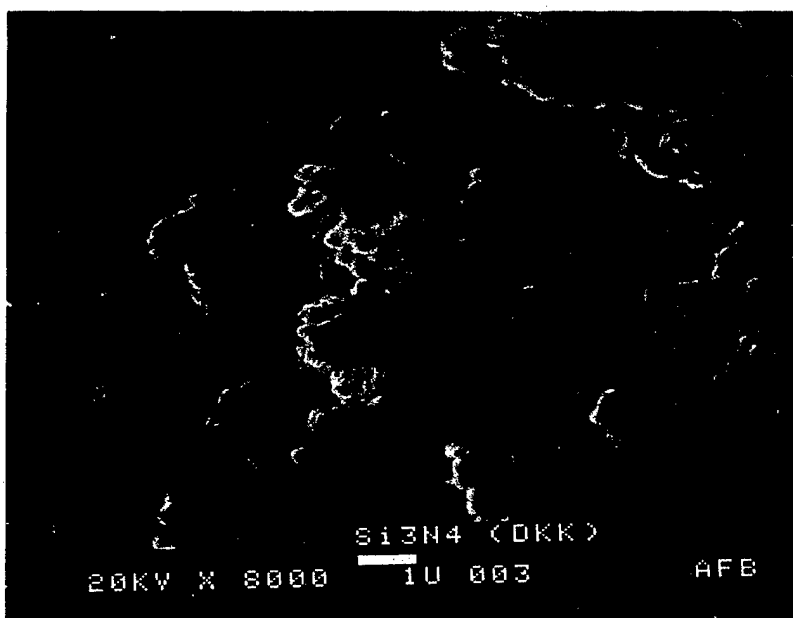
(b)

Figure B-1. SEM of As-received Si₃N₄ Powder: (a) 4100X and (b) 8000X

127
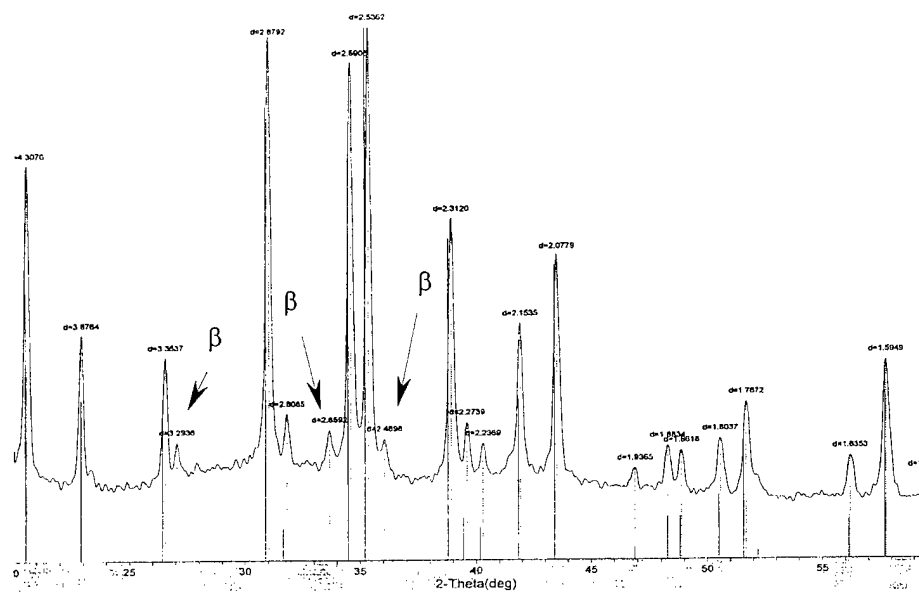
(a)
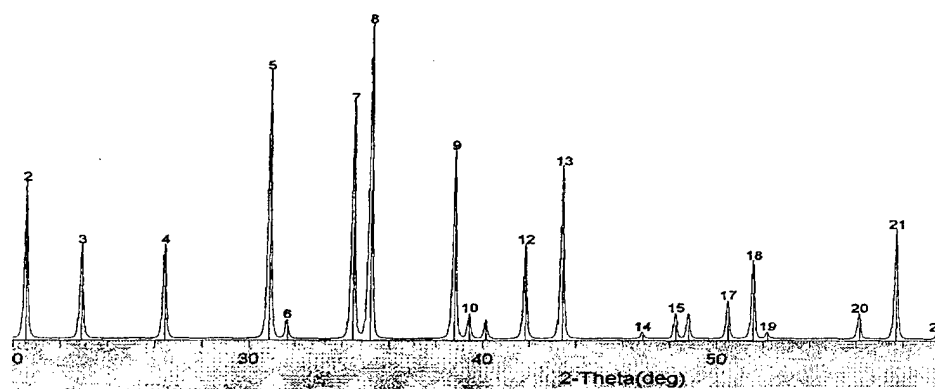
(b)

Figure B-2. XRPD Patterns of (a) DKK α-Si$_3$N$_4$ and (b) α-Si$_3$N$_4$ Standard

Null-type balance arm
  balance resolution: 0.2 μg
  accuracy: ± 0.1%

+

Reference pan

Water-cooled
furnace housing

Gas In

Gas Out

Platinum sample pan

Platinel II
thermocouple

Electric resistance
heater

Figure B-3. Null-type Thermobalance Used for TGA

TDMS was used to characterize the gases evolved from Cs_2WOS_3. The 8.5 mg of Cs_2WOS_3 powder was placed in an alumina coated tungsten heater basket and heated to temperatures above 600°C in a turbomolecular-pumped ultra-high vacuum system. The evolved gases were monitored using a UTI model 100C quadrupole mass spectrometer. The base pressure prior to the start of the analysis was less than 5×10^{-7} torr.

B1.3 Chemical Surface Analysis

XPS surface analysis was performed on four pyrolyzed Cs_2WOS_3 powdered samples that were heated in air using the DTA instrument. XPS was performed using an AEI ES-100 photoelectron spectrometer with a nonmonochromatic magnesium x-ray source (Mg K_α radiation, 1.25 keV) with a 1 μm thick beryllium window. The x-ray power was typically 120 W with an anode potential of 10 kV. The spectra were referenced with the position of the carbon 1s band of adventitious hydrocarbon at 285.0 eV. The base pressure of the spectrometer was typically 2×10^{-8} torr.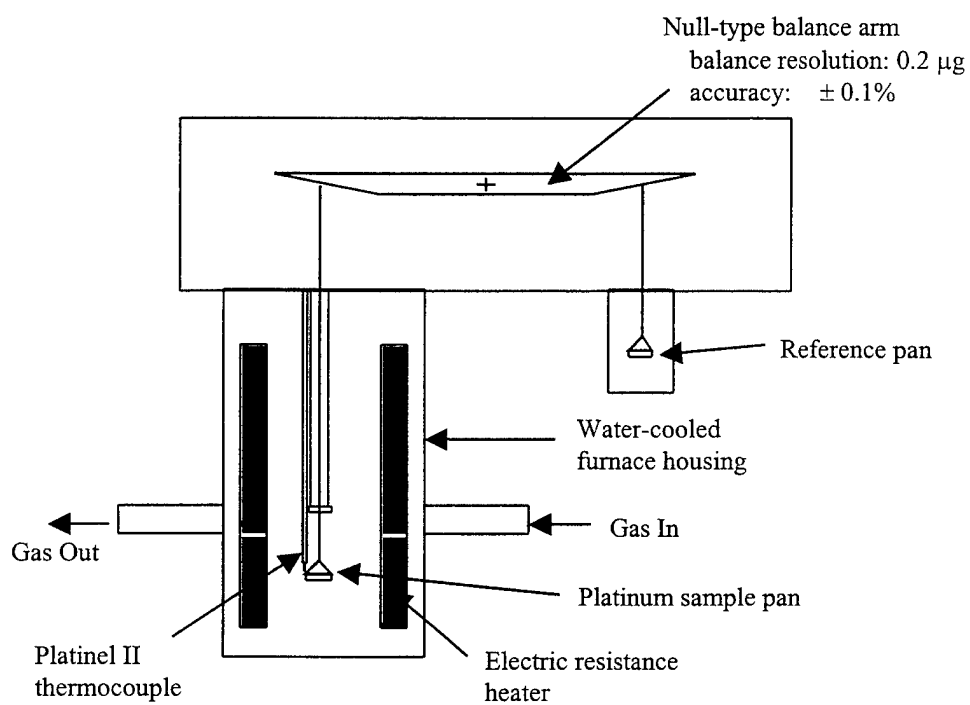 Samples were prepared by distributing a small amount of powder on adhesive tape so as to achieve a complete and uniform coverage.

FTIR and Raman spectra were acquired at room temperature on pyrolyzed Cs_2WOS_3 samples obtained from TGA and DTA experiments. The instrument characteristics and analysis parameters were previously described in Section 2.

B2. Results and Discussion

B2.1 TGA Results

The TGA thermogram showing the change in percent weight as function of temperature for neat Cs_2WOS_3 in air is portrayed in Figure B-4. As shown, Cs_2WOS_3 loses approximately 1.0 percent of its weight from initial heating to about 130°C. The weight loss is believed to be associated with the loss of elemental sulfur and adsorbed moisture. This is supported by TDMS and the Raman and FTIR results presented previously. In air, at least two distinct irreversible reactions are observed between 300°C and 600°C. A sharp oxidation reaction occurs at around 318°C with approximately 0.7 percent weight gain followed by a reaction that appears to initiate at about 380°C and gradually proceeds to about 440°C. The rate then accelerates between 440°C and 460°C leading to a maximum total weight gain of about 1.5 percent at about 600°C.

Since TGA only records net mass changes, it must be kept in mind that the weight gain shown is also being offset by loss of volatile sulfur species identified by TDMS. This will be shown later. The material appears to be thermally stable between 500°C and about 700°C above which the rate of weight loss accelerates leading to complete thermal decomposition.
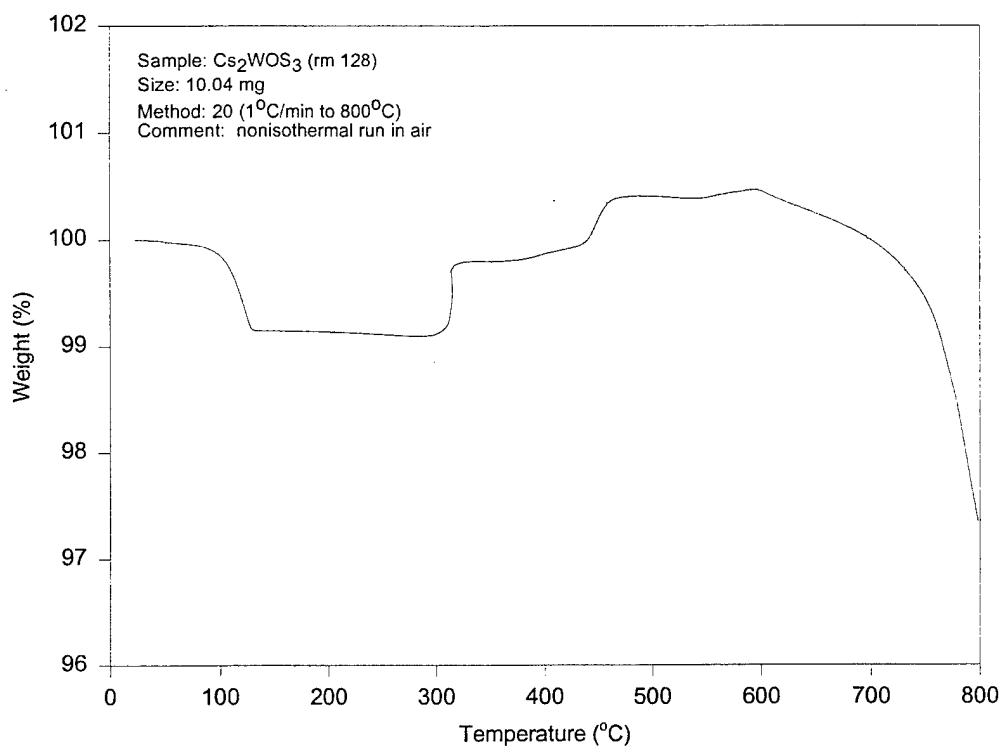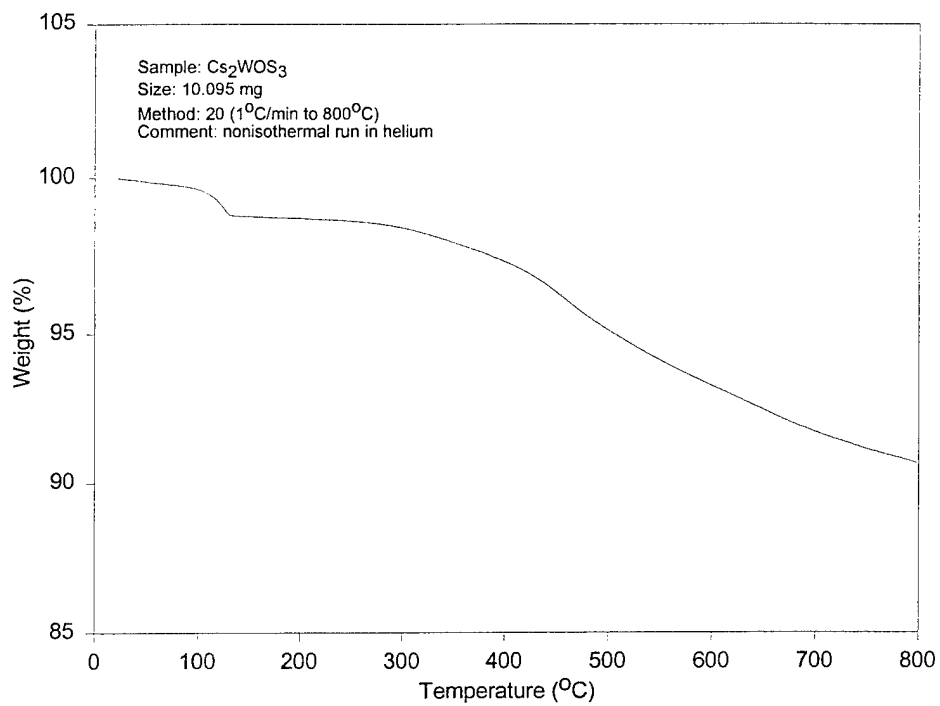
Figure B-4. TGA Thermogram of Neat Cs$_2$WOS$_3$ in Air

Figure B-5. TGA Thermogram of Cs_2WOS_3 in Helium

In helium, the initial 1 percent weight loss is also observed followed by a relatively stable behavior up to about 350°C. Unlike in air, the material undergoes thermal decomposition above 350°C, losing about 10 percent of its weight by 800°C. This is shown in Figure B-5. As expected, no weight gain is observed. The weight loss is likely due to loss of sulfur as the $[WOS_3]^{2-}$ anion is decomposed.

In terms of physical appearance in air, Cs_2WOS_3 remains bright yellow up to its first oxidation reaction (318°C) after which it turns green. The decomposition products obtained at 440°C are a dull white/grayish color, while those obtained at 540°C are powdery snow white at RT. These all tend to absorb moisture when exposed to laboratory air. The residue obtained at 800°C is dull white and highly hygroscopic at RT. This is shown in Figure B-6 where significant weight loss, about 10 percent, is apparent when the products are reheated in air.

TGA results obtained in air on $Cs_2WOS_3/Na_2O\,3SiO_2$ mixtures at 1:1, 1:1.6, and 1:2 weight ratios are shown in Figure B-7. Results differ significantly from those obtained on neat Cs_2WOS_3. Unsurprisingly, features associated with the Cs_2WOS_3 constituent were more prominent in the mixture that contained less sodium silicate (1:1 wt. ratio). The 320°C oxidation reaction is clearly visible in this case. Still, the three mixtures show similar trends. The initial weight loss is believed to be due to loss of moisture from the sodium silicate binder, which is likely to be present as a hydrated silicate ($Na_2O\,2.88SiO_2\,nH_2O$). This is consistent with the observed trends shown in Figure B-7 where the 1:1 mixture showed the least amount of weight loss followed by the 1:1.6 and 1:2 mixtures. All three mixtures exhibited a slight weight gain above 400°C. Unlike neat Cs_2WOS_3, which rapidly begins to lose weight at temperatures above 700°C, mixtures containing sodium silicate remained thermally stable up to 1000°C. It appears that the silicate binder protects the Cs_2WOS_3 oxidation products from gross thermal decomposition, perhaps by serving as a glass encapsulate and thus hindering mass transport or by forming a more stable compound.

Figure B-8 depicts the thermograms obtained on neat Si_3N_4 and a Si_3N_4/Cs_2WOS_3 1:1 weight ratio mixture in air. As one would expect, Si_3N_4 remains relatively stable up to 1000°C with only a slight weight increase above 750°C (< 0.4 percent at 1000°C). This is in good agreement with the temperature at which Si_3N_4 begins to oxidize [143]. Note that the heating rate was 1°C/min, which corresponds to about 5 hours above 700°C. When Cs_2WOS_3 is mixed in, a striking feature develops in the 750 to 1000°C range. The ~7 percent weight gain is believed to be attributed to enhanced oxidation of the Si_3N_4 component which suggests that the Cs_2WOS_3 decomposition products accelerate Si_3N_4 oxidation. This is supported by the Si KLL Auger spectra shown in Figure B-9 from a previous study that shows that Cs_2WOS_3 (or its decomposition products) accelerates the formation of SiO_2 on Si_3N_4 powder when heated to 700°C in air. Interestingly, the TGA feature occurs in the same temperature range where neat-Si_3N_4 begins to oxidize and, as will be shown later, the Cs_2WOS_3 decomposition products begin to melt.
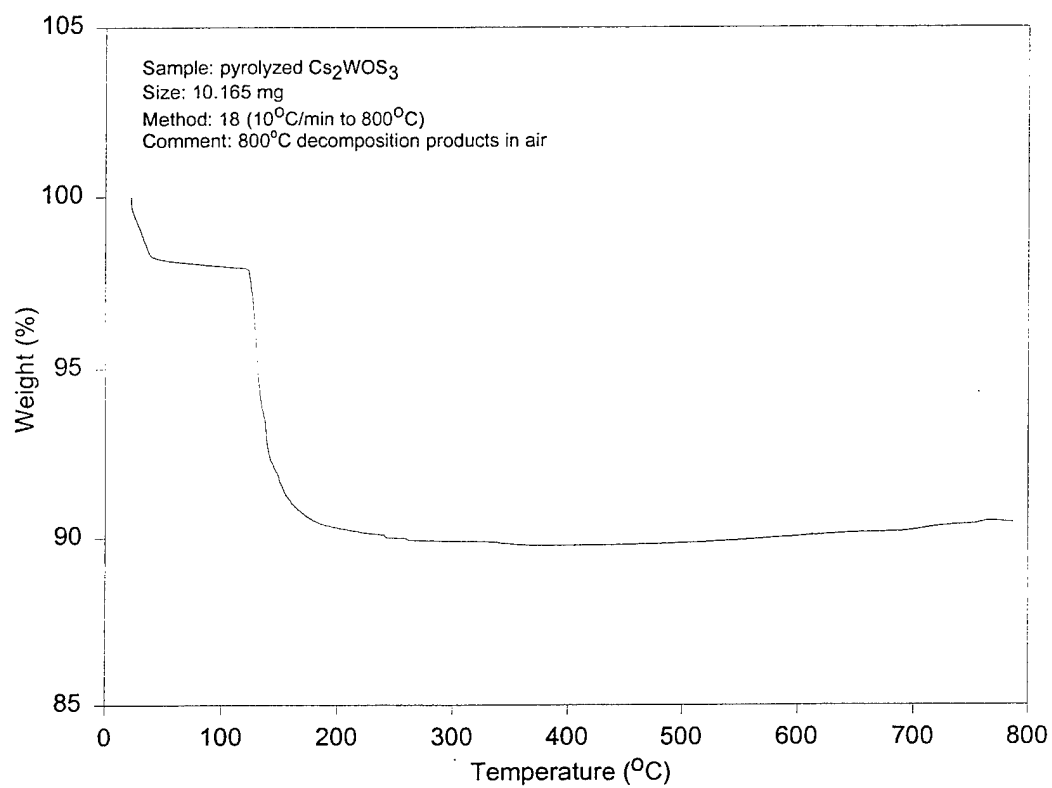
Figure B-6. TGA Thermogram of Cs_2WOS_3 800°C Decomposition Products in Air
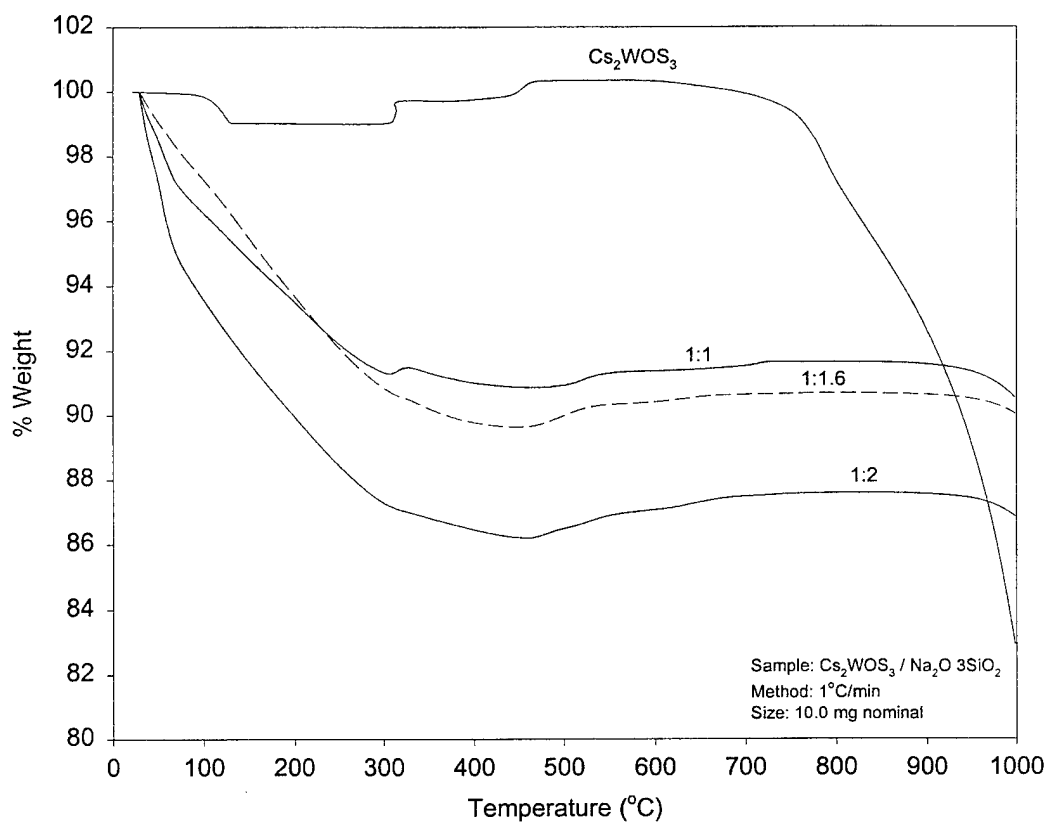
Figure B-7. TGA Thermograms of $Cs_2WOS_3/Na_2O\ 3SiO_2$ Mixtures in Air; 1:1, 1:1.6, and 1:2 Pigment-to-Binder Weight Ratios

135

The chart contains the following embedded text:

107

Sample: Si_3N_4, Si_3N_4 + Cs_2WOS_3
Size: 10.0 mg nominal
Method: 1°C/min to 1000°C
Comment: run in air, Pt pan

106

105

104

% Weight

103

Si_3N_4 + Cs_2WOS_3

102

101

Si_3N_4

100

99

0   100   200   300   400   500   600   700   800   900   1000

Temperature (°C)
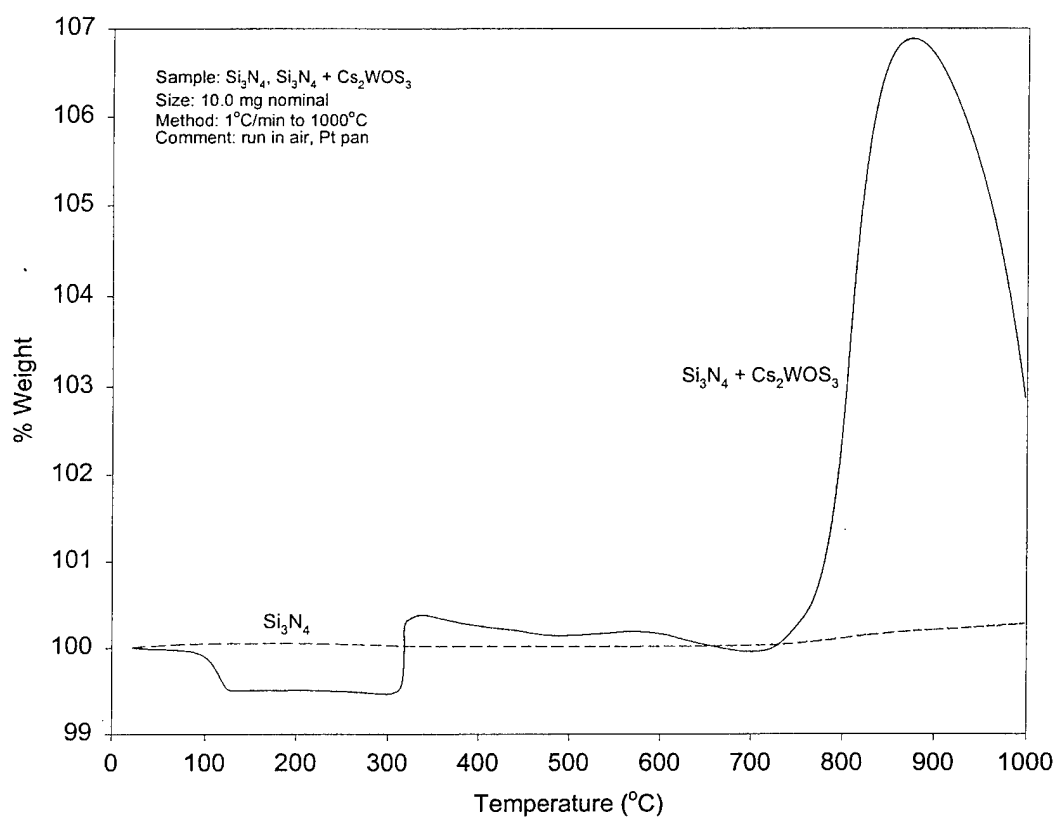
Figure B-8. TGA Thermograms of Neat Si_3N_4 and Si_3N_4/Cs_2WOS_3 1:1 Weight Ratio Mixture in Air

136
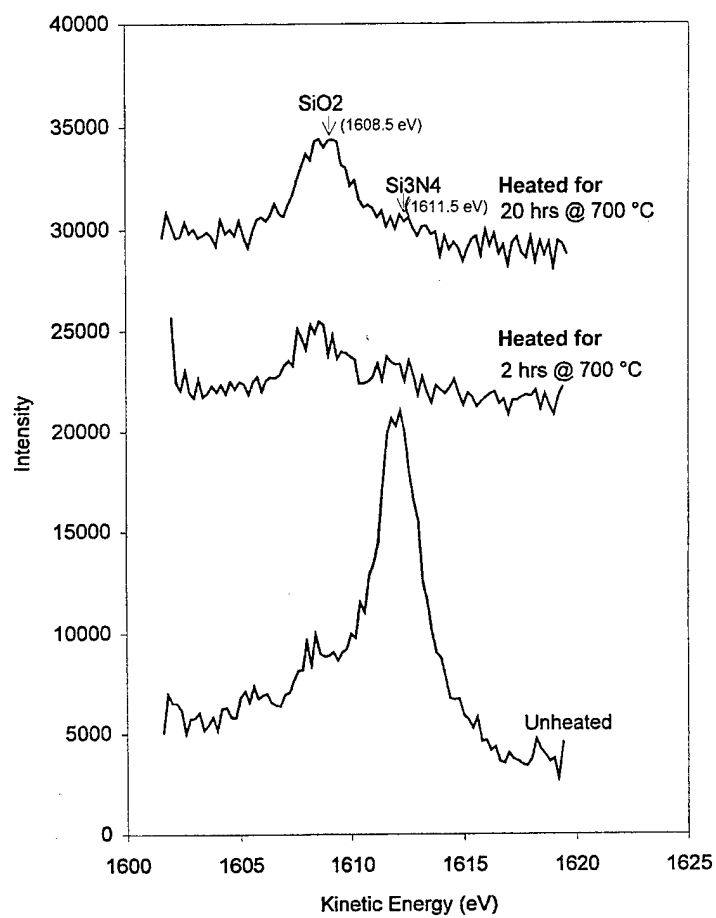
Figure B-9. Si KLL AES Spectra of Unheated and Heated Cs_2WOS_3/Si_3N_4 Powder Mixtures (from Rosado et al., *Trib. Trans.* **43**(3), p. 521, 2000)

To rule out the possibility of a catalytic effect with the Pt pan sample holder, experiments were performed on Si_3N_4 sample support wafers. Results were basically identical to that shown in Figure B-8. The rapid weight loss observed above 900°C in all of these experiments is probably due to unreacted Cs_2WOS_3 oxidation products undergoing gross thermal decomposition.

Isothermal TGA was conducted in air on neat powders and mixtures to further study oxidation characteristics and to try to determine the lowest temperature at which Cs_2WOS_3 decomposition products begin to have a noticeable effect on Si_3N_4 oxidation. Figure B-10 shows the isothermal oxidation behavior of neat-Si_3N_4 at 650, 750, 850, and 950°C. The material exhibits oxidation characteristics typical of other Si_3N_4 powders tested under similar conditions [143, 144]. The maximum weight gain was about 0.45 percent at 950°C. Figure B-11 shows the isothermal characteristics of the Si_3N_4/Cs_2WOS_3 mixtures in the same temperature range. The results show that the Cs_2WOS_3 decomposition products begin to have a measurable effect on Si_3N_4 oxidation at a temperature above 700°C. There appeared to be no measurable effect at 650 and 700°C. The weight gain was about an order of magnitude higher than with neat-Si_3N_4 from 750 to 950°C and the rate of weight gain increased with temperature.

The addition of the sodium silicate binder significantly affected the thermal characteristics of Si_3N_4-Cs_2WOS_3 mixtures as shown in Figure B-12. The mixtures containing the silicate showed measurable weight gain at 650°C, a temperature 100°C lower than the mixture without the binder. Interestingly, weight gain increased with decreasing sodium silicate content (pigment-to-binder ratio), as shown in this figure. These results suggests a chemical interaction between the binder, Cs_2WOS_3, and Si_3N_4, since the binder alone does not show any thermal activity at 650°C.
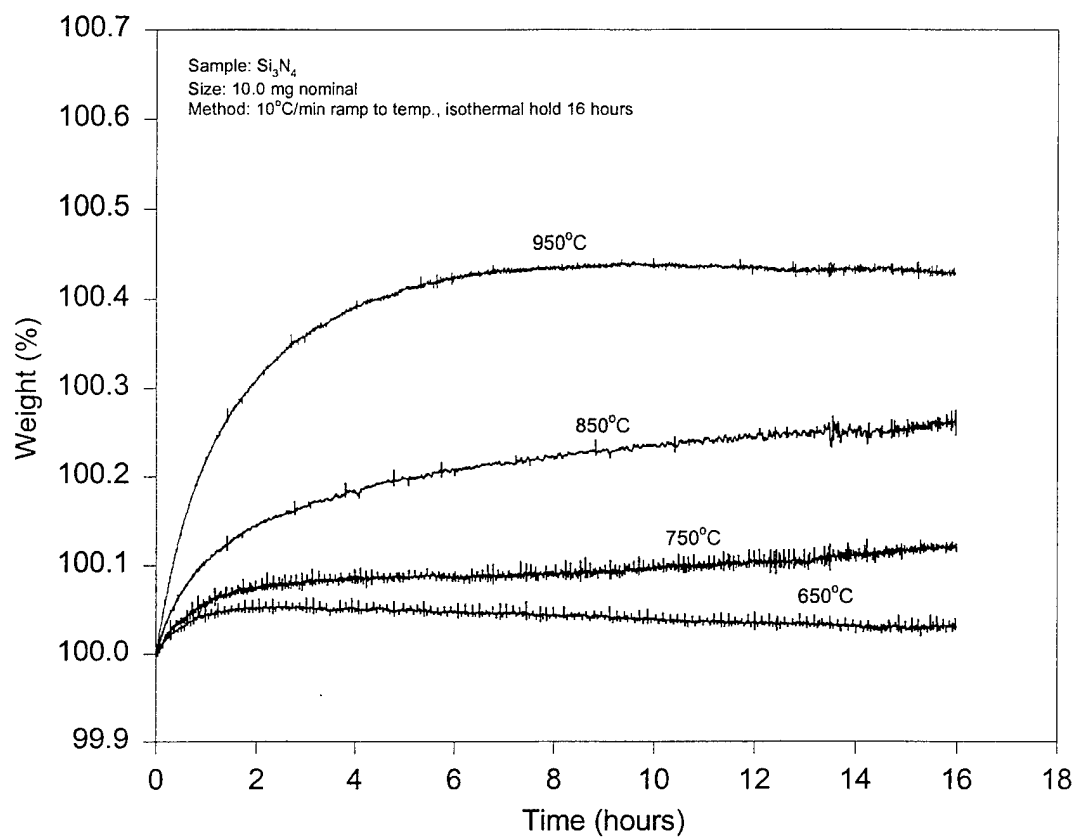
Figure B-10. Isothermal Oxidation Characteristics of Neat Si₃N₄ Powder in Air

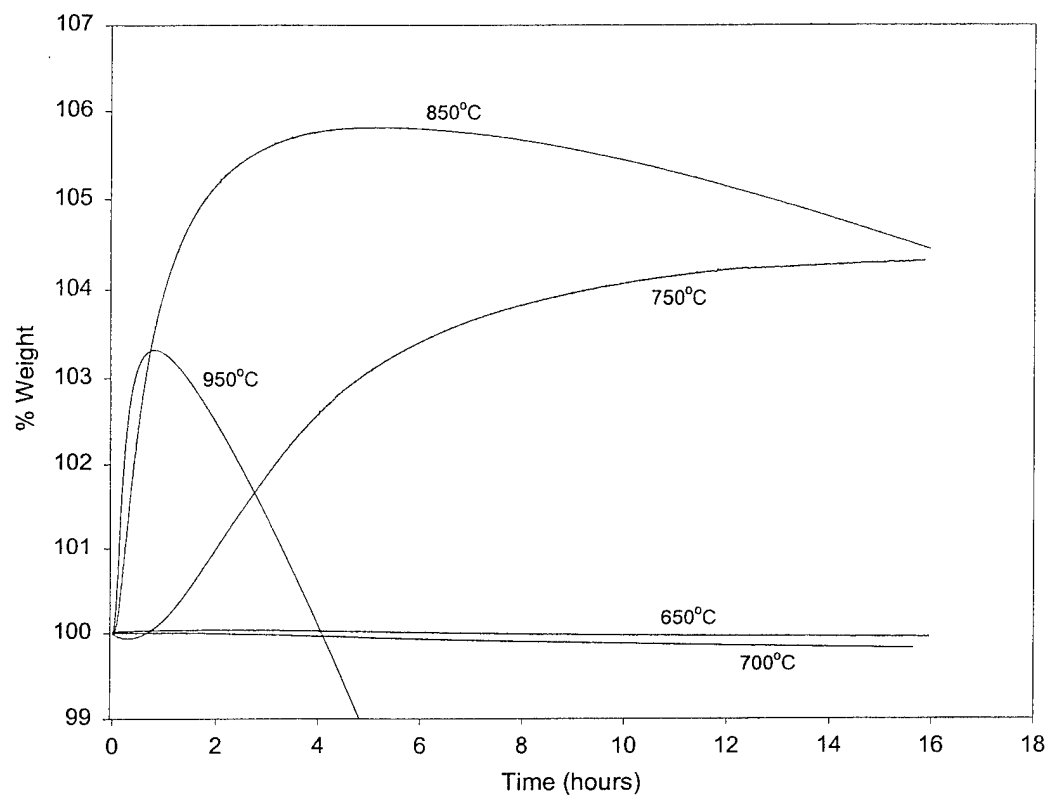Figure B-11. Isothermal Oxidation Characteristics of Si_3N_4 + Cs_2WOS_3 Mixtures in Air
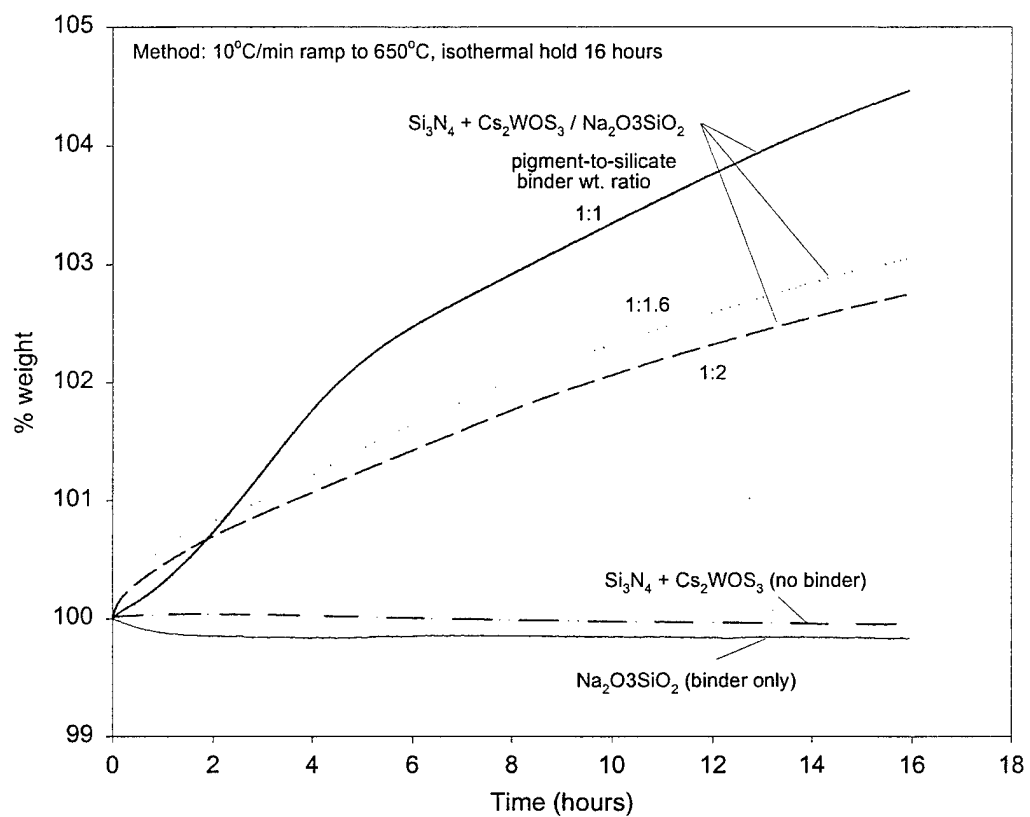
Figure B-12. Isothermal TGA of Si_3N_4 + $Cs_2WOS_3/Na_2O\,3SiO_2$ Mixtures at 650°C in Air

B2.2 High-Temperature DTA Results

DTA results obtained in air on neat-Cs_2WOS_3 and mixtures containing Si_3N_4 and sodium silicate are shown in Figure B-13. Cs_2WOS_3 exhibits three primary exothermic reactions in air between 300 and 600°C. These are in very good agreement with the oxidation reactions observed in TGA. Although TGA results show a weight loss in the 100 to 200°C range, no thermochemical activity was detected in the DTA record. The first sharp, well-defined exothermic peak observed has an extrapolated onset temperature of 315°C. Because of the possible overlap between the other two peaks, onset temperatures were not calculated for these. An endotherm, likely due to the melting of Cs_2WOS_3 decomposition products, is observed at an extrapolated onset of 782°C. Melting must have indeed occurred since the sample had overflowed and spilled onto the sides of the platinum cup. When Si_3N_4 is added to Cs_2WOS_3, the most obvious feature is the appearance of a broad exotherm that has an onset of 868°C and peaks slightly above 900°C. The exotherm closely matches the oxidation peak observed in TGA for the Cs_2WOS_3/Si_3N_4 mixtures. The 400°C exotherm also appears to be suppressed; however, this is could be an artifact caused by the difference in sample size and graphical scale between the two.

Similar to the TGA results, the presence of sodium silicate significantly alters the DTA characteristics of Cs_2WOS_3. The onset temperature of the first exothermic reaction is shifted to a slightly higher value, and the two weaker exotherms are noticeably absent. Also, the melting endotherm appeared to be absent as well. However, these could also be due to the lower Cs_2WOS_3 content of the sample. Nonetheless, it appears that the sodium silicate binder protects the Cs_2WOS_3 from oxidation and thermal decomposition, probably by encapsulating the Cs_2WOS_3 particles or by forming a more stable compound.

The mixture containing Si_3N_4, in addition to Cs_2WOS_3 and $Na_2O\,3SiO_2$, also appears to be more thermally stable. The first exotherm is shifted to a higher temperature (onset 350°C) while the broad high temperature exotherm is lowered (onset 740°C). The lowering of the broad exotherm to 740°C is in general agreement with the isothermal TGA data that showed that Si_3N_4/Cs_2WOS_3 mixtures containing sodium silicate appeared to oxidize at a lower temperature (650°C) than those that did not contain sodium silicate (see Figure B-12). These results indicate that there are high temperature chemical interactions between Cs_2WOS_3, sodium silicate, and Si_3N_4.

B2.3 TDMS Results

The gases evolved from Cs_2WOS_3 as a function of temperature were studied by TDMS. Results are shown in Figure B-14. Peaks at 64, 128, and 192 atomic mass units (AMU) are observed. Possible assignments for these include S_2, S_4, and S_6, respectively. Figure B-14 shows that sulfur is evolved in two stages, at about 75°C and between 350 and 600°C. The low-temperature evolution is believed to be due to elemental sulfur in the Cs_2WOS_3 powder. This corresponds well with the TGA and DTA results, which showed weight loss and no thermochemical activity at this

142
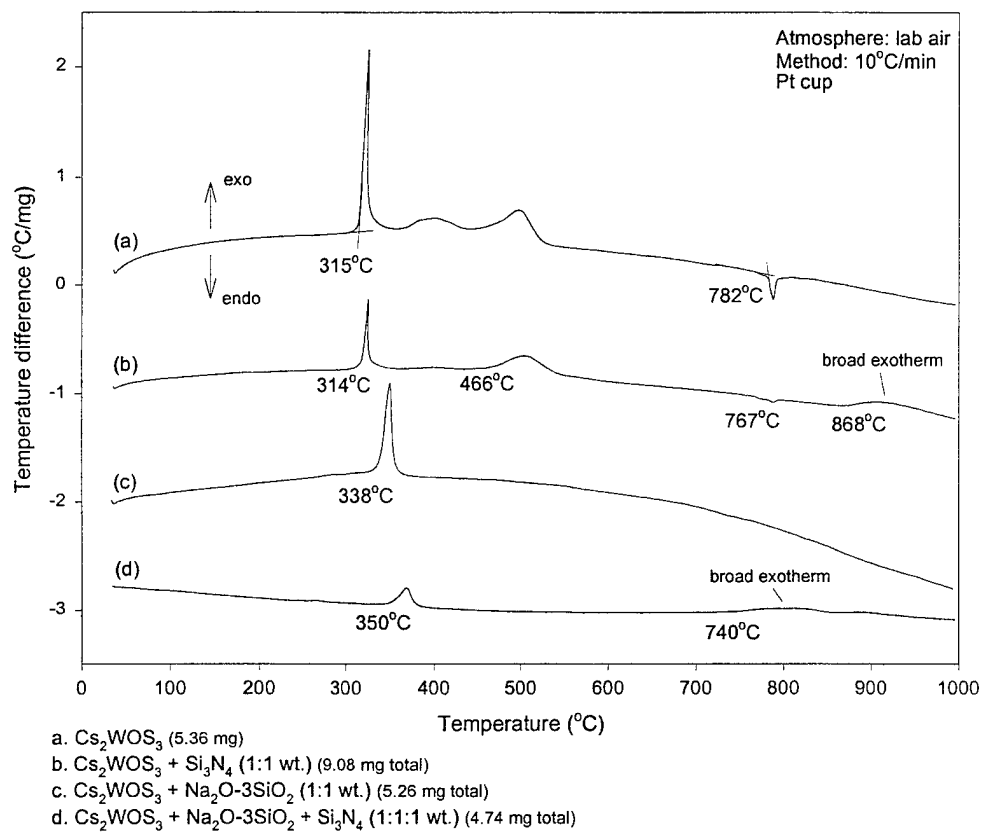
Figure B-13. DTA Thermograms Obtained in Air Showing Exothermic (Oxidation) and Endothermic (Melting) Onset Temperatures of Neat-Cs_2WOS_3 and Mixtures Containing Si_3N_4 and Sodium Silicate
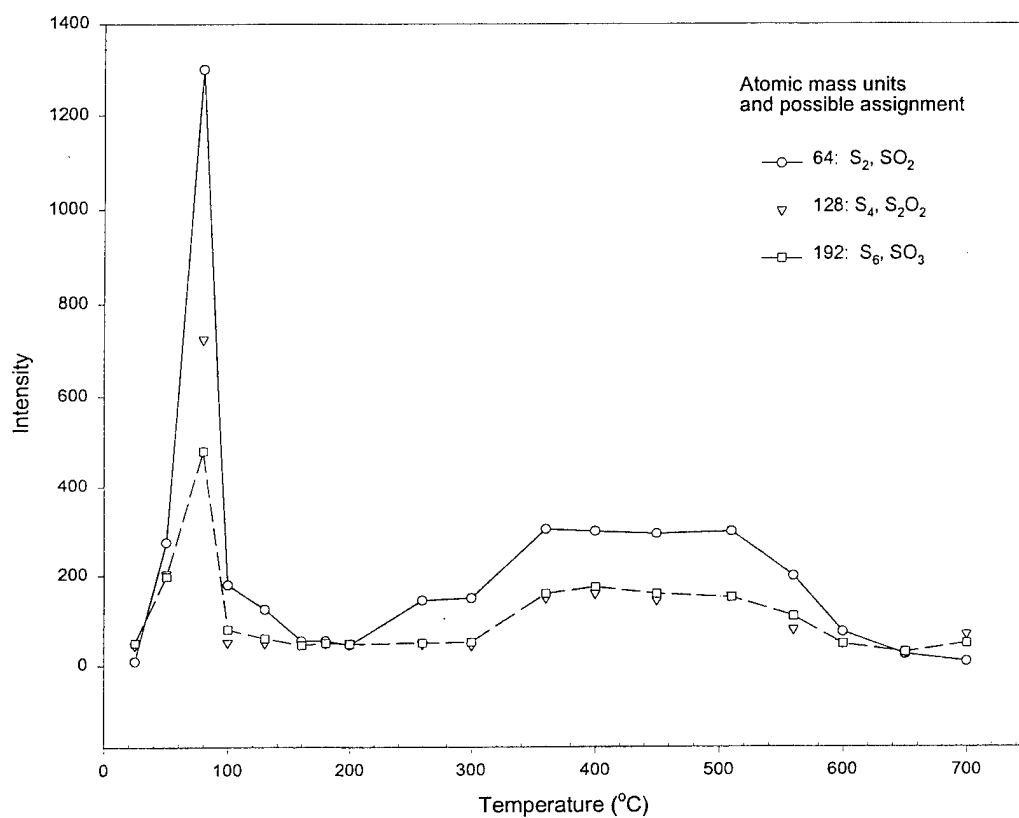
Figure B-14. Thermal Decomposition Mass Spectrum of Cs_2WOS_3 as a Function of Temperature Showing Gaseous Sulfur is Evolved from Cs_2WOS_3 in Two Stages

temperature. The high-temperature evolution matches very well with the temperature range where oxidation reactions are observed in TGA and DTA.

B3. Thermochemistry of Cs_2WOS_3

B3.1 XPS Surface Analysis

XPS surface analysis performed on four annealed Cs_2WOS_3 samples provided valuable information that complemented the thermal analysis, Raman, and FTIR results. Results are shown in Table B-2 and Figure B-15. The analysis focused on changes in neat-Cs_2WOS_3 with temperature since the results obtained on mixtures containing Si_3N_4 and sodium silicate were inconclusive. Electron binding energies (BE) of Cs_2WOS_3, in the as-received and annealed or pyrolyzed form, as well as for other tungsten- and sulfur-based compounds are given in Table B-3. The BE values shown for Cs_2WO_4 and Cs_2SO_4 were obtained from powder standards, while those shown for the other compounds were obtained from the literature. The BE values for the 700°C heated sample were not available.

The 500°C sample consisted of white and gray phases. An attempt was made to select agglomerates of particles of each phase and crush these to a fine powder. In doing so, it was noticed that these were not completely uniform in color. In some instances there was gray phase in the interior of the larger white agglomerates and vice versa. Results are shown for the gray phase only. Table B-2 and Figure B-15 show that there is an increase in oxygen content and a decrease in metal sulfide (S-M) concentration level as temperature increases. The surface oxygen atomic percent increased approximately linearly with increasing temperature. Also note that the surface tungsten level fluctuates with annealing temperature between 4 and 12 at.%, and the sharpest drop occurs immediately after the first oxidation reaction is observed in TGA / DTA (at 360°C). The sulfur-oxide (S-O) level, on the other hand, remains relatively constant up to 360°C. A slight drop in S-O species is detected at 500°C but levels again remain relatively constant up to 600°C. These results suggest that a sulfur oxide-rich layer is formed on the Cs_2WOS_3 particles during initial oxidation. By 700°C, however, sulfur is essentially depleted from the surface of the Cs_2WOS_3 particles and only oxygen, cesium, and tungsten are detected. The tungsten/cesium atomic ratio of 0.50 obtained on the 700°C treated sample is in good agreement with that of Cs_2WO_4. Though formation of Cs_2O and WO_3 are also possible.

Interpretation of chemical shifts in the XPS spectra based solely on changes in valency (i.e., electronegativity) becomes difficult due to the likelihood of metal complex formation during heating of Cs_2WOS_3. Considerable π-bonding exists in the $[WOS_3]^{2-}$ anion [145]. Formation of a coordination complex could result in what is known as back bonding or charge transfer between the central tungsten cation and ligand molecular orbitals [149]. In spite of this, some general observations could still be made if the atomic percentages previously discussed are also considered. Shifts in the

145

Table B-2. Approximate Atomic Percent Surface Composition of Pyrolyzed Cs_2WOS_3 as Determined by XPS*					
Sample	O	Cs	W	S	
				S-O	S-M
as-received	48.7	19.5	12.9	12.9	5.9
360°C	56.4	24.4	4.0	13.0	2.2
500°C (gray phase)	57.8	17.7	12.4	10.9	< 1.0
600°C	58.6	18.8	10.4	10.5	1.7
700°C	61.8	24.4	12.3	< 0.8	-

* Contribution of carbon is not included.
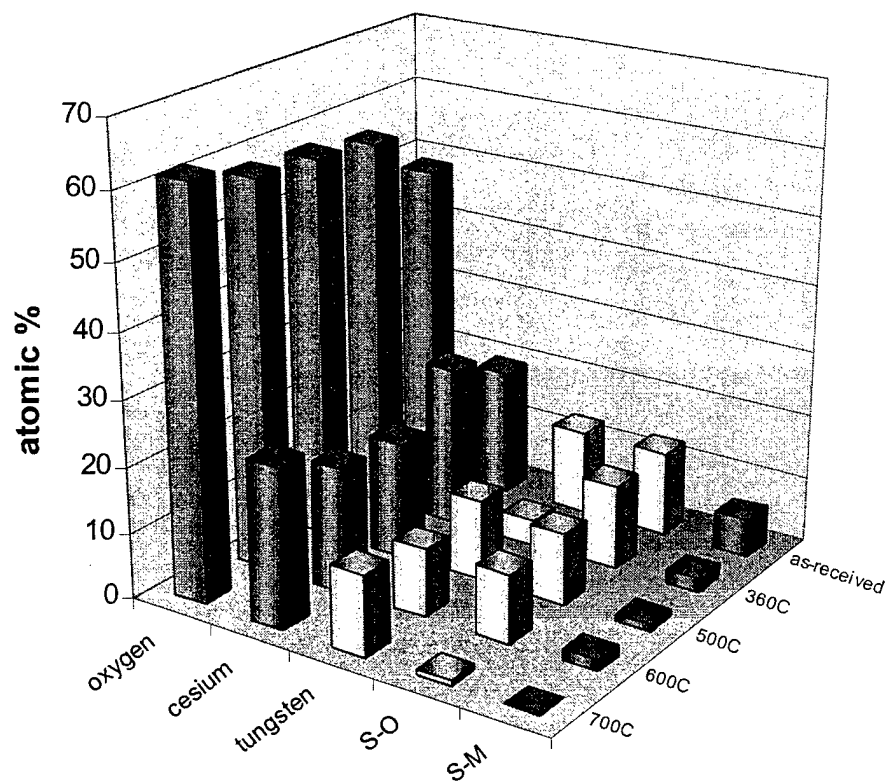
Figure B-15. Approximate Atomic Percent Composition of Pyrolyzed Cs_2WOS_3 as Determined by XPS

147

Compound [ref.]	O (1s)	Cs (3$d_{5/2}$)	W (4f)			S (2p)	
			4$f_{7/2}$	4$f_{5/2}$	ΔE*	S-O	M-S
Cs$_2$WOS$_3$ AR	530.5	724.9	35.8	38	2.2	169.5	162.5
360°C	531.0	724.2	34.9	37.0	2.1	168.1	163.0
500°C (gray phase)	530.8	724.3	35.2	37.2	2.0	170.4	-
600°C	530.8	724.5	35.4	37.4	2.0	168.8	162.7
Cs$_2$SO$_4$	530.9	724.0				167.6	
Cs$_2$WO$_4$	530.1	724.1	34.0	36.1	2.1		
W (metal) [146]			31.4	33.6	2.2		
WO$_3$ [147]	530.5		35.5	37.6	2.1		
WO$_2$ [147]	N.R.		32.5	34.6	2.1		
WS$_2$ [148]			31.9	34.1	2.2		161.8
Cs$_2$WS$_4$ [149]			35.9				

Table B-3. XPS BE of As-received and Pyrolyzed Cs$_2$WOS$_3$ and Other Tungsten and Sulfur Compounds (eV)

AR = as-received, N.R. = not reported
* ΔE = eV separation of W 4f doublet

sulfur $2p$ line were used to differentiate between sulfur-oxygen and sulfur-tungsten bonding while the tungsten $4f$ line was used as an indicator of chemical changes of Cs_2WOS_3 as a function of temperature, since chemical shifts in this particular line are more distinct than those observed in the other elements present (i.e., oxygen and cesium). Also, the W $4f$ band is normally composed of a doublet, caused by spin-orbit splitting of the $4f_{5/2}$ and $4f_{7/2}$ energy levels, typically observed in transition metals with unfilled or partially filled d orbitals [150]. The extent of splitting, in general, follows the degree of covalency, so that oxides should exhibit more splitting than sulfides for the same transition metal ion [150].

The W $4f$ spectra obtained on as-received Cs_2WOS_3 and the samples treated up to 600°C are shown in Figure B-16. BE values for all of the pertinent elements are tabulated in Table B-3. The doublet separation in the as-received material is about 2.2 eV, in good agreement with that observed for other tungsten-based compounds shown in Table B-3, including elemental tungsten. Also, the W $4f_{7/2}$ peak position at 35.8 eV is within the range reported for tungstates in general [146] and is close to the value reported for tungsten in its highest (common) oxidation state (W^{6+}) [147, 148]. Heating to 360°C (after the first oxidation reaction observed in TGA/DTA) causes a chemical shift in the W $4f$ doublet to lower binding energies indicating a change in tungsten bonding state has occurred. This is believed to be caused by the loss of sulfur, which would result in an increase in valence electrons and an increase in the electron screening effect. This is supported by the reduction in metal sulfide (S-M) concentration levels, shown in Table B-2 and Figure B-15, which indicates preferential loss of sulfur-tungsten bonded species. Charge transfer from tungsten cations to ligand molecular orbitals (i.e., back bonding), such as in the formation of a coordinated complex, could tentatively be ruled out since this would cause a shift to higher BE.

Further heating causes a reversal in the chemical shift of the W $4f$ lines to higher BE, indicating oxidation of tungsten or formation of a coordinated metal complex. The BEs for the $4f_{7/2}$ and $4f_{5/2}$ lines obtained on the 600°C sample are in excellent agreement with that reported for WO_3 [147, 151]. Though, the unambiguous identification of WO_3 could not be based on BE peak position and chemical shifts alone and requires other methods for accurate identification. Nonetheless, the W $4f_{7/2,5/2}$ doublet splitting appears more marked at 600°C, implying the presence of tungsten bonding of lower covalency than that present in the as-received material. This is in line with the breaking of sulfur-tungsten bonds (higher covalency) followed by tungsten oxidation (lower covalency).
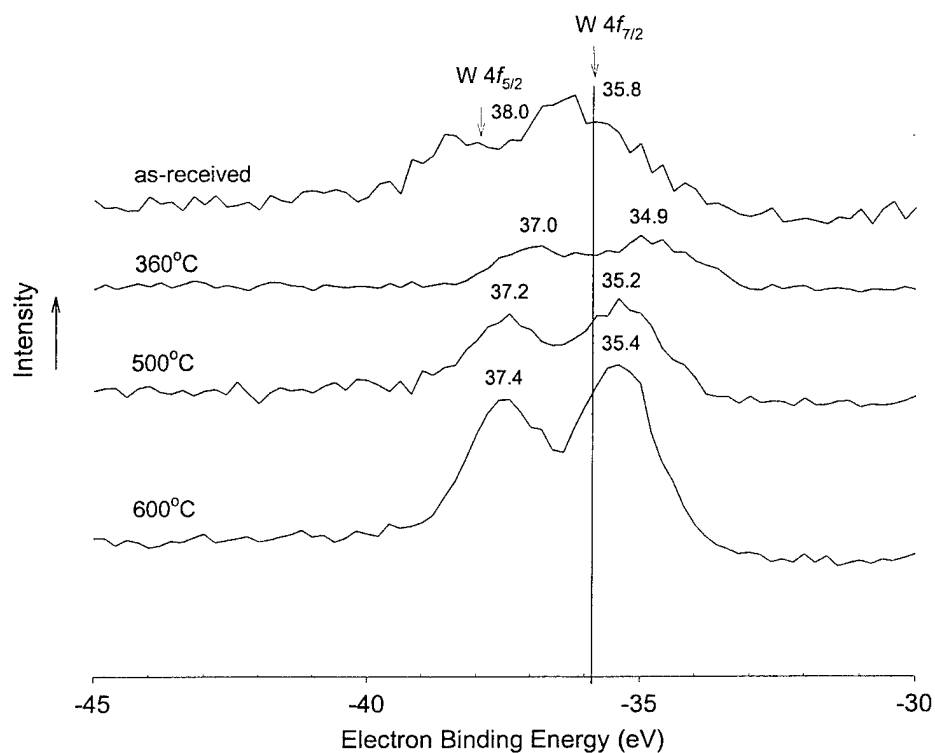
Figure B-16. High-resolution Tungsten 4*f* XPS Spectra Showing Chemical Shift in W 4$f_{7/2}$ and W 4$f_{5/2}$ Spectral Lines of Pyrolyzed Cs_2WOS_3

Note: Solid vertical line marks the position of the W 4$f_{7/2}$ line for the as-received material at 35.8 eV (i.e., W^{6+}).

B3.2 Raman and FTIR Spectroscopy of Pyrolyzed Cs_2WOS_3

Figures B-17 and B-18 show the Raman and IR spectra of pyrolyzed Cs_2WOS_3 samples, respectively. Special attention was given to the first oxidation reaction observed in TGA/DTA and the spectra show the sequence of changes in the $[WOS_3]^{2-}$ anion as this reaction proceeds from about 320°C to 360°C. Spectra are also shown for the sample treated at 600°C. The band assignments of the as-received material have been previously summarized in Table A-3 of the Appendix A.

At 200°C, the only change observed in Raman is the disappearance of the very weak bands at 147 and 214 cm^{-1}, which had been assigned to elemental sulfur. Also, the intensity of the very weak shoulder at 477 cm^{-1} appears to decrease somewhat. As the reaction proceeds from 320 to 360°C, there is a steady decrease (note the difference in graphical scale) in intensity of the WS_3 bending and W-S stretching bands observed in Raman at 172, 181, 245, 256, 453, and 467 cm^{-1} and an increase in the shoulder located at 477 cm^{-1}, next to the W-S symmetric stretching band. The intensity of the W-O stretching vibration at 861 cm^{-1} also decreases and appears to split with the appearance of a higher frequency component at about 879 cm^{-1}. New very weak bands at 308 and 961 cm^{-1} are also apparent by 340°C. Interestingly, these very weak bands correlate well with those reported for supported surface-tungsten oxide species, which are basically isolated WO_x units dispersed on a second oxide phase or substrate [148, 152, 153].

Re-appearance of the very weak bands at 147 and 214 cm^{-1} (free sulfur) between 332 and 360°C, implies that cleavage of some of the W-S bonds has occurred. This is consistent with the XPS spectra which showed shifts in the W $4f$ lines in this temperature range and reduction in S-M surface concentration levels. By 600°C, the $[WOS_3]^{2-}$ anion is destroyed, resulting in a complex Raman spectrum. Figure B-19 depicts the enlarged Raman and FTIR spectra obtained on this sample with possible major band assignments. The sharp intense vibration noted in Raman at 961 cm^{-1} on this sample is tentatively assigned to the S-O symmetric stretch (v_1) of $[SO_4]^{2-}$ in crystalline (orthorhombic) Cs_2SO_4 [154]. The presence of the medium and weak bands at 439, 614, and 1083-1110 cm^{-1} supports this. These bands agree closely with the SO_4 deformation (v_2 and v_4) and S-O asymmetric stretching (v_3) modes, respectively, of crystalline Cs_2SO_4 [154]. Of the four fundamental modes observed in Raman, only v_3 and v_4 should be IR active if the SO_4 units are in a highly symmetrical environment [155]. Coordination of SO_4 units, such as in the formation of a sulfato complex, will lower the symmetry and cause Raman-active modes to appear in IR and the doubly- and triply-degenerate v_2, v_3, and v_4 bands will split into nondegenerate ones [156]. Therefore IR, which will be discussed presently, provides additional information that will help confirm the presence of $[SO_4]^{2-}$ and ascertain whether a coordinated complex has formed.

The precise assignment of the other bands is not as straightforward. These are most likely due to tungsten oxide species though. The numerous bands observed below 300 cm^{-1} are probably due to lattice vibrational modes of these crystalline oxide phases.
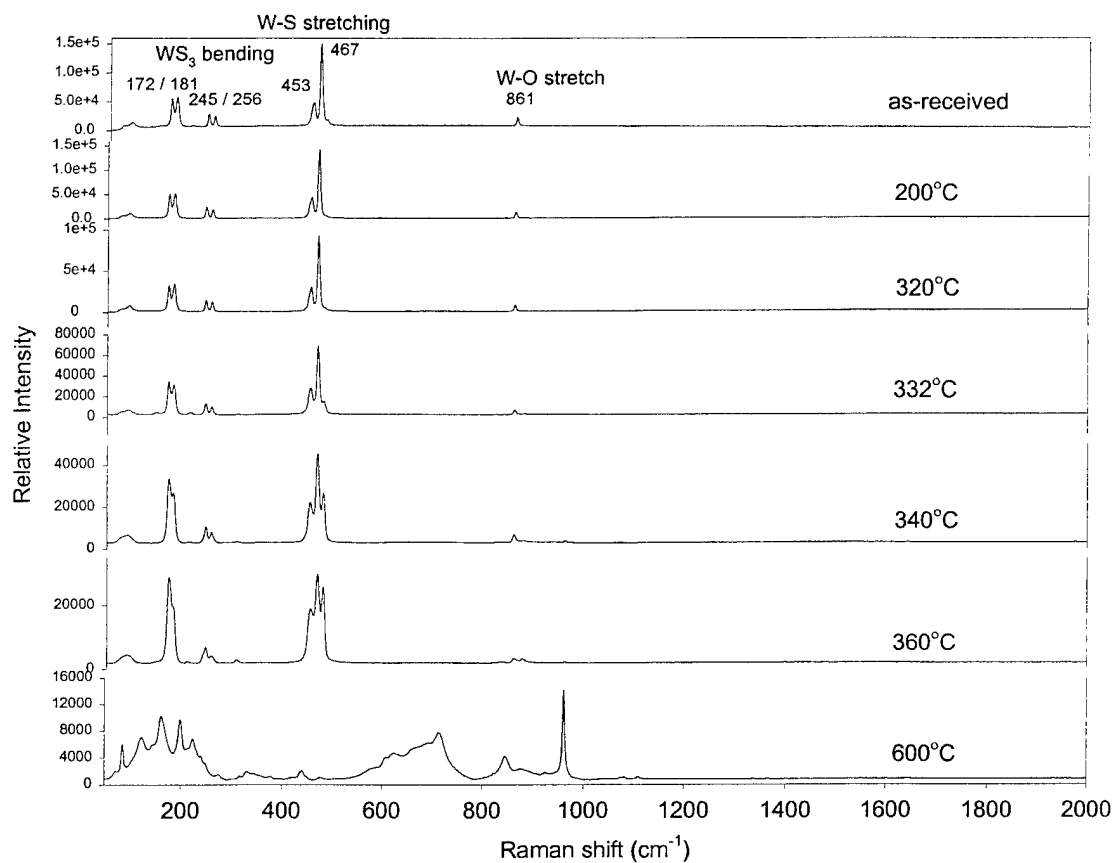
Figure B-17. Raman Spectra of As-received and Pyrolyzed Cs_2WOS_3

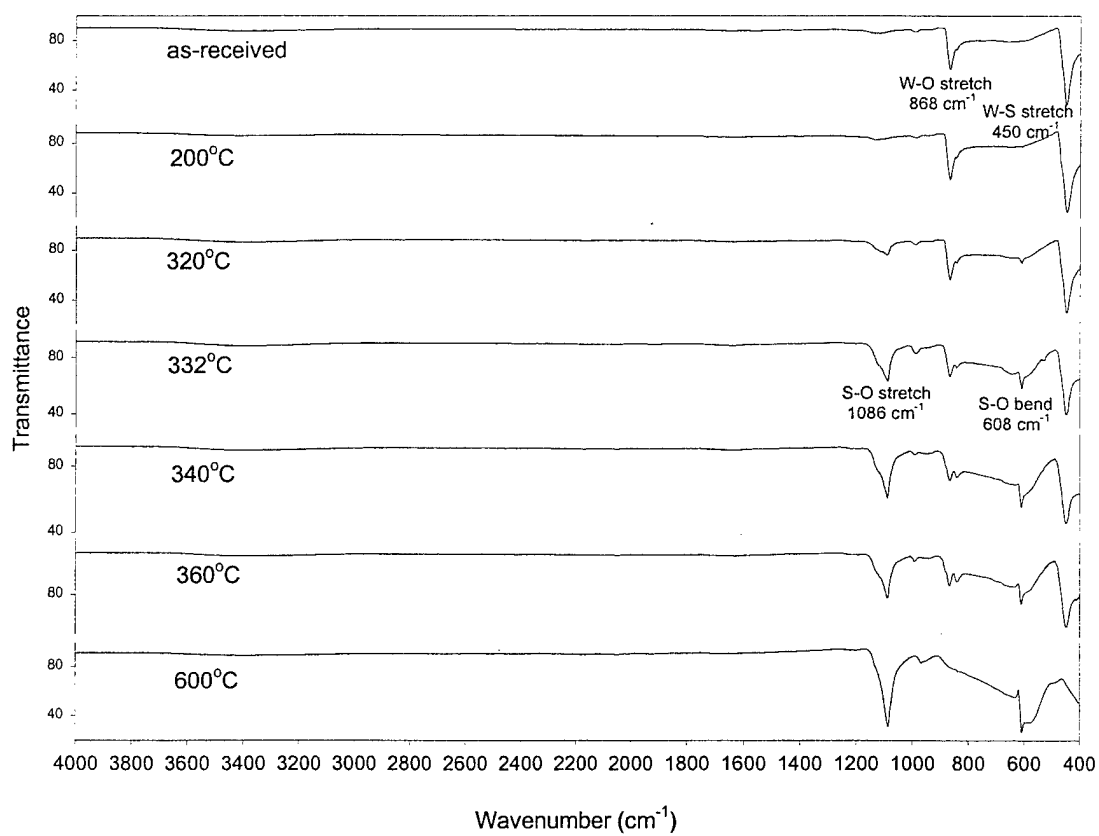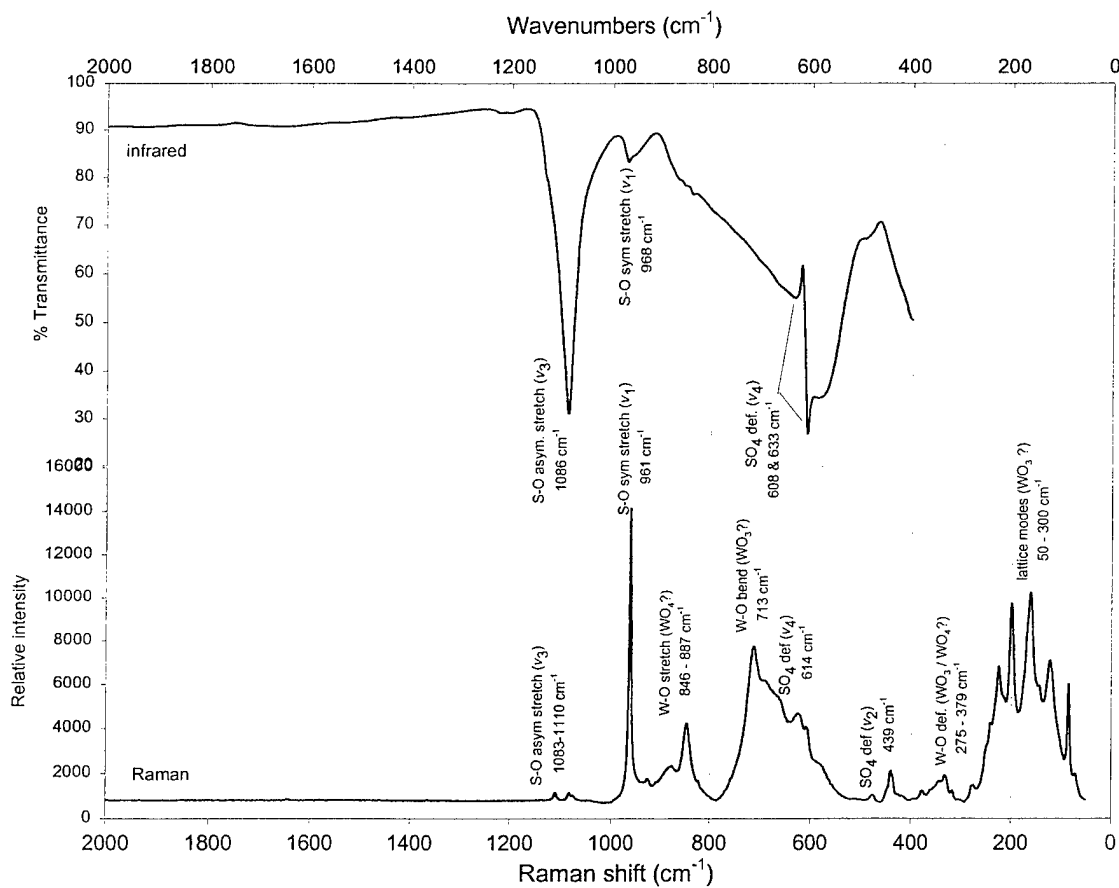Figure B-18. FTIR Spectra of As-received and Pyrolyzed Cs_2WOS_3

Figure B-19. Raman and FTIR Spectra of Cs_2WOS_3 Pyrolyzed at 600°C

For example, WO_3 exhibits numerous lattice modes in this region and has major bands at ~ 807 (W-O stretch, very strong), 715 (W-O bending mode, medium), and 272 cm^{-1} (W-O-W deformation mode, medium) [152, 153]. Conversely, highly symmetrical tetrahedral tungstates (i.e., Cs_2WO_4) exhibit four fundamental vibrational modes in Raman, which, similar to sulfates, can split into additional bands when distorted. The major bands reported for the free tetrahedral $[WO_4]^{2-}$ ion appear at ~ 931 (W-O stretch, symmetric), 838 (W-O stretch, antisymmetric), and 325 (two degenerate deformation modes) [157]. These will appear slightly shifted below or above these values in the solid state but well within the frequencies shown in Figure B-19. Features consistent with both of these tungsten oxide species appear in the spectrum of Figure B-19 and concur with the XPS results that showed that tungsten is present in a highly oxidized state.

In IR, there were no noticeable changes at 200°C. Interestingly, the intensity of the weak, broad bands noted at 1121, 993, and 658 cm^{-1}, which had been assigned to the S-O stretch and SO_4 bending modes in trace amounts of sulfate species found in the as-received material, steadily increase as the reaction proceeds. These shift to slightly lower frequencies, which eventually peak at 600°C at 1086, 968, and 608 cm^{-1}. The strong 1086 and 608 cm^{-1} IR absorptions are in good agreement with the out-of-phase S-O stretching (v_3) and bending modes (v_4), respectively, of inorganic sulfate $[SO_4]^{2-}$ ions, confirming the Raman results. The weak IR absorption at 968 cm^{-1} is believed to be associated with the in-phase S-O stretching (v_1) mode in SO_4 which has become IR active due to reduced symmetry [155]. This suggests that there is some distortion in the SO_4 tetrahedral species, which is expected in crystalline SO_4 salts. Though the apparent splitting of the v_4 mode into two separate components (at 608 and 633 cm^{-1}) could be an indication that some of the SO_4 units may be present as unidentate complex species [156]. At any rate, the results in general support the formation of crystalline Cs_2SO_4 at 600°C.

Although the formation of Cs_2SO_4 is evident as the reaction progresses, the IR bands at 868, 845 and 449 cm^{-1} of the W-O and W-S stretching modes of the $[WOS_3]^{2-}$ anion remain up to 360°C, indicating retention of some of the original Cs_2WOS_3 structure up to 360°C. Note, however, that there is a decrease in intensity of the W-O band at 868 cm^{-1} and an increase in the low frequency W-O component at 845 cm^{-1}. Similar to the Raman results, the IR spectrum shows that the $[WOS_3]^{2-}$ anion is destroyed by 600°C.

In view of these findings, the following sequence of events are proposed for the oxidation of Cs_2WOS_3. The initial oxidation reaction observed in TGA and DTA at about 315°C (~ 0.7 percent weight gain) appears to initiate with the breaking of W-S bonds. Charge balance is maintained by oxidation (oxygen uptake) with oxygen replacing sulfur in the $[WOS_3]^{2-}$ structure. This would explain the chemical shifts towards higher BE observed in the W $4f$ XPS spectra. The free sulfur is subsequently oxidized, part of which volatilizes as SO_2 as detected by TDMS while some remains trapped, probably as SO or SO_2 ligands bonded to tungsten via sulfur or oxygen bonding (i.e., W-S-O, W-O-S-O). The oxides of sulfur are known to commonly form

complexes by direct interaction as just described, particularly with transition metals [158]. With further heating, the bonded sulfur oxide further oxidizes, eventually forming SO_4. The FTIR spectra shows that the formation of SO_4 type species initiates immediately following the 315°C oxidation reaction and persists up to at least 600°C. The enhanced oxidation of trapped sulfur shows up as a gradual weight gain in TGA and as two exotherms in DTA between 400 and 600°C. The process could tentatively be represented with the following overall chemical formula:

$$Cs_2WOS_3 + 5O_2 \longrightarrow Cs_2SO_4\ (s) + WO_3\ (s) + 2SO_2\ (g)$$
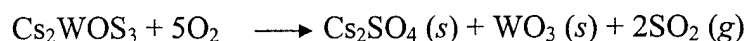
The Raman and FTIR results support the formation of crystalline (orthorhombic) Cs_2SO_4, yet did not unequivocally prove the formation of 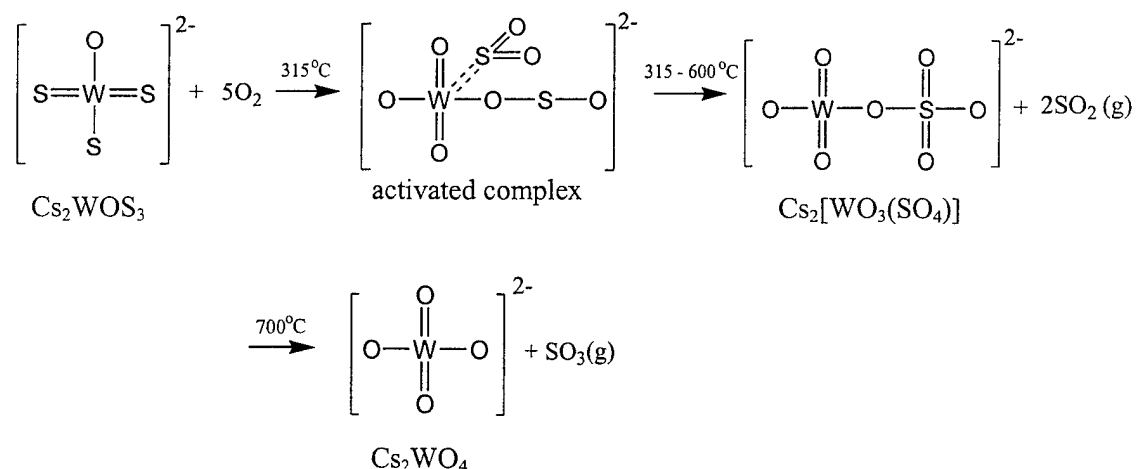WO_3 as a separate crystalline phase. Also, XPS analysis performed on a sample heated to 700°C shows that sulfur is nearly lost and a Cs/W atomic ratio in good agreement with that of Cs_2WO_4 was obtained. This implies that relatively weakly bonded SO_4 species were predominantly formed at 600°C since crystalline Cs_2SO_4 should remain thermally stable up to it's melting point of 1010°C [159]. Additionally, the FTIR spectra of the 600°C sample reveals distortion of SO_4 units and splitting of the v_4 degenerate mode into two components. This suggests the possibility of coordinated SO_4 species. An unidenate structure composed of SO_4 units coordinated to tungsten via oxygen bonding, similar to that shown below, would help explain these discrepancies:
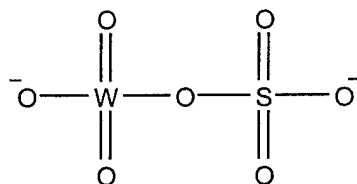
unidenate sulfato complex

The proposed structure would exhibit vibrational characteristics of Cs_2SO_4, Cs_2WO_4, and WO_3 in line with the experimental results. Furthermore, it would explain the loss of sulfur as gaseous SO_3 and formation of Cs_2WO_4 at 700°C, since sulfur-oxygen bonding is expected to be weaker than tungsten-oxygen bonding in this structure; S-O bond dissociation energy = 124.4 kcal/mol vs. 155 for W-O [160]. It is worth mentioning that the surface atomic percent of the elements present on the 600°C treated sample, as determined by XPS, correlate quite well with this structure (from Table B-2; W/S = 1.0, Cs/W = Cs/S = 1.8, and O/Cs = 3.1). Also, the uptake of three oxygen atoms for every sulfur atom that is lost in this scenario results in a net mass increase of about 3.0 weight percent, in fair agreement with the 1.5 percent measured experimentally by TGA, if the loss of some free sulfur in the compound is factored in.

Therefore, the following stepwise mechanism is proposed for the thermal decomposition of Cs_2WOS_3:

156

$$\left[\begin{array}{c} O \\ \| \\ S{=}W{=}S \\ | \\ S \end{array} \right]^{2-} + 5O_2 \xrightarrow{315^\circ C} \left[\begin{array}{c} O \quad O \\ \| \quad \diagup\!\! S{\diagdown}O \\ O{-}W{-}O{-}S{-}O \\ \| \\ O \end{array} \right]^{2-} \xrightarrow{315\text{-}600^\circ C} \left[\begin{array}{c} O \quad\quad O \\ \| \quad\quad \| \\ O{-}W{-}O{-}S{-}O \\ \| \quad\quad \| \\ O \quad\quad O \end{array} \right]^{2-} + 2SO_2\,(g)$$

$\qquad$ Cs$_2$WOS$_3$ $\qquad\qquad\qquad\qquad$ activated complex $\qquad\qquad\qquad\qquad$ Cs$_2$[WO$_3$(SO$_4$)]

$$\xrightarrow{700^\circ C} \left[\begin{array}{c} O \\ \| \\ O{-}W{-}O \\ \| \\ O \end{array} \right]^{2-} + SO_3(g)$$

$\qquad\qquad\qquad$ Cs$_2$WO$_4$

This mechanism helps explain the absence of sulfur observed in previous studies in wear tracks of posttested friction and wear samples and supports the hot corrosion mechanism of Si$_3$N$_4$ under dynamic sliding conditions (i.e., formation of highly reactive sulfo oxide species). It is also possible that the decomposition proceeds via a different path or mechanism in the presence of Si$_3$N$_4$ and/or the sodium silicate binder. The TGA and DTA results tend to support this. Likewise, the frictional energy under sliding conditions will also tend to accelerate the reaction rate (tribochemical effect), leading to decomposition at lower temperatures than those shown above.

B4. APPENDIX B REFERENCES

140. Clark, D.E., Pantano, C.G., and Hench, L.L., <u>Corrosion of Glass</u>, Books for Industry, New York (1979).

141. Casper, L.A. and Powell, C.J., <u>Industrial Applications of Surface Analysis</u>, ACS Sym. Series, New York, pp. 203 (1982).

142. J.C.P.D.S. (International Center for Diffraction Data) Powder diffraction file 09-0250.

143. Butt, D. P., Albert, D., and Taylor, T.N., "Kinetics of Thermal Oxidation of Silicon Nitride Powders," *J. Am. Ceram. Soc.*, **79** (11), pp. 2809-2814 (1996).

144. Wang, P. S., Hsu, S. M., Malghan, S. G., and Wittberg, T. N., "Surface Oxidation Kinetics of $Si_3N_4 - 4\%Y_2O_3$ Powders Studied by Bremsstrahlung-Excited Auger Spectroscopy," *J. Mater. Sci.*, **26**, pp. 3249-3252 (1991).

145. Diemann, E. and Müller, A., "XPS Investigation of the Valence Region of $MoOS_3^{2-}$ and WOS_3^{2-} in their Cs-Salts," *Chem. Phys. Letters*, **27**(3), pp. 351-354 (1974).

146. Wagner, C. D., Riggs, W. M., Davis, L. C., Moudler, J. F., and Muilenberg, G.E., <u>Handbook of X-ray Photoelectron Spectroscopy</u>, Perkin-Elmer Corp., p. 173 (1979).

147. Fleisch, T. H. and Mains, G. J., "An XPS Study of the UV Reduction and Photochromism of MoO_3 and WO_3," *J. Chem. Phys.*, **76** (2), pp. 780-786 (1982).

148. Salvati, L., Makovosky, L. E., Stenci, J. M., Brown, F. R., and Hercules, D. M., "Surface Spectroscopic Study of Tungsten-Alumina Catalysts Using X-ray Photoelectron, Ion Scattering, and Raman Spectroscopies," *J. Phys. Chem.*, **85**, pp. 3700-3707 (1981).

149. Carlson, T. A., <u>Photoelectron and Auger Spectroscopy</u>, Plenum Press, New York, pp. 217-220 (1978).

150. Carlson, T. A., <u>Photoelectron and Auger Spectroscopy</u>, Plenum Press, New York, pp. 231-241 (1978).

151. Sarma, D. D. and Rao, C. N. R., "XPES Studies of Oxides of Second- and Third Row Transition Metals Including Rare Earths," *J. Electron Spectrosc. Relat. Phenom.*, **20**, pp. 25-45 (1980).

152. Wachs, I. E., Hardcastle, F. D., and Chan, S. S., "Raman Spectroscopy of Supported Metal Oxide Catalysts," Reprint from *Spectroscopy*, **1**(8), p. 30 (1986).

153. Horsley, J. A., Wachs, I. E., Brown, J. M., Via, G. H., and Hardcastle, F. D., "Structure of Surface Tungsten Oxide Species in the WO_3/Al_2O_3 Supported Oxide System from X-ray Absorption Near-Edge Spectroscopy and Raman Spectroscopy," *J. Phys. Chem.*, **91**, pp. 4014-4020 (1987).

154. Montero, S., Schmölz, R., and Haussühl, S., "Raman Spectra of Orthorhombic Sulfate Single Crystals, I: K_2SO_4, Rb_2SO_4, Cs_2SO_4, and Tl_2SO_4," *J. Raman Spectrosc.*, **2**, pp. 101-113 (1974).

155. Colthup, N. B., Daly, L. H., and Wiberley, S. E., Introduction to Infrared and Raman Spectroscopy, Academic Press, Boston, p. 376 (1990).

156. Nakamoto, K., Infrared and Raman Spectra of Inorganic and Coordination Compounds, 4th Ed., John Wiley and Sons, New York, pp. 248-251 (1986).

157. Nakamoto, K., Infrared and Raman Spectra of Inorganic and Coordination Compounds, 4th Ed., John Wiley and Sons, New York, p. 138 (1986).

158. Cotton, F. A. and Wilkinson, G., Advanced Inorganic Chemistry, 4th Ed., John Wiley & Sons, New York, pp. 181-182 and 526-533 (1980).

159. Handbook of Chemistry and Physics, 53rd Ed., Weast, R. D., Editor, CRC Press, Inc., Boca Raton, p. B-82 (1972-1973).

160. Handbook of Chemistry and Physics, 53rd Ed., Weast, R. D., Editor, CRC Press, Inc., Boca Raton, pp. F-183-184 (1972-1973).

LIST OF ACRONYMS

ACRONYM	DESCRIPTION
μ-FTIR	micro-Fourier transform infrared
AES	Auger electron spectroscopy
AFRL	Air Force Research Laboratory
AMU	Atomic mass units
AR	As-received
ATR	Attenuated total reflection
BE	Binding energies
BET	Brunauer-Emmett-Teller
C-C	Carbon-carbon
DTA	Differential thermal analysis
DTGS	Deuterium triglycine sulfate
EDS	Energy dispersive x-ray spectrometry
HIP'ed	Hot-isostatically pressed
IHPTET	Integrated High Performance Engine Technology
HT-DTA	High-temperature differential thermal analysis
IR	Infrared
IRE	Internal reflection element
MDN	shaft diameter (mm) multiplied by rpm divided by 10^6
NB	Non-bridging
NMR	Nuclear magnetic resonance
SEM	Scanning electron microscopy

ACRONYM	DESCRIPTION
s.s.	Steady-state
TDMS	Thermal decomposition mass spectrometry
TEM	Transmission electron microscopy
TGA	Thermal gravimetric analysis
UHV	Ultra-high vacuum
VPD	Vapor phase deposition
XPS	X-ray photoelectron spectroscopy
XRPD	X-ray powder diffraction